RADAR System for Sense and Mapping in Small Manned Air Vehicles

Nuno Filipe Paquim Soares Brandão

Thesis to obtain the Master of Science Degree in

Aerospace Engineer

Supervisors: Prof. Custódio José de Oliveira Peixeiro
Prof. Ricardo Adriano Ribeiro

Examination Committee:

Chairperson: Prof. Paulo Jorge Coelho Ramalho Oliveira
Supervisor: Prof. Ricardo Adriano Ribeiro
Member of the Committee: Prof. António Luis Campos da Silva Topa

December 2022

Declaration:

I declare that this document is an original work of my own authorship, and that it fulfills all the requirements of the Code of Conduct and Good Practices of the Universidade de Lisboa.

Front cover image extracted from:

https://www.atlas-mag.net/en/article/the-chinese-flying-taxi-ehang-184-is-ahead-of-those-of-airbus-and-uber

My beloved father,
you left too soon.

Acknowledgements

First, I will start by thanking my beloved mother, who was the main source of support, motivation, balance, and inspiration in my life from an early age, and to my step father, that also pushed me through during this rough years.

I would also like to thank to my close friends who are in my everyday life, for allowing me to have an escape when times are rough.

Finally, I would like to give a special thank you to both my supervisors, for all the time and effort spent explaining, discussing with and helping me in all the difficulties found during the development of this work, and to the "Instituto de Telecomunicações (IT)" of Instituto Superior Técnico.

Resumo

Veículos aéreos de baixa altitude, têm sido, recentemente, alvo de intenso desenvolvimento para aplicações como o transporte de carga, ou mesmo de pessoas. É de extrema importância manter o veículo a salvo de colisões, principalmente quando se considera o transporte de seres humanos.

Neste trabalho, é feita uma simulação de um sistema de radar para identificação de alvos ao seu redor, com enfase no projecto da antena utilizada. É feito o projeto de uma antena impressa quadrada (dimensionada em termos da frequência de ressonância), de um agregado de antenas planares com capacidade de direcionamento do lobo principal (versátil em termos de largura do feixe do lobo principal), e de um método de simulação de radar (versátil em termos de sensibilidade de identificação de alvos).

Os modelos da linha de transmissão e da cavidade resonante foram utilizados para calcular as dimensões iniciais de uma antena impressa quadrada. A antena utilizada ao longo deste trabalho foi projetada a 35 GHz, sendo alimentada para radiar ondas com polarização linear dupla (vertical e horizontal), de forma a minimizar a probabilidade de perda de alvos devido à desadaptação de polarizações.

O elemento impresso quadrado otimizado é usado num agregado planar de Dolph-Chebyshev, também quadrado, de 8x8 elementos. Este tipo de agregado garante o menor nível de lobos secundários, para a largura de feixe definida, de acordo com as exigências das aplicações em radar. O lobo principal pode ser apontado até um desvio máximo de 45°, em relação à direção perpendicular ao plano do agregado.

Os conceitos foram validados por meio de simulação, sendo esta baseada em imagens obtidas de um ambiente virtual 3D, com o objetivo de identificar a posição dos alvos em relação ao sistema. São testados cenários de curto e de longo alcance.

Palavras-chave: AAV, UAV, antenas impressas, antena impressa com dupla polarização linear, agregados de Dolph-Chebyshev, agregados planares, direcionamento do lobo principal, radar de ondas milimétricas, simulação de sinal de radar

Abstract

Low altitude air flying vehicles, have emerged recently for cargo or even human transportation. It is of utmost importance to maintain the vehicle safe from collisions, specially when transportation of humans is considered.

In this work, a simulation of a radar system to identify targets in its surroundings is done, with emphasis in the design of the sensing component of the system (the antenna). The design of a square microstrip patch antenna (being versatile in terms of resonant frequency), of a planar antenna array with main lobe steering capability (being versatile in terms of main lobe beam width), and of a target detection method for the radar (being versatile in terms of target identification sensibility) are done.

The transmission line and cavity models are used to compute the dimensions of the square microstrip patch antenna. The antenna used throughout this work was designed at 35 GHz, being fed to radiate dual linear polarized waves, to minimise the probability of missing targets due to polarization mismatch.

The optimized square microstrip patch element is used on a Dolph-Chebyshev planar array, also square, with 8x8 elements. This type of array provides the lowest side lobe level, for the defined beam width, as required in radar applications. The main lobe can be scanned up to 45° from broadside.

The concepts are validated using a simulation method, based on images taken from a 3D environment, with the purpose of identifying the targets positions relative to the system. A long range and a short range scenarios are tested.

Keywords: AAV, UAV, microstrip patch antennas, dual linearly polarized patch antenna, Dolph-Chebyshev arrays, planar arrays, beam steering, mm-wave radar, radar signal simulation

Index

List of Tables

List of Figures

List of Abbreviations

ADAS	Advanced Driver Assistance System
ADC	Analogue to Digital Converter
AAV	Autonomous Air Vehicle
DAC	Digital to Analogue Converter
DFT	Discrete Fourier Transform
FFT	Fast Fourier Transform
ELOS	Equivalent Level of Safety
EHF	Extremely High Frequency
FMCW	Frequency Modulated Continuous Wave
FPGA	Field Programmable Gate Array
GNSS	Global Navigation Satellite System
IMU	Inertial Measurement Unit
LNA	Low Noise Amplifier
MIMO	Multiple Input Multiple Output
MPR	Mechanically Pivoting Radar
OTMS	On-board Terrain Mapping Systems
PRF	Pulse Repetition Frequency
RF	Radio Frequency
SiGe	Silicon Germanium
SLAM	Simultaneous Location and Mapping
SOI-CMOS	Silicon on insulator Complementary metal–oxide–semiconductor
UAV	Unmanned Aerial Vehicle
UHF	Ultra High Frequency
UWB	Ultra Wide Band

List of Symbols

Constants

c	Speed of light in vacuum - 3×10^8 [m/s]
ϵ_0	Vacuum Permittivity - 8.854 $\times 10^{-12} [F/m]$
k_{boltz}	Boltzmann constant - 1.380649×10^{23} [J/K]
μ_0	Vacuum Permeability [m] - 4$\pi \times 10^{-7} [H/m]$

Greek Symbols

α_{cam}	Camera orientation [°]
ΔL	Extension along the length of a patch antenna [m]
ϵ_r	Substrate relative dielectric constant
ϵ_{reff}	Substrate relative effective dielectric constant
Γ	Reflection Coefficient
Γ_L	Absolute load reflection coefficient
λ_0	Wavelength propagating in free-space [m]
λ_g	Wavelength propagating in the embedded substrate [m]
ϕ	Angle of latitude [°]
ϕ_0	Theoretical steering angle [°]
ψ	Wavenumber space auxiliary variable [rad]
ψ_0	Steering phase of the array factor [rad]
ψ_{ij}	Phase shift of element (i,j) of the array [rad]
σ	Radar cross section [m^2]
σ_N	Signal noise standard deviation
$\sigma_{px,py}$	Radar cross section of the surface represented in pixel (px,py) [m^2]
θ	Angle of longitude [°]
θ_{fep}	Angle of point in a polar plot of a fisheye equidistant projection image
θ_{inc}	Angle of incidence [°]
θ_{res}	Angle per pixel resolution [°]

Roman Symbols

$A(\cdot)$	Array factor
A_e	Effective area of the antenna [m^2]
A_{fft}	Amplitude of the signal computed from the FFT

A_{mnp}	Amplitude coeficient of mode mnp
$A_{tt_{ij}}$	Attenuation in power of the antenna (i,j) of the radar system
A_x	Potential vector
a_n	Weight coefficient of antenna n of the array
a_{ij}	Weight coefficient of antenna i,j of the array
B	Radiating slot susceptance [S]
B_{ch}	Chirp bandwidth [Hz]
D_0	Asymptotic directivity values
d	Distance between consecutive antennas in the array
f_b	Beat frequency of the radar signal [hz]
$f_{b;px,py}$	Beat frequency contribution of the simulated signal obtained from pixel (px,py) [hz]
f_{min}	Chirp minimum frequency [hz]
f_N	Nyquist frequency [hz]
f_r	Resonant frequency [hz]
f_s	Sampling frequency [hz]
$(f_r)_{mnp}$	Resonant frequency of mode mnp [hz]
$F(k)$	Radiation vector at a wavenumber k [W]
G_{LNA}	Gain of the LNA of the radar system
G_r	Radiating slot conductance [S]
G_{total}	Total gain of the array
$G(\theta,\ \phi)$	Gain of the array in the direction $(\theta,\ \phi)$
$G_{px,py}$	Gain of the array in the direction of pixel (px,py)
h	Substrate height of the antenna/array [mm]
j	Imaginary Number
$J(r)$	Current density at a distance r [A/m^2]
k_0	Wavenumber for the EM field in free-space [rad/m]
k_g	Wavenumber for the EM field within the embedded substrate [rad/m]
k_x	Wavenumber for the EM field in x-axis [rad/m]
k_y	Wavenumber for the EM field in y-axis [rad/m]
k_z	Wavenumber for the EM field in z-axis [rad/m]
L	Microstrip patch length [mm]
L_{eff}	Effective microstrip patch length [mm]
L_{qwt}	Length of the quarter wavelength transformer [mm]
L_1	Inset feed length [mm]
l	Distance from the load [mm]
$l_{px,py}$	Sidelength of a squared plate in pixel (px,py) [m]
N_0	Noise power spectral density [W]
N_{pix}	Linear number of pixels of an image
P_{cam}	Camera position [m]
P_d	Probability of correct target detection
P_D	Power density of the antenna [W/m^2]
P_{fa}	Probability of incorrect target detection (false alarm)
P_{in}	Incident power [W]
P_{ref}	Reflected power [W]

P_r	Total received power by the radar system [W]
P_{rt}	Power reflected by a target [W]
$P_{r,min}$	Minimum received power to detect a target [W]
$P_{r;px,py}$	Received power by the object represented in pixel (px,py) [W]
P_t	Total transmitted power by the radar system [W]
P_{t0}	Transmitted power per antenna of the radar system [W]
P_{tr}	Transmitted power [W]
P_{Rij}	Received power by the antenna (i,j) of the radar system [W]
P_{Tij}	Transmitted power by the antenna (i,j) of the radar system [W]
r_{fep}	Radius of point in a polar plot of a fisheye equidistant projection image
$\overrightarrow{r_{pos}^{ant}}$	Unitary vector pointing to a position, in the antenna system referential
$\overrightarrow{r_{pos}^{cam}}$	Unitary vector pointing to a position, in the $Blender$ camera referential
$\overrightarrow{r_{pos}^{scene}}$	Unitary vector pointing to a position, in the $Blender$ scene referential
R	Target distance [m]
R_{abs}	Absolute relative side lobe attenuation
R_a	Relative side lobe attenuation [dB]
R_{ij}	Target distance at index (i,j) [m]
R_L	Load resistance [Ω]
R_{max}	Maximum detectable distance by the radar system [m]
$R_{px,py}$	Distance of the object represented in pixel (px,py) [m]
R_{sim}	Distance computed from the simulation of one radiation pattern [m]
R_XYZ	Euler rotation matrix over the axis with order X-Y-Z
R_X	Euler rotation matrix over the X axis
R_Y	Euler rotation matrix over the Y axis
R_Z	Euler rotation matrix over the Z axis
R_0	Resistance of the edge of the patch at resonance [Ω]
R_{in}	Input resistance of the patch at resonance [Ω]
$S_{ADC}(\cdot)$	Signal to be sampled by the ADC of the radar system [V]
$S_b(\cdot)$	Beat signal of the radar system [V]
S_{mn}	Scattering Matrix element with mn index
S_{sim}	Simulated radar signal [V]
$S_{t0}(\cdot)$	Linear modulated chirp signal [V]
$S_{IFij}(\cdot)$	Intermediate frequency signal of the antenna (i,j) of the radar system [V]
$S_{Rij}(\cdot)$	Received signal by the antenna (i,j) of the radar system [V]
$S_{Tij}(\cdot)$	Signal to transmit through the antenna (i,j) of the radar system [V]
TM_{mnp}	Transverse electromagnetic mode with index mnp
T_{ch}	Chirp duration [s]
$T_n(\cdot)$	Dolph-Chebyshev polynomial of first kind
T_{noise}	Receiver noise temperature [K]
T_s	Sampling interval [s]
V_G	Generator voltage [V]
V_{th}	Threshold voltage to claim the detection of a target [V]
W	Microstrip patch width [mm]
W_0	Transmission line width [mm]
X_L	Load reactance [Ω]

x_i	Location of the zeros of the Dolph-chebyshev array factor in the wavenumber space
W_{qwt}	Width of the quarter wavelength transformer [mm]
$W(\cdot)$	Window function
$w(\cdot)$	Spectral noise [V]
Y_C	Transmission line admittance [S]
Y_{in}	Input admittance [S]
Z_C	Transmission line impedance [Ω]
Z_G	Generator impedance [Ω]
Z_{in}	Input impedance [Ω]
Z_L	Load impedance [Ω]
Z_n	Impedance of the n-th transmission line [Ω]
Z_{pass}	Distance data of an image, exported from $Blender$ [m]
Z_{qwt}	Impedance of the quarter wavelength transformer [Ω]
Z_0	Characteristic impedance of a transmission line [Ω]
z_{in}	Normalized input impedance

Chapter 1

Introduction

In this chapter, an overview of the developed theme is presented, along with the motivation to study this topic, the objectives, main results, and a brief summary of the thesis structure.

1.1 Overview

The term Radar stands for "Radio Detection and Ranging". A Radar system works by transmitting electromagnetic waves that propagate in free-space and reflect in objects along their path. An antenna is one of the main components of a Radar system, being used to convert the energy from a guided wave to the free-space wave, and vice-versa. When transmitting, the antenna transfers the electromagnetic signal at carrier frequency to the free-space, and when receiving it collects the reflected signal from the target. A Radar system can have a wide area of applications depending on its type, that is defined based on the antenna characteristics. In this work, a narrow beam low side lobe level Radar system is designed, with the purpose of mapping the objects located in an environment.

In a Radar system, by receiving the echo signal, besides claiming or not the detection of a target, it is also possible to calculate its distance, by analysing the time delay between the transmitted and received signal, and relative radial velocity, by analysing the frequency shift of the reflected wave caused by the Doppler effect [1]. A Radar cannot resolve as much detail as other type of sensors available nowadays, and it is costlier to manufacture, but has the advantage of being capable of providing reliable information under adverse environmental conditions, in which the others cannot [1], thus being essential for a more reliable safety system of air vehicles.

In this work, the Radar data will be simulated using *Blender* software to define a 3D environment, with a post-processing phase in *Python* using the camera rendered image to simulate the radar signal of a system, using the previously designed array. The data obtained from the Radar can be stored and mapped to a 3D construction model, according to the system position and orientation related to a local coordinate system. Simultaneous Location and Mapping (SLAM) algorithms allow to monitor the position and orientation of the system, and to receive data from sensing components to be processed, placed and updated within the system local referential [2].

1.2 Motivation

The use of quad-rotors and other types of Unmanned Air Vehicles (UAVs) is growing over time not only for military applications but also for high risk activities, cargo transportation, among many other civil applications

[3]. Radar imaging is an efficient and viable solution that allows the coverage of a wide and/or not easily accessible region, and provides a high operative flexibility [4].

Due to the inherent nature of the low altitude flying vehicle, obstacle awareness is a fundamental requirement to avoid the collision against stationary and/or moving obstacles along the flight path, either for manned or unmanned air vehicles [5]. With the knowledge about what surrounds the vehicle it is possible to keep the flight safe from collisions, what is of utmost importance for these type of vehicles in order to be accepted and used by human operators. Regulatory requirements reflect that to operate in civilian airspace an Autonomous Air Vehicle (AAV) must have Sense and Avoid capabilities that meet or exceed the level of performance of a human pilot, without cooperative communication with other aircrafts or prior knowledge of their flight plans [6].

There are several sensors commonly used to sense the environment, namely Lidar, Sonar, Radar, visual cameras and infrared sensors [5]. However, Radar is mostly used only to determine the velocity of a detected target, since it has a high manufacture cost comparing to the other sensors [6]. Since Radar systems are reliable under bad weather conditions, they could be used as the short to long range sensor that firstly identifies the presence of a target [7]. Then, by complementing it in a computational algorithm with data from the other sensors, it is possible to get detailed information about each detected object, and to build a detailed map of the surroundings. However, if the Radar system's angular resolution is fine enough to identify targets with some detail, it could be sufficient to provide a safe flight even in moments where all the other sensors were unable to provide reliable data [7].

Microstrip Patch Antennas are widely used in the Airspace Industry. These are low profile, light weight, with a low production cost and simple design methods, that are very versatile regarding their resonant frequency, polarization, impedance and radiation pattern. Patches can have different shapes, each with a specific design method associated [8]. There are also four easily adaptable common feeding methods for a patch antenna, making these antennas versatile in terms of physical design. Each patch antenna propagates the energy to the free-space through its borders according to its radiation pattern, that is possible to modify either by the design of the single antenna element, or by the design of an array using a large number of elements. Furthermore, the physical size of each patch antenna is inversely proportional to its resonant frequency, thus, by increasing the frequency to the mm wave range (30-300 GHz) it is possible to design an array with size suitable for air vehicles applications [9].

The desired radiation pattern requires a narrow main-beam and a low side lobe level. A single antenna won't be able to provide such characteristics, despite its operating frequency, and thus the need of designing an array arises [8]. The design of the array in terms of the number of elements, their position and input current amplitude allow to precisely control the directivity and side lobe level of the radiation pattern of the array, and increses the sensing range. Furthermore, by controlling the phase-shift between consecutive antennas it is possible to steer the main beam towards a desired direction. This flexibility make planar microstrip patch arrays very suitable to be used in high resolution RADAR applications [1].

An array with a sufficient narrow main-beam, low side lobe level, and with the ability to be steered can provide detailed data about the existence and location of a target for each scanned angular direction. Since the production of the array in this frequency range is expensive due to the high frequency electrical components, a simulation was the chosen solution to obtain the Radar data. $Blender$ is a graphic simulation and ray tracer open source software, that allows to build a 3D environment and freely navigate a camera within, enabling to obtain rendered images from the ray tracer at each camera position. Blender simulations have been previously used to simulate Radars with accurate results [10].

SLAM algorithms are used to solve the problem where a moving object identifies objects to build a map of an unknown environment, while updating its position within that map according to data from accelerometers and gyroscopes. The SLAM is to be performed based on the simulated Radar data obtained as the result of the detection analysis within an environment. The versatility of these algorithms also allow to complement data from multiple sensors. Air vehicles would be able to face unknown environments and reckoning it while travelling, allowing to perform path planning tasks, prevent trajectories that lead to collisions, and display an intuitive map for human operators [11].

1.3 Objectives

The main objective of this thesis is to simulate a radar system navigating in an airspace environment, to identify targets and position them in a common referential, using a system with size and characteristics that are sufficient to be used in air vehicles as a safety feature.

Great emphasis is to be given to the design of a single patch antenna at the desired frequency of operation, to the design of a highly directive and low side lobe planar phased array, to the design and simulation of the mm-Wave Radar system in a known 3D environment, and to the fundamentals of the SLAM algorithm application to the simulated data.

The single patch antenna element design is made in *Matlab* and it is modelled and optimised in *CST Studio Suite*, which is the chosen electromagnetic field simulation software. Three models that resonate at the same frequency were made using three different substrate heights, with the objective of analysing the effect of the substrate height on the radiation pattern and antenna size. Some tests with different line feeds are also made using coaxial and microstrip line feeds, with the purpose of identifying the effect of feed type in the single element. Furthermore, since a radar with a linear polarization can miss targets due to polarization changes of the eletromagnetic waves when reflecting from an object [12], a dual linear polarization patch antenna is desired to minimize this effect. The goal is to obtain an optimised antenna that radiate at the desired frequency in both the horizontal and vertical polarization to decrease the probability of missing a target due to changes in the polarization of the propagated wave.

An array consisting of N elements of the optimised patches, is to be designed and fed with a non-uniform excitation to achieve high directivity and low side lobe level. Furthermore, to control the direction of the main lobe, a phase shift in the feed current must be applied between consecutive antennas. The goal of this design is to achieve characteristics that allow to steer the main lobe both vertically and horizontally while maintaining a low side lobe level and a high directivity of the main lobe for both vertical and horizontal polarizations, allowing to identify targets with accuracy and some detail.

The fundamentals of a mm-Wave Radar using a phased array antenna are presented, and a Frequency Modulated Continuous Wave (FMCW) Radar model described. Unfortunately, the whole array won't be fabricated, and a simulation of a Radar system with the characteristics of the designed array will be performed. A 3D scene is to be created in *Blender* software and a camera is to be used to acquire the image seen from the camera position, along with data of the distance to each visible target, for each pixel, obtained during the render process. The rendering results are to be post-processed based on the characteristics of the designed array, with the objective of acquiring data that mimics the real Radar system on the simulated environment. The goal is to simulate the radar signal for each scanned direction, based on the rendering results and on the radiation patterns of the designed array, to use the simulated signal to process target detection algorithms, and position the detected objects in a map, according to the position of the camera during the render.

Furthermore, SLAM algorithms can be used to create a map of the environment, based on the results of the radar simulations.

1.4 Main Results of the Thesis

The present work is divided into the design of a single antenna element, the design of an antenna array and the simulation of a radar system, being the objectives achieved throughout it given as follows.

- The patch antenna is successfully designed, being the design versatile in terms of resonant frequency.
- The antenna array is successfully designed, using narrow-beam low side lobe design with steering capabilities.
- The radar system is simulated in a known environment, identifying objects according to its position.

The implementation of the SLAM algorithm using the simulated data wasn't accomplished.

1.5 Thesis Structure

The first chapter describes the motivation and the objectives of this work. It also summarises the main results obtained and the structure of the thesis report.

In Chapter 2, a bibliographic review of the most relevant aspects to develop throughout this work is done, being divided into the general purpose of the thesis, the design of a microstrip antenna and of an antenna array, and the radar system fundamentals and simulation.

In Chapter 3, the theoretical foundations for the design and optimisation of a microstrip patch antenna are presented, along with the development of a model of a single antenna, and simulation results of the developed model.

In Chapter 4, the theoretical foundations for the design of a generic antenna array are presented, as well as for a non-uniform excitation of the antenna array elements, and for the steering of the main lobe of the array. An array is modelled using a number of the elements obtained in Chapter 3, and the results of the simulation of the array are presented. Due to the different steering angles, several results were obtained, being depicted in Appendix A.

In Chapter 5, the working principle of a mm-Wave radar is presented, along with the theoretical foundations needed to perform the radar simulation, using the array designed in Chapter 4. The simulation concepts and methods are also detailed in this chapter, along with the radar simulation results.

Since the concepts developed in chapters 3, 4 and 5 are quite distinct, each chapter contains its own discussion and possible future work. However, in Chapter 6, the conclusions of the overall work are presented.

Chapter 2

State of the art

In this chapter, a Literature Review related to the general concept of this work is done, followed by a review of the state of the art of the necessary specific fields divided into two categories: Antenna and Array Design and mm-Wave FMCW Radar Fundamentals and Simulation.

Some On-board Terrain Mapping Systems (OTMS) to identify targets are being developed and used nowadays for automotive applications. This systems are subdivided into an object detecting module and a mapping module, in which a Radar have been successfully tested as part of the detecting module [13] [14].

G. Ludeno et Al. [15] made an experiment using a single radar in a hexacopter. A Ultra Wide Band (UWB) radar was used, with an operating frequency between 3.1 GHz and 4.8 GHz. The experiment was made in an open space with 4 reflecting obstacles. It transmits a chirp signal from 3.4 GHz to 4.6 GHz, and a radar image was collected where it was possible to identify the objects.

Alistar Moses et Al. [16] develop a miniature radar system, working at 10.5 GHz, to be used in aircrafts with less than 25kg. The radar sensor used allow range and velocity detection of the target. The system consists of a RF front end module, an ADC, and a PC to process information, then noise is eliminated through a Finite Impulse Response filter. Tests were made in a controlled environment, in which a quad-rotor wants to identify a miniature helicopter, at approximately 7 m of distance. After calibration, the target was correctly identified.

Malcom Mielle et Al. [7] made 3 experiments with a Lidar and a Radar indoors, with and without smoke, to compare the reliability of both sensors in adverse atmospheric conditions. The sensor's data were used to perform SLAM algorithms and create a map of the environment. The RADAR system used were a Mechanically Pivoting Radar (MPR), with a rotation speed of 2.5 Hz (200 measurements per 360º, once every 1.8º), with 3.75 cm of accuracy up to 19 m of range. Although the low resolution of the MPR, it was able to accurately perform the SLAM and build a map of the environment under both circumstances (including corners and small walls).

Young K Kwag et Al. [17] used a radar with an antenna array operating at a frequency of 35 GHz, having 2.5° of mainbeam beamwidth, with a 5 kHz Pulse Repetition Frequency (PRF), scanning at $150^\circ/s$. The goal was to implement it on UAVs with a low flying nature to avoid the collision against obstacles. The UAV considered had a maximum speed of 500 km/h. The article objectives were based on the Equivalent Level of Safety (ELOS) for see & avoid, which had the following minimum requirements: A search volume of $+$/- 60º in Azimuth and $+$/- 10º in Elevation and a minimum time to collision of 21 seconds for a detection of an object. The objective is to have a system that provides range, azimuth, elevation and velocity of obstacles through the Radar sensor, and the Obstacle Collision Avoidance System hold the collision criteria and sends a command to the digital Air Data Computer based on the time to collision (which varies with relative velocity between obstacles and range).

Intensive work is being done lately regarding environment identification with different types of sensors due to the recent Advanced Driver Assistance System (ADAS) technology. However, in order to achieve a higher level of reliability, the AAV systems must use a combination of Radars, Lidars and Cameras sensors. Jorge Vargas et al. [18] stated that with state of the art technology, the safest and most reliable way to position an object within an environment is to first position the object using Global Navigation Satellite System (GNSS) technology and then update its position with data measured from Inertial Measurement Unit (IMU), Lidar, Radar and Camera sensors. There is also a summary of the weather effects on the different types of AAVs sensors, and the conclusion was that Radar was the state of the art sensor to reliably operate under adverse weather conditions for these purpose. However, Radars were still criticised by their need of an auxiliary sensor for object perception assistance. [19]

2.1 Antenna and Array Design

Patch antennas consist of a radiating element supported by a dielectric substrate above a ground plane and are easily produced with Printed Circuit Technology. It is one of the most revolutionary antenna technologies ever [20]. Patch antennas usually have a small bandwidth, and the limiting factors for operating frequency are usually its physical dimensions, being those limited by the precision and accuracy of the production machine. At high frequencies, electrical losses become noticeable and must be taken into account in the design procedure [21].

The resonant frequency of an antenna is affected by, and have effect in many factors. Stéphane Kemkemian et Al. [22] carried out an operating frequency analysis in 3 different frequencies. The pros and cons of a radar operating at 3 GHz (S-Band), at 10 GHz (X-band - classical airborne radar band) and at 35 GHz (Ka-band, millimetre waveband) are developed, without taking frequencies regulations into account. It defines a cylindrical area around the aircraft that is the safety area in which no obstacles can exist. To the radar system it is required at minimum a revisit time of 2 seconds and a minimum of 20 seconds advance when an obstacle is identified inside the safety area. The 3 GHz radar has as advantage the possibility of creating a non ambiguous waveform both in range and velocity, but has very low angular resolution due to the limited size, which allow the use of less antennas. The 10 GHz radar has as advantages the possibility to form narrower beams than the 3 GHz, but needs a larger number of antennas and therefore more physical space when comparing to the same beamwidth with 35 GHz antennas. The 35 GHz radar was studied using a mechanically pivoting transmissor and with a fully static solution. The fully static with mechanical pivoting was the chosen solution for this work, due to its advantages such as good angular accuracy, high gain, but turned out to need a higher power to identify targets for a determined range than the previous solutions.

Regarding design methods, there are uncountable methods to design a resonant patch. Siakavara in [23] describes many orthodox design methods, adaptable to different requirements, proving once again the versatility of patch antennas. To design simple shaped patches, one of the most common used method is the Transmission Line Model, in which the patch is assumed to be a part of a transmission line. Despite existing more accurate design methods, with the state of the art electromagnetic wave propagation simulators available, this method is accurate enough to provide an initial estimation and then the dimensions are adjusted in the simulator in order to obtain an optimised antenna. Another design method often considered to be used is the Cavity Model, in which the patch is modelled as a cavity bounded by an electric conductor ceiling and floor, and surrounded by magnetic walls [20]. This method is very useful to determine the radiation pattern of each resonant mode of the patch. The Transmission Line Model and the Cavity Model design methods are often used together [24].

To transfer power to the Microstrip patch antenna, a feeding point is needed. Many feeding techniques exist, but the most common are [8] [24]:

- Microstrip Line - Thin printed line above the dielectric substrate that connects to the coaxial cable and to the patch.
- Coaxial Probe - Coaxial cable that goes through the ground plane and the dielectric substrate and connects directly to the desired feed point on the patch.
- Proximity Coupled Feed - Model with two substrates, in which a microstrip line is placed in between the two substrates, the patch is on the upper substrate and the ground is under the lower substrate. The coaxial cable connects to the microstrip line doesn't connect directly to the patch.
- Aperture Coupled Feed - Model with two substrates, in which the ground plane is in the middle of the substrates, the patch is on the upper substrate and the microstrip line is placed under the lower substrate. The ground plane has an aperture (slot) through which the patch is energised. There is no direct contact between the microstrip line and the patch.

However, when feeding a patch, one has to make sure that the impedance of the transmission line and the point where the energy is transfered to the patch are compatible. This is done by impedance matching, there are also many ways to match impedance as explained in [25]. Coaxial Probe feeding is the simplest to match for low frequency patches, since the coaxial cable is inserted directly to the point on the patch with the desired impedance. Microstrip Lines have well known impedance matching techniques such as a transformer, a tuning stub or a matching network, which are applicable to every feeding type that involves microstrip lines, being possible to obtain near perfect matches.

A system intended to identify targets should take into account that when an eletromagnetic wave reflects on a target at certain incident angles, a portion of the reflected signal polarization become the orthogonal of the incident wave polarization, which can lead to the loss of a target due to polarization mismatch [26]. The polarization of the signal radiated from a patch antenna depends on the feeding point position, for coaxial proble feeding, or orientation of the feed line, for microstrip line feeding. Shah in [27] with the purpose of developing Multiple Input Multiple Output (MIMO) wireless communications systems, designed a dual linear polarized patch antenna array. The Transmission Line Model was used to design a squared patch fed with inset feed to resonate at 2.4 GHz. The patches were positioned at an angle of $\pm 45°$ and were coupled in a 1x2 array in order to achieve different polarizations in each array. A 1x2 array and 2x2 array with patches aligned at $+45°$ and at$-45°$ were also tested, and a radiation pattern with dual linear polarization, low cross polarization and relative high gain was obtained in both cases. Note that despite the great results, the designed array is not supposed to be used in a highly directive Radar system, and does not take into consideration the side lobe level, which is affected by using a 2x2 array as a single element in a bigger sized array.

Christopher Smith in [28] designed a single dual linear polarized patch to ressonate in the X-band (8 to 12 GHz) with the purpose of providing a verified design method to obtain dual linear polarized patch antennas for mobile phones or satellite communications. The Transmission Line Model is once more used to design the squared patch, and an aperture coupled feed was used connected to two coaxial cables, one responsible for each polarization. The result was an antenna that resonate at 9,30 GHz with a simillar radiation pattern for both polarizations, low cross polarization between ports, and a good impedance matching between the aperture coupled feed and the patch.

Microstrip antennas can be used in many array configurations, in planar or spherical surfaces [29]. There are 3 types of feeding each element in an array: independent feed, series feed or parallel feed. Independent feed is the case in which each element is fed by an independent coaxial cable, and its phase and current amplitude can be well controlled [30]. If consecutive antennas of an array are fed in series, each antenna will have a phase shift on the received signal, and therefore the main lobe of the radiation pattern will be steered. If the antennas of an array are all fed by a parallel feed in which the length of the transmission line is the same from the power source to each antenna, all antennas are fed with the same phase, and the radiation pattern has its main lobe centered [24].

Series and parallel array feed configurations are tested in [31], using patch antennas that resonate at 2.5 GHz, being noticeable the difference in gain, return loss and other performance characteristics between each feeding method. Midasala in [32] simulated a 3x3 patch array at Ku-band (12 to 18 GHz) fed with independent coaxial cables, in order to obtain a phased array system. Since each antenna is fed by a current that can be adjusted in terms of amplitude and phase, it is possible to steer the main lobe of the radiation pattern of the array by inserting different phase shifts between consecutive antennas, without the need for a mechanical structure to rotate the array [33].

Current amplitude of each element of an array can also be controlled, which gives the ability to impose desired characteristic on the radiation pattern of the array regarding directivity and/or side lobe levels [34]. In this work, a narrow beam low side lobe radiation pattern is desired. The four commonly used designs are: Uniform, Dolph—Chebyshev, Taylor—Kaiser and Binomial. The difference between these designs is the different trade-off between main-beam beam width and side lobe level. Uniform design outputs the narrowest main-beam width but the highest side lobe levels, Dolph-Chebyshev design outputs the narrowest main-beam achievable for a given side lobe level, Taylow Kaiser design outputs a slightly larger main-beam than the Dolph-Chebyshev design, however the side lobes furthest from the main lobe have a much better behaviour, and binomial design outputs no side lobes at all, but has the widest main-beam width [30].

Dolph-Chebyshev arrays have been used for a long time [35], and is a very well mathematically formulated design. In [36] a Dolph-Chebyshev array with periodic spacing between elements is synthesized, with the objective to control the array radiation pattern. The paper also proposes a method to implement the array using a Field Programmable Gate Array (FPGA) that is supposed to control each attenuator and phase shifter to deliver the desired current amplitude and phase to each element in the array.

Patch antennas are commonly used in phased arrays with single element phase controlled excitation in order to steer its main lobe towards a desired direction. In [29] different consecutive phase shifts are applied to a 5x5 patch array with successful steering achieved, relating the desired scanning angle with the antennas phase shift. However, when steering an array to angles closer to the array plane, a deformation of the main lobe appears due to wave interactions between array elements. The phenomena that lead to this behaviour are discussed in [37], and it is also shown that when steering the main lobe to angles close to the array plane, undesired modes are propagated from the antennas and the reflection coefficient is affected, sometimes leading to very weak propagated signals.

In [9] Jin Song et al. designed a 77 GHz rectangular patch antenna array with microstrip line feed. Each single antenna has sides with lengths less than 1.4 mm, making it suitable for building an array with many antennas to acquire higher directivities while keeping the array with a size applicable to many situations. The result were a high gain and directive array, that resonate at 77 GHz with low bandwidth and a side lobe level of -24.5 dB, using non-uniform Dolph-Chebyshev feeding excitation distribution, with 64 antennas occupying 33 mm x 22 mm width and length, respectively.

2.2 mm-Wave FMCW Radar Fundamentals and Simulation

The mm-Wave frequency, or Extremely High Frequency (EHF) band, is defined between 30 GHz and 300 GHz and is a special class of Radar technology due to the shorter wavelength of the transmitted signals. The transmitted waves have different propagation characteristics to take into consideration when comparing to the regularly used Ultra High Frequency (UHF) band (from 600 MHz to 3 GHz), such as a higher atmospheric absorption, rain attenuation and path losses. Due to the short wavelength, distance measurement cannot be achieved with a single frequency, and a frequency modulated signal (chirp) must be considered to use. There are also many advantages of mm-Wave Radars, such as the enhanced capabilities achieved with digital beamforming in phased arrays, due to the possibility to deploy a higher number of elements in the same spatial dimentions as UHF arrays, leading to a better control of the radiation pattern characteristics [38]. Another advantage of working with a short wavelength signal is the high accuracy, being able to detect movements that consist of fraction of milimeters [39]. Despite higher attenuations, mm-Wave Radars are still able to provide reliable data under conditions in which optical sensors would not [40].

Frequency Modulated Continuous Wave (FMCW) Radars are almost as old as the Radar itself, and usually operate by transmitting pulses of a certain frequency modulated signal (e.g. a linearly modulated Chirp signal). The operational principle behind FMCW Radars is explained in [41]. FMCW Radars have a simple and compact architecture, consisting of a signal generator, an antenna to transmit and to receive the signal, a mixer to extract the instantaneous frequency difference between transmitted and received signal, which is nearly constant over each chirp and proportional to the target range, followed by ADCs and by a processing module. Another advantage of FMCW Radars is the ability to take advantage of the Doppler effect to obtain the target velocity, by comparing the phase shift between a consecutive sequence of chirp signals sent to a single direction [39]. Furthermore, phased arrays are commonly fed with FMCW modulated signals in low-powered antennas, such as patch antennas [42].

mm-Wave FMCW Radars are already being used to identify objects position and motion to avoid collisions in industrial environments [43]. One key aspect for a system to make a real-time decision regarding changing its position safely is to have knowledge of what surrounds it. This kind of Radars are also used in the automotive industry to avoid collision between moving vehicles [44]. Note that these are active sensors, that operate independently of the surroundings.

The signal generator component of a phased array FMCW Radar is usually implemented with a FPGA in order to obtain a real time electronically steered array. A mm-Wave transmitter based on FPGA is designed in [45], containing an intermediate frequency module composed by the FPGA and some digital to analog converters (DAC), that outputs the desired IF signal to transmit, a local oscilator module that provides the carrier wave signal and a mixer module to modulate the IF signal. In [46] a review of full duplex mm-Wave systems is done. Despite a good isolation in full duplex phased array still being challenging to achieve, using a Silicon on insulator Complementary metal–oxide–semiconductor (SOI-CMOS) is proven to output good results [47].

To implement a phased array, one must apply a phase shift between each element. Phase shifting is often obtained by two methods, either by inserting a programmable phase shifter between the output from the FPGA and the mixer for each antenna (in this case, the FPGA only outputs one signal and the phase shifters need to be controlled), or by time-delaying the output signal directly on the FPGA, in which the FPGA has one output signal for each antenna [48]. Note that both configurations would need one gain amplifier per antenna, to implement the weights to be fed to each antenna according to the used feeding technique of the array [49].

A mm-Wave Radar receiver with digital beamforming using a highly directive phased array impose the transmission and processing of a big amount of data. Thus, the desired is to have a high signal aquisition rate on the ADCs and DACs, and a high transfer rate and processing speed on the system. A realization of a digital beamforming receiver system is presented in [50], in which the signal from the ADCs that is received on the FPGA is sent over Ethernet to a PC in which all the processing is done.

Simulation is a reliable and cheap way to solve a certain real-world problem, and is widely used when designing Radio Frequency (RF) components. There are several open source Radar signal simulation software, e.g. $gprMax$, and toolboxes, e.g. $Radar\ System\ Design$ from $MathWorks$. However, they focus on the electromagnetic propagation of the Radar signals, and do not allow the creation of a 3D environment to freely navigate. Ray tracers have previously been used to perform Radar simulations, with the objective of simplifying the model and computational burden [51].

$Blender$ has also been used to perform Radar simulations within a defined environment, mostly due to its 3D creation and ray tracing capabilities and to the incorporated Python API. A concept of Radar simulation using $Blender$ is done in [52], using the software to create a simple environment and using the ray tracer in real-time to emulate the electromagnetic signal, allowing to perceive reflected, refracted and diffracted signals. The electromagnetic wave source is a light source, and the arrival point is a camera, which are set to be on the same position, being analogous to an antenna transmitting or receiving in the real-world. A real-world Radar was simulated, and the obtained simulation results were in agreement with the real working behaviour of the Radar. This method was further enhanced and detailed in [53], in which Doppler frequency analysis, materials configuration and signal reconstruction were added, with the purpose of providing a general Radar simulation tool for Synthethic Aperture Radar Imaging or cross-section measurement, requiring knowledge of ray tracing algorithms.

A simpler tool for Radar simulation in Blender is presented in [51], in which the Radar signal is created outside of $Blender$, interacting with the scene data with the $BlenderPythonAPI$. The ray tracer is not used directly in this paper, instead, the rendered images output by it are used. This method is simpler since it does not require any specific knowledge on ray tracers to perform the simulation. However, it does not account for refracted nor multiple-reflected signals. The group light source + camera can be moved around the scene, and by rendering each step it is possible to acquire the necessary rendered images to be further processed. The simulations are done assuming that the scene is stationary and the radar is moving and that the objects lie in the far-field of the Radar. The FMCW Radar model used is described in [54]. It only takes into consideration the gain and half-power beam-width angles of the radiation pattern of the array, and the position of each antenna. A chirp signal is used. The range data is obtained from the the phase shift between one transmitted and received chirp, and the velocity data is obtained from the frequency shift of detected targets between a sequence of chirps. This is explained in detail in [55]. The data is processed pixel by pixel to obtain the simulated raw signal, which is the coherent sum of the signals for each pixel. The Rendered images were exported as Open-EXR format [56] due to its high dynamic range format, in order to obtain a more accurate simulation. As limitations, the paper describes the model lacking gain specification for each direction, and multi-path propagation/penetration of signals, which is a consequence of avoiding the direct use of the ray tracer.

An image is obtained as the rendered output by $Blender$. Thus, in order to process the desired radiation patterns in the image, the projection between the radiation patterns and the rendered images must match, in order for the processing to be done pixel by pixel. Many image projections and a comparison between them are presented in [57].

SLAM algorithms require knowledge of the position and attitude of the system in each time instance, along with the data obtained from the system sensors, in order to create a 3D map of the environment. In real systems, one of the most challenging aspects in SLAM algorithms is the odometry (position estimation from motion sensors) drift correction. Usually, an IMU is used to provide accurate odometry data to these algorithms [58]. With the system position and attitude computed, the following challenge is to convert a position relative to a local referential to an universal referential, in which the targets identified at the different positions are combined. 3D transformations allow to convert the point from one referential to another [59].

Chapter 3

Microstrip Patch Antenna Design

In this chapter, the transmission line and cavity models are studied to design a squared patch antenna with dual linear polarization, along with the implementation of a quarter wavelength transformer to optimise impedance matching between the transmission lines and the load. The model is validated by performing simulations using the electromagnetic field simulation software $CST\ Studio\ Suite$.

3.1 Theoretical Background

3.1.1 Microstrip Patch Antennas Simple Design Models

The antenna is to be designed in terms of shape, substrate dielectric constant (ϵ_r), substrate height (h), patch length (L), patch width (W), inset feed length (L_1), transmission line width (W_0) and patch resonant frequency (f_r). The transmission line model and the cavity model provide well-known formulas to obtain initial estimations for these variables, used to perform the pre-designing of the single element.

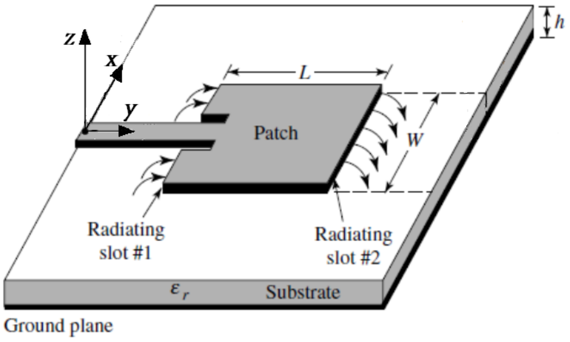

Figure 3.1: Orthogonal view of a generic square patch with reference axis (extracted from [8])

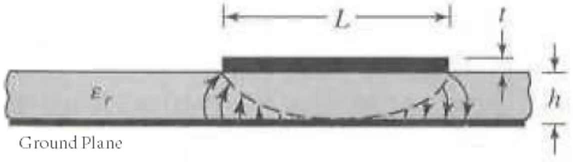

Figure 3.2: Side view of a generic square patch (extracted from [8])

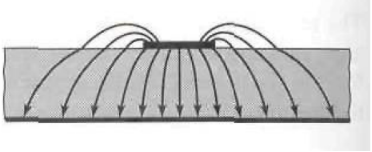

Figure 3.3: Eletric field path with fringing (extracted from [8])

Transmission Line Model

Figures 3.2 and 3.3 illustrate the electric field lines of a microstrip that undergo fringing. Fringing is a well known effect that happens due to the nature of patch antennas, that creates a non-homogeneous electrical path between two dielectrics (the air and the substrate). Due to fringing, electrically the patch looks larger than its physical dimensions, phenomena that affects the resonant frequency of the patch. As the height of the substrate increases, fringing also increases [8].

To account for fringing, it is assumed that the patch is embedded into a homogeneous substrate with an effective dielectric constant ϵ_{reff}. This way, the electrical fields that undergo fringing are analysed as propagating in the same material with one propagation constant, avoiding the analysis of the non-homogeneous field path between air and substrate, as illustrated in figure 3.3. The wavelength propagating in the free-space λ_0 is only dependent on the resonant frequency, being the relation specified in equation 3.1. However the wavelength propagating in the embedded substrate λ_g is also affected by the substrate characteristics [8], being obtained using equation 3.2.

$$\lambda_0 = \frac{c}{f_r} \tag{3.1}$$

$$\lambda_g = \frac{\lambda_0}{\sqrt{\epsilon_{reff}}} \tag{3.2}$$

Despite the effective dielectric constant being influenced by the frequency of the antenna, an estimation can be obtained by one of the following equation:

$$\epsilon_{reff} = \begin{cases} \frac{\epsilon_r+1}{2} + \frac{\epsilon_r-1}{2}\left[1+\frac{12h}{W}\right]^{-1/2}, & W \geq h \\ \\ \frac{\epsilon_r+1}{2} + \frac{\epsilon_r-1}{2}\left[(1+\frac{12h}{W})^{-1/2} + 0.04(1+\frac{W}{h})^2\right], & W < h \end{cases} \tag{3.3}$$

The frequency of operation of the antenna influences the way eletric field lines behave. As the frequency increases, the more the eletric field is concentrated in the substrate and the effective dieletric constant approaches the value of the dieletric constant of the substrate [8]. A graphical representation of this effect is presented in figure 3.4. Note that, since the model is to be optimised using the electromagnetic field simulation software (*CST Studio Suite*), there is no need to take this effect into consideration when pre-designing the element.

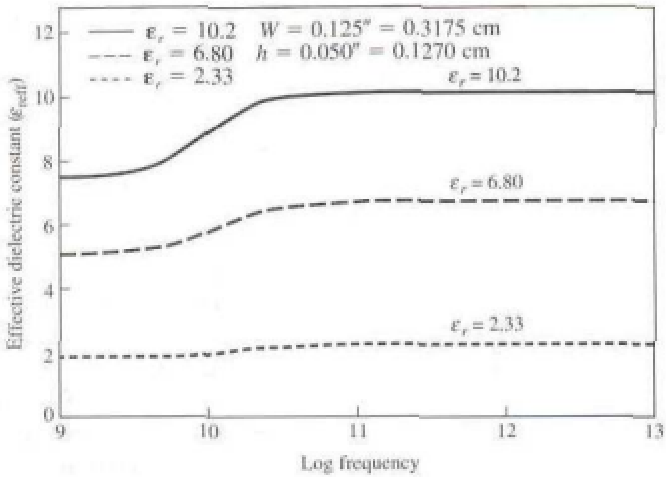

Figure 3.4: ϵ_{reff} vs frequency of operation (extracted from [8])

To account for fringing, an extension along the length of the element for each side is considered. The effective length of the patch L_{eff} is given by

$$L_{eff} = L + 2\Delta L, \tag{3.4}$$

where L is its physical length. The extension along the length of the antenna ΔL is a function of ϵ_{reff} and of the ratio W/h, given by:

$$\Delta L = 0.412h\frac{(\epsilon_{reff}+0.3)(\frac{W}{h}+0.264)}{(\epsilon_{reff}-0.258)(\frac{W}{h}+0.8)} \tag{3.5}$$

Analysing a patch antenna using the *Transmission Line Model* leads to the representation of the patch as an array of two radiating slots along its width W , separated by a transmission line of length L, with a low impedance Z_c (thus high admittance Y_c). Each radiating slot is represented by a parallel equivalent admittance Y, with susceptance B and conductance G_r, as illustrated in figure 3.5.

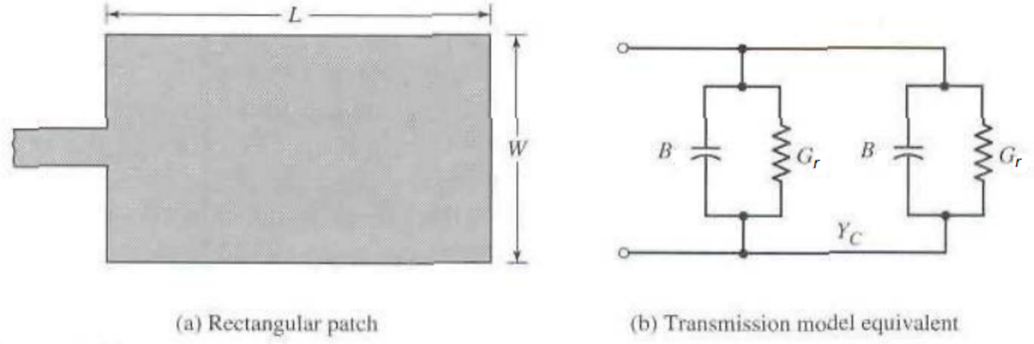

(a) Rectangular patch (b) Transmission model equivalent

Figure 3.5: Equivalent radiating slots of a patch antenna (extracted from [8])

The conductance G_r and the susceptance B represent, respectively, the radiation losses and the edge effects on each radiating border of the patch [8], and for patches with $h < 0.1\lambda_0$ are expressed by:

$$\begin{aligned} G_r &= \frac{W}{120\lambda_0}\left[1-\frac{(k_o h)^2}{24}\right] \\ B &= \frac{W}{120\lambda_0}\left[1-0.636\ln(k_0 h)\right] \end{aligned} \tag{3.6}$$

Based on the equivalent model in figure 3.5, the input admittance of the patch Y_{in} is given by

$$Y_{in} = (G_r + jB) + Y_C\frac{(G_r+jB)+jY_C\tan(k_g L_{eff})}{Y_C + j(G_r+jB)\tan(k_g L_{eff})},$$

being $k_g = k_0\sqrt{\epsilon_{reff}}$ the wavenumber within the embedded substrate, and k_0 the wavenumber in the free-space given by equation 3.7.

$$k_0 = \frac{2\pi}{\lambda_0} \tag{3.7}$$

Considering $Y_C \gg G_r, B$, leads to $k_g L_{eff} \simeq \pi$. The resonant condition of the patch is then expressed by:

$$Im(Y_{in}) = 0 \Longleftrightarrow Y_{in} = 2G_r \tag{3.8}$$

Thus, the resistance at resonance at the radiating edges of the patch R_0 is:

$$R_0 = \frac{1}{Y_{in}} = \frac{1}{2G_r} \tag{3.9}$$

However, it is possible to control the input resistance by connecting the transmission line to a recessed inset feed, at a distance L_1 towards the center of the patch, as illustrated in figure 3.1. The resulting input resistance is

$$R_{in} = R_0 \cdot \cos^2(\frac{2\pi}{\lambda_g}L_1) \tag{3.10}$$

A microstrip transmission line is to be used to connect the coaxial cable to the inset feed point. The characteristic impedance of a microstrip transmission line, is calculated by one of the following equations [8]:

$$Z_0 = \begin{cases} \frac{120\pi}{\sqrt{\epsilon_{reff}}} \left[\frac{W}{h} + 1.393 + 0.667\ln\left(\frac{W}{h} + 1.444\right)\right]^{-1}, & W \geq h \\ \\ \frac{60}{\sqrt{\epsilon_{reff}}} \ln\left(\frac{8h}{W} + \frac{W}{4h}\right), & W < h \end{cases} \tag{3.11}$$

Cavity Model

This model analyses the patch as a cavity with perfectly conducting electric borders on top and bottom and perfectly conducting magnetic lateral walls, with the same dimensions as the patch to analyse. It shows that the cavity radiate through 4 slots along the perimeter of the patch, in which the radiation vectors from the slots along its length cancels in the principal planes. Considering the patch represented in figure 3.1, the principal planes are the yz-plane or E-plane, and the xz-plane or H-plane.

The cavity is assumed to only radiate through the slots along its width, as represented using the transmission line model (figure 3.5).

The field configuration mode TM_{mnp} within the cavity affects the resonant frequency of the patch. The mode can be found by relating the eletric and magnetic fields within the cavity to a potential vector A_x that must satisfy the homogeneous wave equation

$$\nabla^2 A_x + k^2 A_x = 0 \tag{3.12}$$

As described in detail in section 14.2.2 of [8], by applying boundary conditions given by the cavity properties, the final form of the potential vector is:

$$A_x = A_{mnp}\cos(k_x x)\cos(k_y y)\cos(k_z z), \tag{3.13}$$

which is only valid while x, y, z are inside the cavity. A_{mnp} represents the amplitude coefficient of each mnp mode. The wavenumbers along x, y and z are related to the field mode as follows:

$$\begin{cases} k_x = \frac{m\pi}{W}, & m = 0, 1, 2, ... \\ k_y = \frac{n\pi}{L}, & n = 0, 1, 2, ... \\ k_z = \frac{p\pi}{h}, & p = 0, 1, 2, ... \end{cases}, \tag{3.14}$$

where m, n, p represent the number of half-cycle field variations (zeros) along the x, y, z directions, respectively.

The resonant frequency for each mode is then given by:

$$(f_r)_{mnp} = \frac{1}{2\pi\sqrt{\epsilon_{reff}}\sqrt{\mu_0\epsilon_0}}\sqrt{(k_x)^2 + (k_y)^2 + (k_z)^2}, \tag{3.15}$$

Note that fringing is also accounted for in equation 3.15. The dimensions of the patch are used to determine which mode is dominant. A couple examples of common design configurations are listed below:

- $W > L > h$ - Dominant mode is TM_{100}.
- $L > W > h$ - Dominant mode is TM_{010}.

Since the patch is to be design as a square patch, $W = L$, and the resonant frequency of mode TM_{100} and TM_{010} become approximately the same:

$$(fr)_{100} = (fr)_{010} = \frac{\pi}{2\pi W\sqrt{\epsilon_{reff}}\sqrt{\mu_0\epsilon_0}} \tag{3.16}$$

This allows for a patch to resonate at the same frequency when fed by two independent transmission lines, one at each border, one for vertical polarization and the other for horizontal polarization. However, when modelling a patch with two polarizations, there's a need to adjust the resonant frequency of each polarization individually, which is possible due to the fact that each mode will be controlled by each polarization.

This model also sketches the fields radiated by the microstrip patch. This is described in [8] as well, however the analysis of the radiation pattern of the patch will be done using the software CST Studio Suite. The directivity of the single element is limited due to the nature of patch antennas, thus its value depends on how optimized the element is. The assymptotically values for the directivity of a patch antenna are given by [8]:

$$D_0 = \begin{cases} 6.6 = 8.2dB, \;\; W \ll \lambda_0 \\ \\ \frac{8W}{\lambda_0} \;\; W \gg \lambda_0 \end{cases} \tag{3.17}$$

3.1.2 Optimizing Impedance Matching

Impedance matching is used to maximise the power transferred from a generator to a load. Considering an incident power on the load P_{in}, some power will be reflected P_{ref} and some will be transmitted P_{tr}, being the relation given by $P_{tr} = P_{in} - P_{ref}$. The reflection coefficient represents the percentage of the incident power that gets reflected by the load. The following figure illustrates a circuit that connects a generator with voltage V_G and internal impedance Z_G to a load with impedance Z_L, through a transmission line with characteristic impedance Z_0 and length d [60].

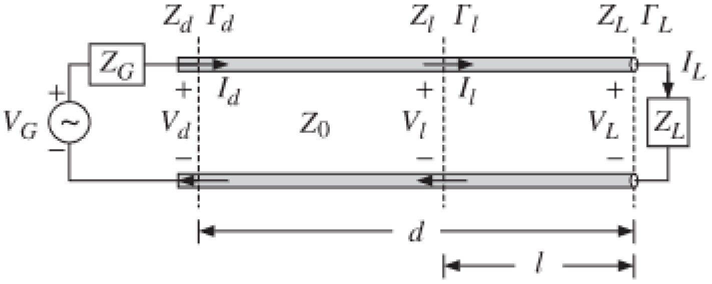

Figure 3.6: Terminated transmission line (extracted from [60])

Since the patch is to be used in an array for radar applications, it will work as a transmitting and receiving antenna. As a transmitting antenna, the transmitter is the generator and the patch the load, however, as a receiving antenna, the patch is the generator and the receiver the load. The load impedance can have a resistive and a reactive part, being represented by $Z_L = R_L + jX_L$. The reflection coefficient at the load is given by:

$$\Gamma_L = \frac{Z_L - Z_0}{Z_L + Z_0} \tag{3.18}$$

The reflection coefficient is usually a complex expression which has a constant absolute value, only varying its phase, and can generically be written as $\Gamma = \gamma e^{j\zeta}$. Thus, if $Z_L = Z_0$ the transmission line is matched and $\Gamma_L = 0$, however, if $Z_L \neq Z_0$, Γ varies periodically along the transmission line. At an arbitrary distance l from the load towards the generator, the reflection factor can be calculated using the following equation:

$$\Gamma(l) = \Gamma_L e^{-j2\pi l/\lambda} = \gamma e^{-j(2\pi l/\lambda - \zeta)} \tag{3.19}$$

The input impedance, however, varies its absolute value and phase with the distance l, and is given by:

$$Z_{in}(l) = Z_0 \frac{1+\Gamma(l)}{1-\Gamma(l)} = Z_0 \frac{Z_L + jZ_0 \tan(2\pi l/\lambda)}{Z_0 + jZ_L \tan(2\pi l/\lambda)} \tag{3.20}$$

Defining now a normalized impedanze $z_{in}(l) = \frac{Z_{in}(l)}{Z_0} = r + jx$, the reflection factor can be stated as:

$$\Gamma(l) = \frac{z_{in}(l) - 1}{z_{in}(l) + 1} \Leftrightarrow z_{in}(l) = \frac{1+\Gamma(l)}{1-\Gamma(l)} \tag{3.21}$$

This allows a mapping between the normalized z-plane and the reflection coefficient Γ-plane, as depicted in figure 3.7:

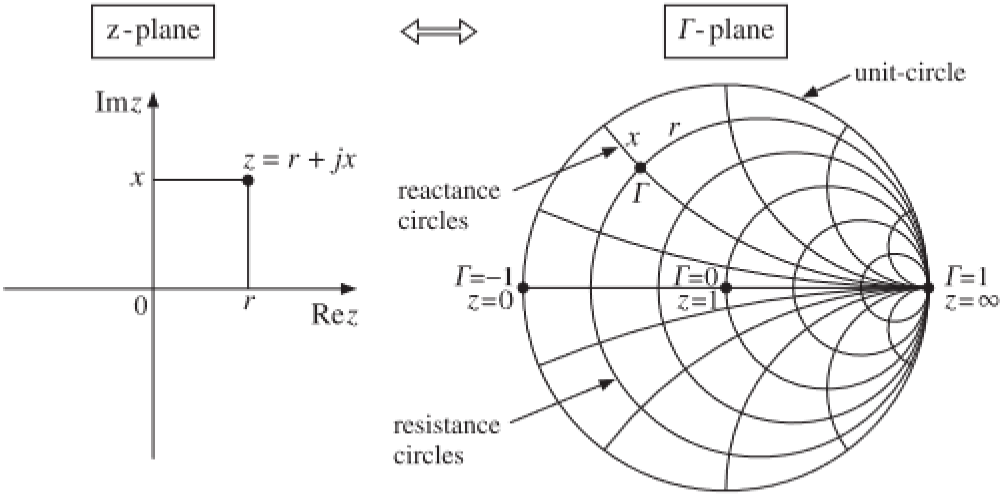

Figure 3.7: Mapping between z-plane and Γ-plane (extracted from [61])

The Smith Chart is a graphical representation of the Γ-plane. The points with constant resistance and constant reactance in the z-plane form the resistance and reactance circles in the Γ-plane, respectively. The center point of the Smith chart corresponds to a well matched impedance, with a null reflection coefficient. Note that for each working frequency there is a point in the Smith chart that corresponds to the reflection coefficient for that frequency. Thus, a sweep over different frequencies will produce a line in the Smith chart.

Once the position of the reflection coefficient at the load Γ_L is marked on a Smith chart for a lossless line, it is possible to predict the position of $\Gamma(l)$ by rotating the initial point around the origin of the chart. A full rotation to the initial point happens when $l = \lambda/2$. At $l = \lambda/4$ from the load a special behaviour happens, and it allows the use of quarter wavelength transformers to match transmission lines with different characteristic impedance.

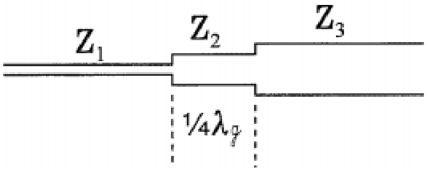

Figure 3.8: Quarter wavelength transformer

A quarter wavelength transformer is depicted in figure 3.8. A transformer with impedance Z_2 is used to convert the impedance Z_3 to an arbitrary impedance Z_1. The length of the transformer is $\frac{1}{4}\lambda_g$, which only has the desired behaviour for the designed frequency. The perfect match occurs when equation 3.23 is satisfied [60].

$$Z_2 = \sqrt{Z_1 Z_3} \tag{3.22}$$

Combining equations 3.20 and 3.22, with $Z_L = Z_3$ the following relation is obtained:

$$z_{in}(\lambda/4) = \frac{Z_2^2}{Z_L} \tag{3.23}$$

Note that by considering Z_3 the load, and Z_1 the main transmission line, equation 3.23 becomes $z_{in}(\lambda/4) = \frac{Z_0 Z_L}{Z_L} = Z_0$.

The Scattering Parameters (S-Parameters) also allow an analysis of the reflection and transmission coefficients of a transmission line. Considering the two-port network in figure 3.9, the S-Parameter relates the outgoing waves b_1 and b_2 to the incoming waves a_1 and a_2.

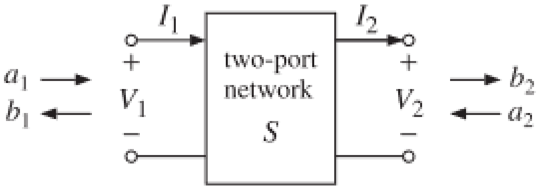

Figure 3.9: Two port network, with ingoing and outgoing waves on each port (extracted from [61])

The outgoing and incoming waves are related by the Scattering Matrix:

$$\begin{bmatrix} b_1 \\ b_2 \end{bmatrix} = \begin{bmatrix} S_{11} & S_{12} \\ S_{21} & S_{22} \end{bmatrix} \begin{bmatrix} a_1 \\ a_2 \end{bmatrix} \tag{3.24}$$

The elements S_{11} and S_{22} represent the reflection coefficients for each port and are very helpful to determine the resonant frequency of an antenna with precision. Then, the Smith chart can be used to minimize the reflection coefficient for the desired frequency. The elements S_{12} and S_{21} represent the transmission coefficients between port 1 and port 2, being useful to verify if a good isolation between ports exists.

3.2 Single Element Pre-Design

In this section the pre-design of a squared patch fed by a microstrip line is done. The desired frequency was to be set within the mm-Wave frequency (EHF band), which have a few propagation characteristics to take into account when designing a highly directive radar, such as higher path loss and atmospheric absorption [38]. The free-space path loss decays with the square of the transmitted frequency, and it's the principal source of power loss in mm-Wave Radars. The atmospheric attenuation is the second major source of power loss in mm-Wave Radars, and to minimize it, the frequency was set to 35 GHz, which has nearly the minimum attenuation for the frequency band $f \in [30, 60]$ GHz [62].

An initial estimation for the patch width is given by:

$$W = \frac{\lambda_0}{2}\sqrt{\frac{2}{\epsilon_r + 1}} \tag{3.25}$$

The effective dielectric constant is calculated using equation (3.3). The effective length of the antenna is given by $L_{eff} = \frac{\lambda_g}{2} = \frac{\lambda_0}{2\sqrt{\epsilon_{reff}}}$, and using equations (3.4) and (3.5) it is possible to calculate the physical length of the patch.

Reiterating this process from equation (3.3) with $W = L$ allows both dimensions to converge to a value, making the patch squared.

Since the patch dimensions are in the mm range, a direct feed from the coaxial cables to the patch is a very rigorous task, and is prone to error. Even if higher impedance coaxial cables, which are thinner, were to be used, since the patch would need two independent coaxial cables to achieve dual linear polarization, the cables would be extremely close in distance. Thus, a coaxial cable will be connected to a microstrip line to feed the border of the patch. The microstrip can either connect directly to the border or to a recessed inset feed.

The inset feed length can be estimated based on equation (3.10) that leads to

$$L_1 = \frac{\lambda_g}{2\pi} \arccos\left(\sqrt{\frac{R_{in}}{R_0}}\right) \tag{3.26}$$

However, since the goal is to have dual-linear polarization, two transmission lines are to be connected to the patch, and the resonant frequency and the radiated fields for each polarization would be affected by the inset feed of the transmission line responsible for the other polarization. Thus, the transmission lines will be matched to the impedance of the border of the patch to minimise the differences between each polarization.

Assuming that the vertical polarization happens when the patch is fed at a border along its width (x-axis), the dominant mode will be the TM_{010}, and mode TM_{100} will be dominant for the horizontal polarization, which happens when the patch is fed at the border along its length (y-axis), as depicted in figure 3.14. The resonant frequency for each polarization have an inversely proportional relationship with the width and length of the patch, and can be tweaked according to the following equations:

$$\begin{aligned} (f_r)_{vertical} &= \frac{\pi}{2\pi L\sqrt{\epsilon_{reff}}\sqrt{\mu_0\epsilon_0}} \\ (f_r)_{horizontal} &= \frac{\pi}{2\pi W\sqrt{\epsilon_{reff}}\sqrt{\mu_0\epsilon_0}} \end{aligned} \tag{3.27}$$

The impedance of the transmission lines that connect to the patch must be matched to the impedance of the border of the patch at resonance, R_0 (equation 3.10). The available coaxial cables are the EZ-47, with $50\ \Omega$, thus a quarter wavelength transformer will be used to transform $50\ \Omega$ to R_0 to feed the patches.

The impedance of the quarter wavelength transformer is calculated using equation 3.22. Then, to calculate the width and length of the transformer, software $AWRTx - Line$ [63] is used. The user inputs the dielectric constant, loss tangent and height, the plate thickness, the impedance of the line, the frequency of operation, and the desired electrical length (90º being a quarter wavelength).

3.3 Single Element Modelling and Simulation Results and Discussion

The chosen substrate is RT/duroid 5880 with a dielectric constant of 2.20 ± 0.015 with a loss tangent @ 10 GHz of 0.0009. The antennas and transmission lines will be made of copper with $0.035\ mm$ of plate thickness. The substrate height is usually in the range of $0.003\lambda_0 \leq h \leq 0.05\lambda_0$. The desired patch resonant frequency is 35 GHz, thus the substrate height must be in the range $[0.0257, 0.4286]\ mm$. The patch will be modelled with substrates of height 0.508 mm, 0.381 mm and 0.254 mm to evaluate its effect on the antenna properties.

A *Matlab* code was developed according to the previous reasoning. One must specify the desired resonant frequency, the substrate dielectric constant and height, and the impedance of the coaxial cable and the code outputs the width W, length L and impedance R_0 of the border of the patch, as well as the impedance of the quarter wavelength transformer to connect the coaxial cable to the border of the patch Z_{qwt}. Then, $Tx - Line2003$ outputs the width W_{qwt} and length L_{qwt} of the transformer. The results are depicted for each substrate height in table 3.1. Note that there is an increase in the patch size, and in the length of the transformer, and a decrease in the width of the transformer as the substrate gets thinner.

h (mm)	0.508	0.381	0.254
W = L (mm)	2.60	2.63	2.67
R_0 (Ω)	198.9	195.7	192.9
Z_{qwt} (Ω)	99.7	98.9	98.2
L_{qwt} (mm)	1.59	1.61	1.63
W_{qwt} (mm)	0.46	0.33	0.20

Table 3.1: Antenna simulation results for different substrate height

Three simple models were made and optimised on $CST\ Studio\ Suite$ to evaluate the radiation pattern for each substrate height. The substrate was modelled as 5 times bigger than the patch width and length, and the patches were fed using a $100\ \Omega$ coaxial cable that was modelled.

The principal planes of the radiation patterns for $h = 0.381$ mm and $h = 0.254$ mm are represented in pictures 3.10, 3.11, 3.12 and 3.13:

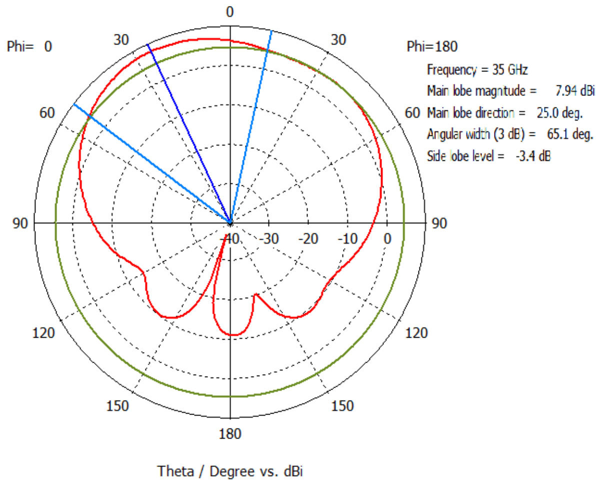

Figure 3.10: E-Plane radiation pattern for $h = 0.381$ mm

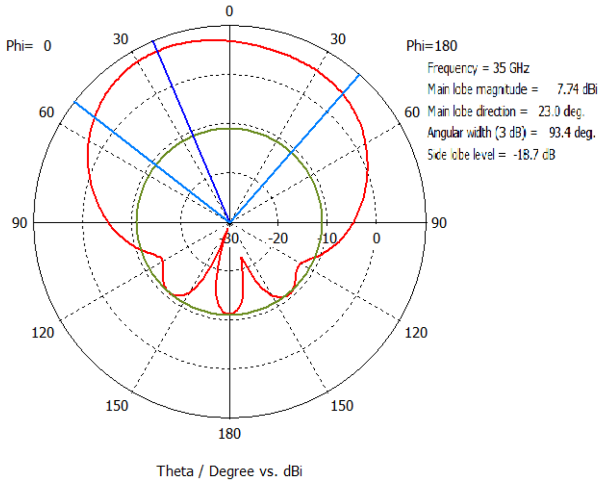

Figure 3.11: E-Plane radiation pattern for $h = 0.254$ mm

The simulations lead to the following conclusions about the influence of the substrate height on the radiation pattern of the single element.

1. The substrate height highly influences the width of the transformer, and it is possible to verify its influence on the E-plane of the radiation pattern (figures 3.10 and 3.11).
2. Without the influence of the transmission line, the directivity increases and the 3dB angular width decreases as the substrate gets thinner (figures 3.12 and 3.13).

The optimised patch width and length, in order to obtain the minimum of $|S_{11}|$ and $|S_{22}|$ at the desired frequency (35 GHz), was 2.665 mm. Note the proximity of this value to the one obtained in table 3.1 for $h = 0.254$ mm.

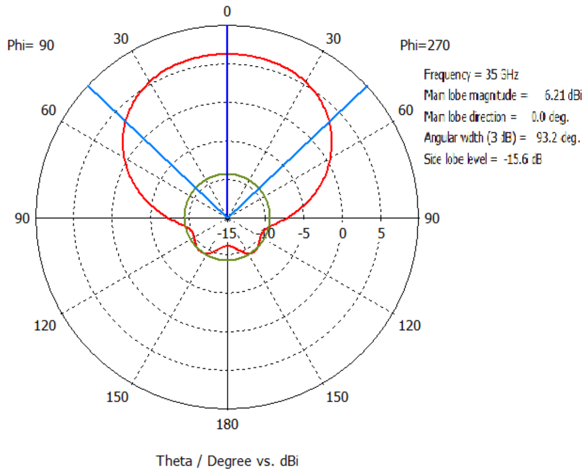

Figure 3.12: H-Plane radiation pattern for $h = 0.381\ mm$

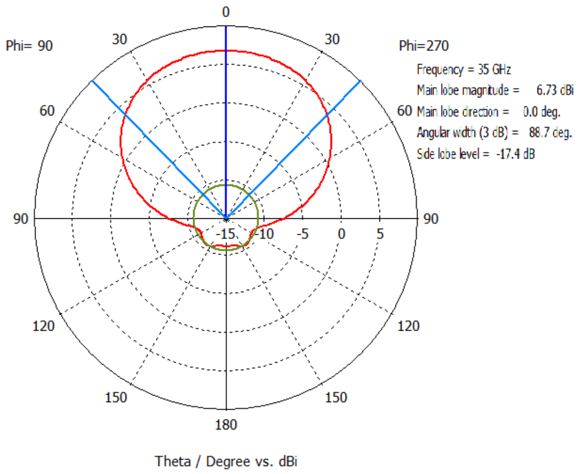

Figure 3.13: H-Plane radiation pattern for $h = 0.254$ mm

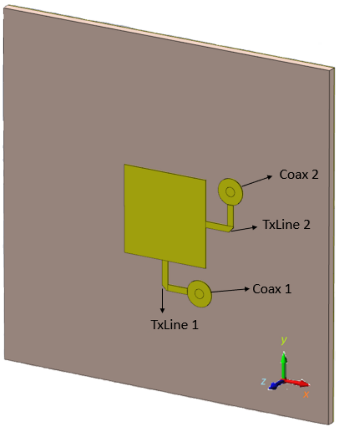

Figure 3.14: Dual linear polarized patch antenna

To minimise the effects of the transmission lines and to achieve a higher directivity the substrate with $h = 0.254$ mm was used for the final single element model, represented in figure 3.14. The antenna consists of the patch, two microstrip lines and two coaxial cables to control both polarizations. Both transmission lines are transforming the $50\ \Omega$ from each coaxial to R_0 in order to avoid using inset feeds to keep the similarity of the radiation pattern between polarizations. Coaxial cables 1 and 2 are stimulated independently to obtain vertical and horizontal polarization, respectively. The xz-Plane corresponds to the H-plane of the vertical polarization and to the E-plane of the horizontal polarization, and the yz-Plane corresponds to the E-plane of the vertical polarization and to the H-plane of the horizontal polarization.

The simulation results regarding vertical polarization are shown in figures 3.15, 3.16, 3.17 and 3.18. The impedance matching between the transmission line and the antenna is verified by the magnitude of the S-Parameter and by the Smith Chart at the frequency of operation, depicted in figures 3.15 and 3.16. Thus, it is possible to conclude that the transmission line successfully transforms the $50\ \Omega$ from the load to the impedance of the border of the patch. In figures 3.17 and 3.18 it is seen the main lobe slightly steered, due to the influence of the transmission lines, that also radiate power. Note that the model was optimised by replacing inset feeds with an appropriate transformer to minimise the influence of the transmission lines on the radiation pattern, as seen when comparing the radiation patterns in figures 3.17 and 3.11.

The results regarding horizontal polarization are shown in figures 3.19, 3.20, 3.21 and 3.22. A good

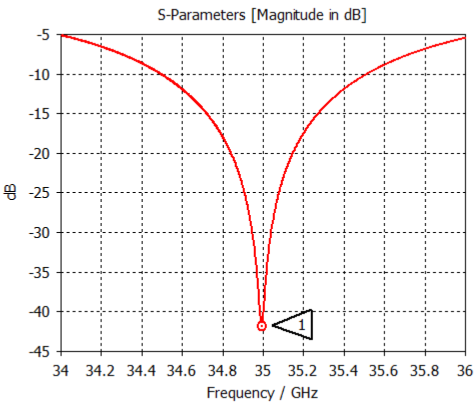

Figure 3.15: Vertical polarization $|S_{11}|$

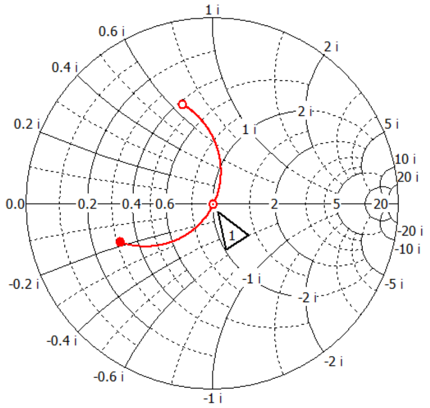

Figure 3.16: Vertical polarization Smith Chart

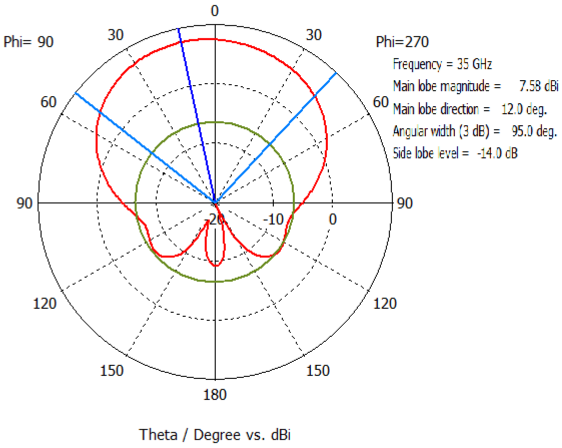

Figure 3.17: Vertical polarization E-Plane radiation pattern

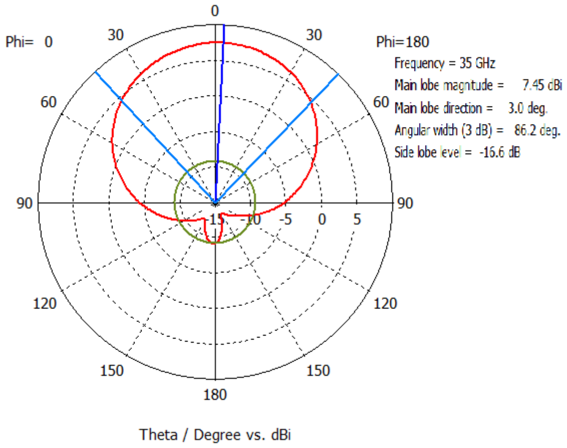

Figure 3.18: Vertical polarization H-Plane radiation pattern

impedance match between the transmission line and the antenna is also verified for this polarization. As noticed in the vertical polarization, figures 3.21 and 3.22 show the main lobe slightly deviated from broadside. Note that for both polarizations and/or designs, this steered angle will become unnoticeable after designing the array.

The antenna has a narrow bandwidth for both polarizations, which is an already known limitation of patch antennas [9][21]. The bandwidth of the array will be slightly larger than the bandwidth of the single element antenna. Considering that the bandwidth is the frequency range where $|S_{11}|$ is below -10 dB, the antenna bandwidth is approximately 1 GHz.

The mutual coupling between ports can be evaluated by analysing $|S_{12}|$ and $|S_{21}|$ parameters (equation 3.24), and are represented in figure 3.23. Any interference lower than -15 dB would be acceptable. The feeds are well isolated, evidencing that the two polarizations could be stimulated independently.

3.4 Discussion and Future Work

Due to the high versatility of patch antennas, the design procedure has slight changes according to the desired shape of the patch. In this chapter, an efficient way to design squared patch antennas was presented, allowing to obtain its physical dimensions, according to the desired final characteristics of the element.

The design of a single patch antenna element was successfully done using the transmission line and cavity

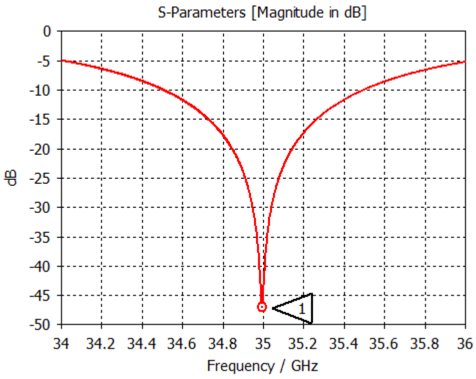

Figure 3.19: Horizontal polarization $|S_{11}|$

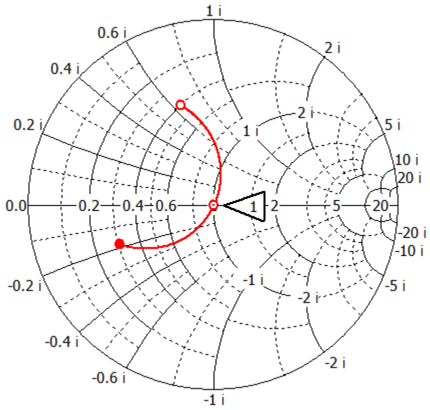

Figure 3.20: Horizontal polarization Smith Chart

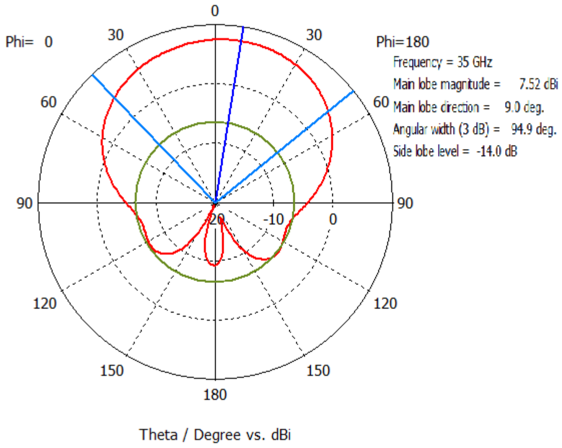

Figure 3.21: Horizontal polarization E-plane radiation pattern

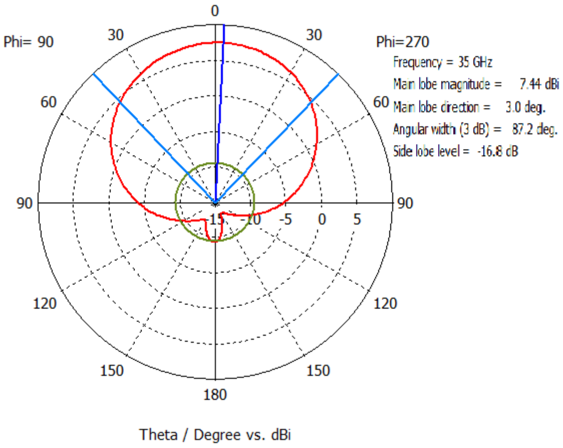

Figure 3.22: Horizontal polarization H-plane radiation pattern

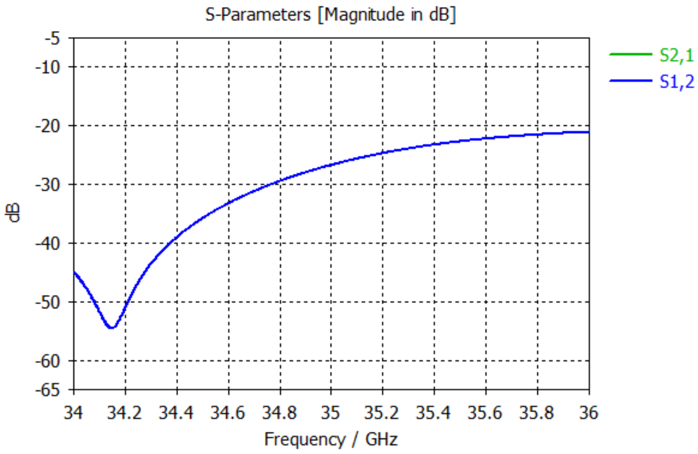

Figure 3.23: Mutual coupling between vertical and horizontal polarization ports

models. By using this models, initial estimations for the physical dimensions of the patch were obtained, according to the desired resonant frequency and taking into consideration the substrate and feed types used. The patch antenna dimensions were further optimised using the software *CST Studio Suite*, to achieve the desired characteristics for the single element. To optimise the antenna radiating properties, impedance matching was performed between the feed line and the patch antenna, to minimise the reflected power and therefore maximise the transmitted power.

Some models were also made to analyse the substrate height influence on the single element radiating properties, allowing to conclude that the thinner the substrate height, the higher the magnitude of the radiation pattern gain.

Finally, a dual linear polarized patch antenna was designed, achieving, for both polarizations, approximately the same resonant frequency, similar radiation pattern characteristics, and a good impedance match between the feed line and the antenna. Due to the dual linear polarization and high frequency of operation, direct feed with a coaxial cable to the patch, or a transmission line with a recessed inset feed on the patch were not suitable to be used, and a quarter wavelength transformer was used to connect each coaxial cable directly to each border of the patch.

Future work in this section could be to increase the resonant frequency of the single element to the band used by the state of the art long range automotive radars, between 76 GHz and 77 GHz [64]. Either proximity coupled or aperture coupled feed should be taken into consideration, to minimise the effects of the feed microstrip lines in the radiation pattern of the single element. Furthermore, the production of antennas with small physical dimensions require a manufacture procedure with high accuracy and precision, and a study of the maximum dimensional error allowed shall also be done, relative to the dimensions of the element to produce.

Chapter 4

Array Design

In this chapter, the a study of an antenna array is done, considering a Dolph-Chebyshev array, with non uniform excitation and main lobe steering.

The first approach to have dual-linear polarization for the final array was to design an array of sub-arrays, with each sub-array having 4 elements and a set of transmission lines that allow each antenna to be fed for vertical or horizontal polarization, as developed in [27]. However, it wasn't possible to achieve a side-lobe level that suits radar applications with this approach.

4.1 Theoretical Background

4.1.1 Antenna Arrays

The single element alone is limited in terms of main lobe directivity and direction control [8], thus, arrays of antennas are used to achieve higher directivities by controlling the number of elements, its position and the current amplitudes of each antenna. Arrays also allow to steer the main lobe towards a desired direction, by controlling the relative current phase-shift between elements.

The displacement between each element in an array defines how the radiation vectors of each antenna interact with the others nearby. The radiation vectors of each antenna shall add constructively in the desired scanning direction, and destructively in other directions [33].

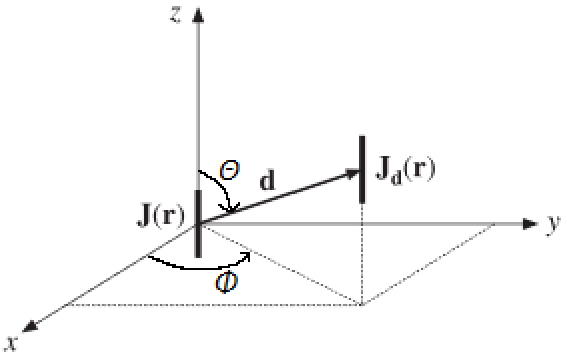

Figure 4.1: Antenna translation by a vector **d**

As depicted in figure 4.1, consider two identical antennas, being one translated by a vector **d**, whose direction is given by the longitude θ and latitude ϕ. Considering that the current density of the antenna at the origin is **J(r)**, the radiation vector **F(k)** of that antenna is defined as the three-dimensional Fourier transform of the current density:

$$\mathbf{F}(\mathbf{k}) = \int_V \mathbf{J}(\mathbf{r}) e^{j\mathbf{k}\cdot\mathbf{r}}\, d^3r,$$

in which **k** is the propagation vector in the direction of the field vector [65]. The radiation vector of the translated antenna $\mathbf{F}_d(\mathbf{k})$ is then given by

$$\mathbf{F}_d(\mathbf{k}) = a_d \mathbf{F}(\mathbf{k}) e^{j\mathbf{k}\cdot\mathbf{d}},$$

being $\mathbf{J}_d(\mathbf{r})$ the current density of the translated antenna

$$\mathbf{J}_d(\mathbf{r}) = a_d \mathbf{J}(\mathbf{r\text{-}d}),$$

with a_d being the relative feed coefficient.

Combinining the radiation vectors of all the antennas in an array yields the radiation pattern of the array. The radiation pattern of an array is also the result of the product between the radiation pattern of the single element and the array factor of the array [33].

The array factor $\mathbf{A}(\theta, \phi)$ of an N-element array is a function of the weights a_n (which define the type of excitation) and position of each element, being defined in equation 4.1. An uniform array has equal weights a_n for all antennas, meaning that each antenna radiates an equal amount of power.

$$\mathbf{A}(\theta, \phi) = \sum_{n=1}^{N} a_n e^{j\mathbf{k}\cdot\mathbf{d}_n} \tag{4.1}$$

Furthermore, the gain of the array $G_{total}(\theta, \phi)$ is related to the gain of the single element $G(\theta, \phi)$ by the power gain of the array $|\mathbf{A}(\theta, \phi)|^2$, being given by equation 4.2.

$$G_{total}(\theta, \phi) = |\mathbf{A}(\theta, \phi)|^2 G(\theta, \phi) \tag{4.2}$$

Considering a one dimensional array along a certain axis, the propagation constants k_x, k_y and k_z, corresponding to the x, y, and z axis are given by:

$$\begin{aligned} k_x &= k_0 \sin(\theta)\cos(\phi) \\ k_y &= k_0 \sin(\theta)\sin(\phi) \\ k_z &= k_0 \cos(\theta) \end{aligned} \tag{4.3}$$

The angular dependence of the array factor comes through the propagation constant k_x, k_y or k_z [33]. Simplifying the design by setting the same inter-element spacing d leads to define an auxiliary variable in the wavenumber space ψ:

$$\psi = \mathbf{k} \cdot d, \tag{4.4}$$

and the array factor from equation 4.1 can be written in terms of ψ as follows:

$$A(\psi) = \sum_{n=0}^{N} a_n e^{jn\psi} \tag{4.5}$$

The array factor $A(\psi)$ is periodic in ψ with period 2π, however, the true range of ψ that affects the physical behaviour of the array is named the visible region, and is defined as the interval $\psi \in [-kd, kd]$. In case the visible region is bigger than the period of $A(\psi)$, the values of the array factor repeat in the visible region, and secondary main lobes (*grating lobes*) arise at different directions than the desired one [33].

The size of the visible region also affects the directivity of the array. An array with N elements will have $N-1$ zeros that will correspond to nulls in the radiation pattern. In order to achieve the maximum directivity and avoid grating lobes, the visible region should reach the last null before the main lobe of the following period in ψ [30].

Usually, equally spaced arrays are defined as symmetrical with respect to the origin of the array axis. However, this leads to an uneven analysis when the number of elements in the array is even or odd, and a redefinition has to be made for each case [30].

The parity of the number of elements in an array dictates the type of analysis. Considering the case of an equally spaced array with an odd number of antennas such that $N = 2M + 1$, the location of each antenna is given by $d_m = md$, with $m = 0, \pm 1, \pm 2, ..., \pm M$, and the array factor $A(\psi)$ (equation 4.1) is rewritten as the following Discrete-Space Fourier Transform (DFT):

$$A(\psi) = a_0 + \sum_{m=1}^{M} (a_m e^{jm\psi} + a_{-m} e^{-jm\psi}), \tag{4.6}$$

whose inverse DFT is given by:

$$a_m = \frac{1}{2\pi} \int_{-\pi}^{\pi} A(\psi) e^{-jm\psi} \, d\psi, \quad m = 0, \pm 1, \pm 2, ..., \pm M \tag{4.7}$$

On the other hand, if the array has an even number of elements $N = 2M$, each antenna will be located at $d_m = \pm(m - \frac{1}{2})d$ with $m = 1, 2, ..., M$, and the array factor is written as:

$$A(\psi) = \sum_{m=1}^{M} (a_m e^{j(m-1/2)\psi} + a_{-m} e^{-j(m-1/2)\psi}), \tag{4.8}$$

whose inverse DFT is given by:

$$a_{\pm m} = \frac{1}{2\pi} \int_{-\pi}^{\pi} A(\psi) e^{\mp j(m-1/2)\psi} \, d\psi, \quad m = 1, 2, ..., M \tag{4.9}$$

Assuming one wants to design an array with an infinitely narrow beam towards some desired direction ϕ_0 (relation with ψ_0 in equation 4.11), the array factor in the wavenumber space and the corresponding inverse DFT are given by:

$$A(\psi) = 2\pi \cdot \delta(\psi - \psi_0) \xrightarrow[\text{DFT}]{\text{inverse}} a(m) = e^{-j\psi_0 m}$$

This leads to an infinite number of weights a_m with $m \in]-\infty, \ \infty[$. An array with a finite number of N elements can be obtained by windowing the solution with an appropriate spatial window w(m), in a way that for the case of odd and even number of elements the solutions are respectively given by:

$$a(m) = e^{-j\psi_0 m} \cdot w(m), \quad m = 0, \pm 1, \pm 2, ... \pm M$$
$$a(\pm m) = e^{\mp j(m-1/2)\psi_0} w(m), \quad m = 0, 1, 2, ..., M$$

Thus, the array factor from equations 4.6 and 4.8 can be rewritten as:

$$A(\psi) = W(\psi - \psi_0),$$

being $W(\psi)$ the inverse DFT of the window function $w(m)$, defined in equation 4.10 for an odd and even N and assuming a symmetric window such that $w(m) = w(-m)$ [30]. The window function $w(m)$ dictates the relation between the main lobe width and the side lobe level of the array, and is defined by the chosen design method.

$$
\begin{aligned}
W(\psi) &= w(0) + 2\sum_{m=1}^{M} w(m)\cos(m\psi), \quad (N\ \ odd) \\
W(\psi) &= 2\sum_{m=1}^{M} w(m)\cos((m-1/2)\psi), \quad (N\ \ even)
\end{aligned} \tag{4.10}
$$

As a further simplification to describe the steering capabilities of an array, consider the array symmetrical along the x-axis (where $\theta = 90$), such that the array factor is measured along ϕ (on the xy-Plane of figure 4.1). Its maximum is $A(0)$, which corresponds to $\psi = k_0 d\ cos(\phi) = 0$ or $\phi = 90$. By applying a phase shift between consecutive antennas, the maximum of the array factor will be steered towards a certain angle ϕ_0. The corresponding steering phase ψ_0 to be applied between consecutive elements is given by

$$\psi_0 = k_0 d\ \cos(\phi_0) \tag{4.11}$$

Figure 4.2 illustrates the difference on the array factor for a beam steered towards $\phi = 90^{\text{o}}$ or towards another arbitrary angle.

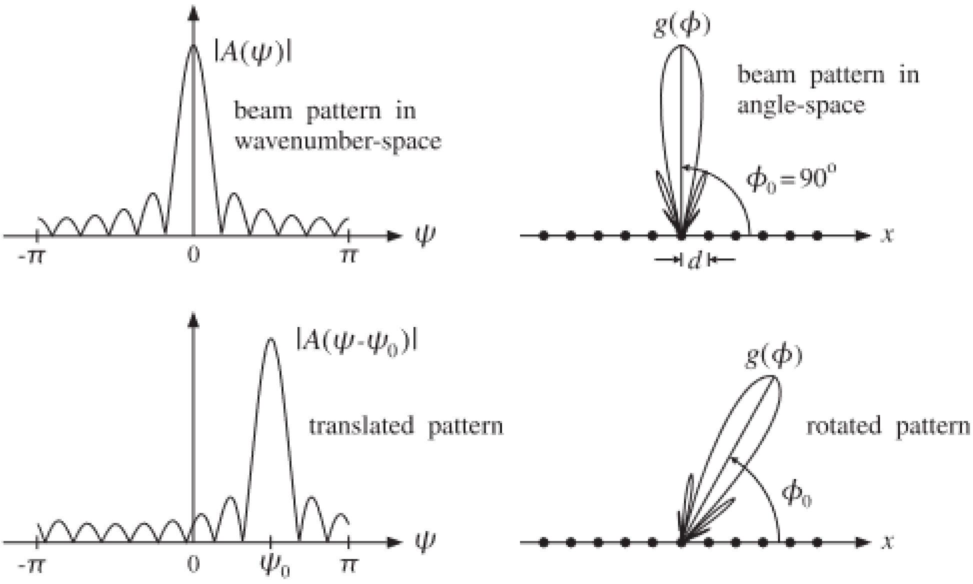

Figure 4.2: Non-steered vs steered patterns (extracted from [33])

The translated digital wavenumber is defined as $\psi' = \psi - \psi_0$ and the steered array factor is given by:

$$A'(\psi) = A(\psi - \psi_0) \tag{4.12}$$

The weights coefficients for each antenna of the steered array are defined as

$$a'_n = a_n e^{-j\psi_0 n} \tag{4.13}$$

being ψ_0 the phase shift between consecutive elements and a_n the weight of the non-steered array.

For the steered array, the visible region shifts accordingly to the angle ϕ_0. The visible region is defined in the wavenumber-space as the phase shift ψ_0 in the interval

$$\psi_0 \in [-kd(1 + \cos(\phi_0)),\ kd(1 - \cos(\phi_0))] \tag{4.14}$$

and to ensure that no grating lobes exist, the maximum spacing between elements d must be:

$$d_{max} = \frac{\lambda}{1 + |\cos((\phi_0)_{max})|} \tag{4.15}$$

being $(\phi_0)_{max}$, the maximum desired steering angle. Once d is established, the visible region in 4.14 can be represented in the angle-space as the angle ϕ_0 in the interval

$$\phi_0 \in [\arccos(\frac{\lambda}{d} - 1),\ 180 - \arccos(\frac{\lambda}{d} - 1)] \tag{4.16}$$

.

Regarding the conversion between the pattern in the wavenumber-space and in the angle-space, the beamwidth relation is given by

$$\Delta\phi = \begin{cases} \frac{1}{k_0 d\sin(\phi_0)}\Delta\psi, & if\ \ 0 < \phi_0 < 180 \\ \\ 2\sqrt{\frac{\Delta\psi}{k_0 d}}, & if\ \ \phi_0 = 0, 180 \end{cases} \tag{4.17}$$

which is normally measured at the 3-dB width or at the width between nulls of the main lobe.

The side lobe level of the radiation pattern of an array is another parameter that must be took into consideration for radar applications. It relates the magnitude of the main lobe to the magnitude of the biggest side lobe. Its absolute value is defined as:

$$R_{abs} = \max\left|\frac{A(\psi_i)}{A(\psi_0)}\right|\ ,\ i = 1, ..., N-1 \tag{4.18}$$

In order to use an antenna in a radar system, the side lobe level must be low enough to avoid false detections. An uniform linear array with high number of elements has the limited capability to achieve a maximum side lobe level of $-13\ dB$ [33]. Thus, to achieve lower side lobe levels, a non-uniform excitation must be considered.

4.1.2 Dolph-Chebyshev Non-Uniform Excitation

The Dolph-Chebyshev excitation provides a definition of the window $w(m)$ (to be used in equation 4.10) such that the main lobe directivity is optimized for a given side lobe attenuation. The window $W(\psi)$ for the Dolph-Chebyshev array is related to the Chebyshev polynomials of first kind $T_{N-1}(x)$, defined in equation 4.19, with x_0 being the scale factor.

$$W(\psi) = T_{N-1}(x), \qquad x = x_0\cos(\frac{\psi}{2}) \tag{4.19}$$

The Dolph-Chebyshev window $W(\psi)$ is defined such that the main lobe corresponds to a portion of the Chebyshev polynomial in the region where $x > 1$ and the side lobes correspond to a portion of the polynomial in the region where $|x| \leq 1$. The Chebyshev polynomials of the first kind are defined in equation 4.20.

$$T_m(x) = \begin{cases} \cos(m \cdot \arccos(x)), & if\ |x| <= 1 \\ \cosh(m \cdot \text{arccosh}(x)), & if\ |x| > 1 \end{cases} \tag{4.20}$$

These polynomials have some well defined properties [66] [30], being a few concepts listed below:

- By setting $x = \cos(\theta) \Leftrightarrow \theta = \arccos(x)$ it is possible to define the first two Chebyshev polynomials as:

$$T_0(x) = 1$$
$$T_1(x) = x$$

- The Chebyshev polynomials have a recursive relation expressed by:

$$T_{n+1}(x) = 2xT_n(x) - T_{n-1}(x)$$

- For $|x| < 1$ the polynomials have ripples with the same amplitude, whereas if $|x| > 1$ it increases like x^m
- The polynomial $T_m(x)$ is even if x is even, or odd if x is odd.

The interval $[x_{min},\ x_0]$ can be split into two subintervals, $[x_{min},\ 1]$ and $[1,\ x_0]$, corresponding to the side lobe and main lobe interval of the array factor, respectively. For an angle $\phi \in [0°,\ 180°]$, the wavenumber $\psi = kd\cos(\phi)$ will range over the visible region. The quantity x will start at the value of x_{min}, and after it reaches the value of x_0, which corresponds to having $\phi = 90°$, x will move back until it reaches the value of x_{min} again, making the zeros of the Chebyshev polynomial the zeros of the array factor at each side of the main lobe, as depicted in Figure 4.3.

The value of $W(\psi)$ at $x = x_0$ correspond to the relative side lobe attenuation level in absolute units [30]. The scale factor x_0 is always greater than 1, and thus, the window W_{main} at $\psi = 90°$ or $x = x_0$ is defined as:

$$W_{main} = \cosh((N-1) \cdot \text{arccosh}(x_0)) \tag{4.21}$$

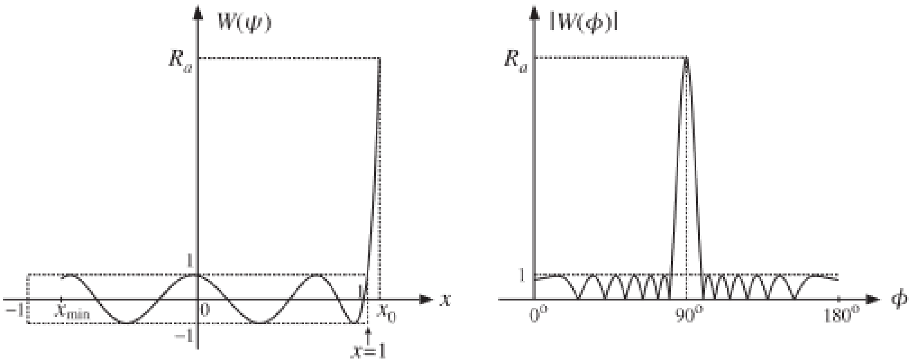

Figure 4.3: Chebyshev polynomials to array factor in wavenumber-space (extracted from [30])

Based on equation 4.18, the side lobe level of the array is given by:

$$R_a = \frac{W_{main}}{W_{side}} \tag{4.22}$$

with $W_{side} = 1$, being R_{abs} the relative side lobe atenuation in absolute units, converted to dB using equation 4.23.

$$R_{abs} = 20\log_{10}(R_a) \tag{4.23}$$

Combining equations 4.20, 4.19 and 4.22, result in the following relation that allow to design the array by defining the desired side lobe level atenuation:

$$R_a = \cosh((N-1)\text{arccosh}(x_0)) \Leftrightarrow x_0 = \cosh(\frac{\text{arccosh}(R_a)}{N-1}) \tag{4.24}$$

The Dolph-Chebyshev window function $w(m)$ is obtained by computing the z-transform of the computing the inverse z-transform of the z-transform of the array factor, constructed from its zeros. In the region of the $N-1$ zeros, the window $W(\psi)$ is defined as:

$$W(\psi) = \cos((N-1) \cdot \arccos(x)) \tag{4.25}$$

The the $N-1$ zeros x_i of $W(\psi)$ are found to be:

$$x_i = \cos(\frac{(i-1/2)\pi}{N-1}), \quad i = 1, 2, ..., N-1 \tag{4.26}$$

Solving for each wavenumber using $x_i = x_0\cos(\psi_i/2)$, the pattern zeros ψ_i are obtained:

$$\psi_i = 2\text{arccos}(\frac{x_i}{x_0}) \tag{4.27}$$

Being each pattern zero represented in the z-space as $z_i = e^{j\psi_i}$. The symmetric z-transform of the window $W(z)$ is constructed with equation 4.28.

$$W(z) = z^{-(N-1)/2}\prod_{i=1}^{N-1}(z - z_i) \tag{4.28}$$

The inverse z-transform of 4.28 gives the window coefficients normalised to unity, that differ from the ones in equation 4.10 by the scale factor $\frac{x_0^{(N-1)}}{2}$.

4.2 Dolph-Chebyshev Squared Array Modelling and Results

In this section, the design and model of a squared array using the previously designed patch antennas with Dolph-Chebyshev non-uniform excitation is done. The *Matlab* "Electromagnetic Waves & Antennas" toolbox from [67] was used to create a script that simulates the theoretical radiation pattern and outputs the Dolph-Chebyshev weights for a linear array, given the desired number of elements N, inter-element spacing d, side lobe attenuation level Ra, and main lobe direction ϕ_0. The script was done according to the reasoning of section 4.1.2.

The maximum spacing between elements can be calculated using equation 4.15. For a steering angle $\phi_0 \in [30°, 150°]$, the maximum distance between elements is $d_{max} = 0.5359\lambda$. For the final array, d was set to $d = 0.5\lambda_0$. The distance between elements affects the visible region of the array, which have a direct effect on the array directivity. Using $0.5\lambda_0$ as inter-element spacing is a very common practice, and usually outputs balanced results [9]. The desired side lobe attenuation level was set to $R_a = 25$ dB to be suitable for Radar applications. The main lobe direction was set to $\phi_0 = 90°$, being orthogonal to the array plane. Several number of elements N were tested, the principal plane of the radiation patterns for $N = 8$, $N = 16$ and $N = 32$ are depicted in figure 4.4, and the relevant results represented in table 4.1.

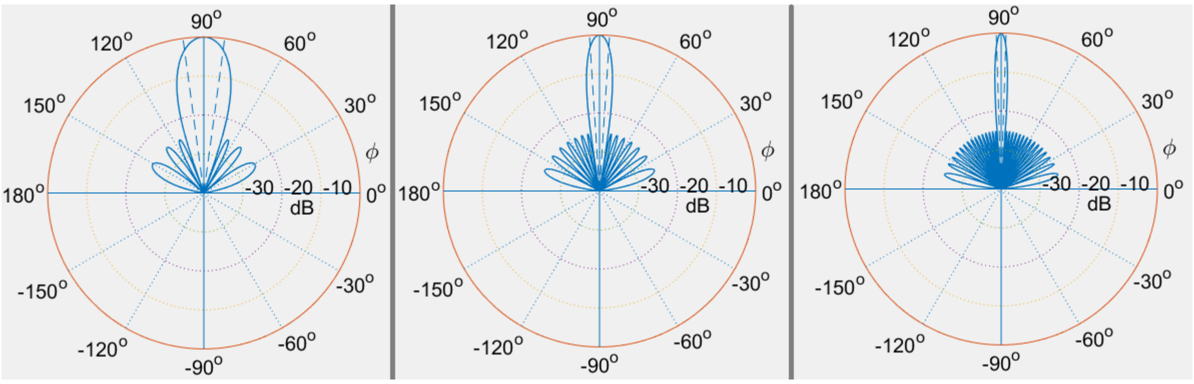

Figure 4.4: Theoretical radiation patterns for N = 8, 16, 32, respectively

N	8	16	32
Array size (mm)	42.80	77.04	145.52
Half-power Beam-width (°)	15.36	7.40	3.61

Table 4.1: Theoretical results for arrays with different number of elements for $f = 35\ GHz$

Note that the Half-power Beam-width results from table 4.1 are considering an isotropic antenna. When simulating the array with the previously designed antennas, the directivity of the single element will slightly increase the directivity of the whole array.

A linear array with $N = 8$ was designed in *CST Studio Suite* using the microstrip patch from section 3.3 as an array element, the model is depicted in figure 4.5.

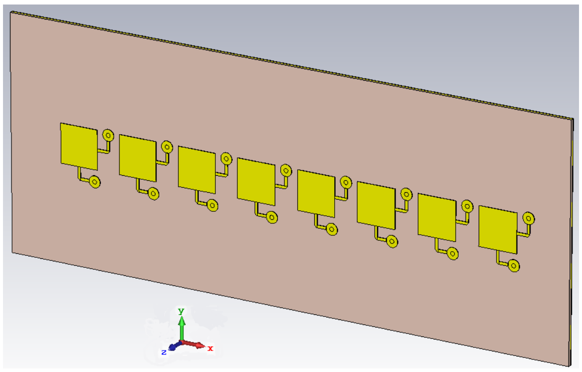

Figure 4.5: Linear array with 8 elements

The simulation was done using the Dolph-Chebyshev coefficients for the vertical polarization feed of the antennas, and the results are represented in figures 4.6, 4.7 and 4.8. The Dolph-Chebyshev coefficients for an array with 8 elements and $R_a = 25$ dB were computed using the reasoning in section 4.1.2, and are represented in table 4.2.

a_1	a_2	a_3	a_4	a_5	a_6	a_7	a_8
1.00	1.55	2.23	2.65	2.65	2.23	1.55	1.00

Table 4.2: Dolph-Chebyshev coefficients for a linear array with $N = 8$ and $R_a = 25dB$

The Half-power Beam-width of the simulated array is $13.3°$ instead of $15.36°$ predicted in table 4.1, which is expected since the directivity of the single element is higher than the directivity of an isotropic antenna. The side lobe level obtained was -24.4 dB, being the back-lobe the side lobe with higher magnitude, behaviour that could be caused by a short modelled coaxial cable feeding each antenna in the simulator. The impedance matching between each port and respective antenna is verified by the magnitude of the reflection coefficients S_{ii} at operating frequency 35 GHz, depicted for the vertical and horizontal polarization ports in figures 4.7 and 4.8, respectively. Only the first four elements are analysed, since the reflection coefficient would be identical for the last four elements due to the symmetry of the array. The mutual coupling from the first element to every other element is shown in figure 4.9, proving that the antennas are well isolated around the operating frequency.

A squared array with 8x8 elements was modelled, and is depicted in figure 4.10. A squared array is a linear array of linear arrays, and the side lobe levels have to be controlled for both axis of the array. Thus,

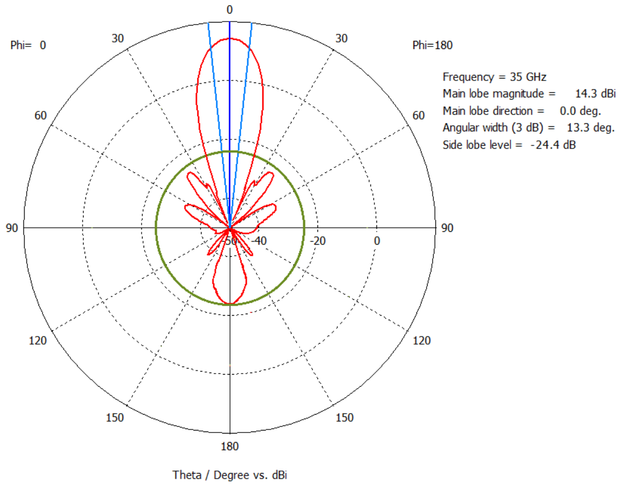

Figure 4.6: Simulated array pattern of a linear array with 8 elements

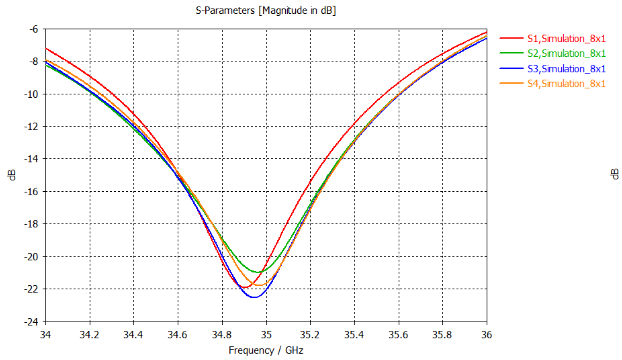

Figure 4.7: $|S_{ii}|$ for vertical polarization of elements i = 1, 2, 3, 4

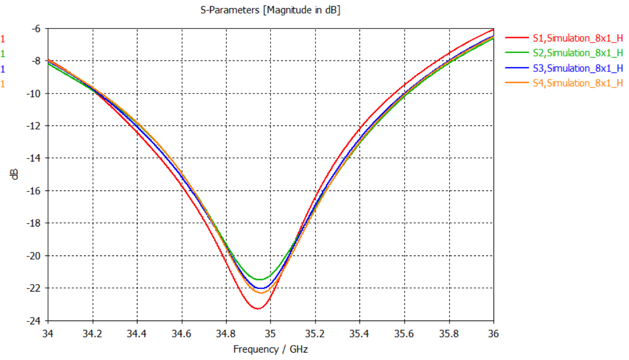

Figure 4.8: $|S_{ii}|$ for horizontal polarization of elements i = 1, 2, 3, 4

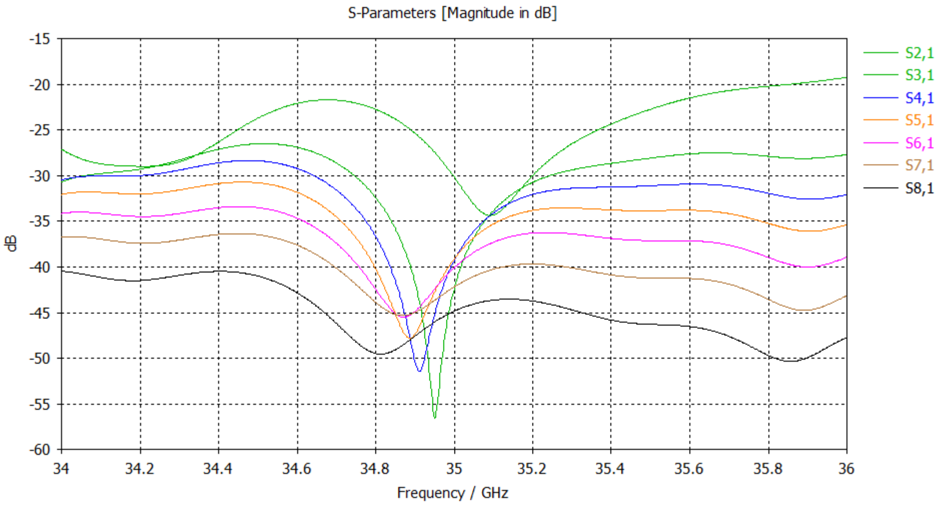

Figure 4.9: Mutual coupling from the first antenna to the following ones

the weights for each element should be influenced by the element position according to each axis, in order to have higher weights at the centre of the array and lower ones as closer the element gets to one of the 4 corner elements, which have unitary weights. This effect is represented conceptually along with the whole array in figure 4.10.

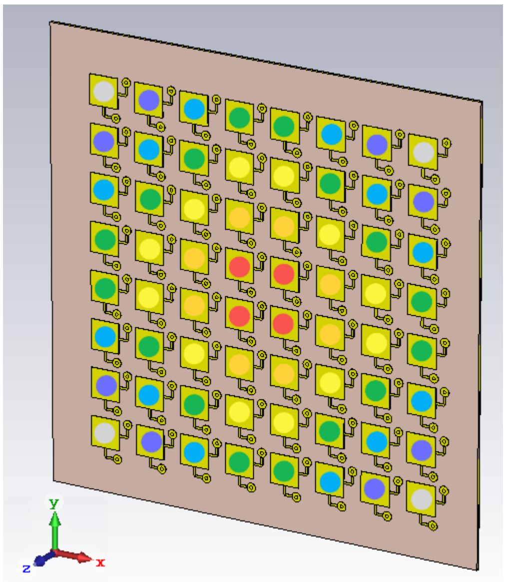

Figure 4.10: Squared array with 8x8 elements and conceptual feed weights technique

Considering the numbering from 1 to 8 of the elements from left to right in the x-axis, and top to bottom in the y-axis, the weight of each element can be referred as a_{ij}, with $i, j \in [1, 8]$. The weights for each element of the 8x8 array are related to the weights of the linear array in table 4.2 by equation 4.29.

$$a_{ij} = a_i \times a_j, \quad i, j \in [1, 8] \tag{4.29}$$

The coefficients for an 8x8 array with $R_a = 25$ dB are exhibited in table 4.3, and the simulation results for the squared array are hereby presented. Due to the symmetry of the squared array, to evaluate impedance matching, the reflection coefficients are analysed for the elements with weights a_{11}, a_{12}, a_{13}, a_{14}, a_{22}, a_{23}, a_{24}, a_{33}, a_{34} and a_{44}, with respect to table 4.3 and to figure 4.10. The reflection coefficients are represented in figure 4.11 for the vertical polarization and in figure 4.12 for the horizontal polarization. The magnitude of the reflection coefficient at the operating frequency is suitable for the desired purpose, and the array achieved a bandwidth of approximately 1.5 GHz, from 34.3 to 35.8 GHz for the vertical polarization and from 34.2 to 35.7 GHz for the horizontal polarization. A maximum reflection coefficient of -10 dB were considered for the bandwidth of the array.

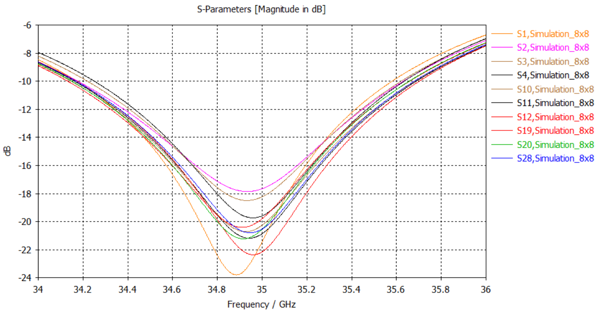

Figure 4.11: $|S_{ii}|$ of elements with vertical polarization with symmetry in the 8x8 array

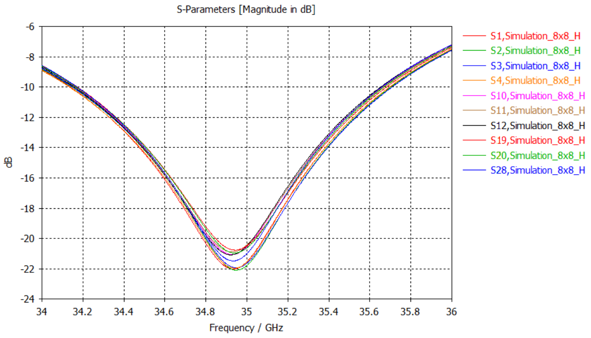

Figure 4.12: $|S_{ii}|$ of elements with horizontal polarization with symmetry in the 8x8 array

Figure 4.13 shows the 3D radiation pattern of the array, figures 4.14 and 4.15 the principal planes of the radiation pattern for the vertical polarization and figures 4.16 and 4.17 the principal planes of the radiation

a_{ij}	a_{i1}	a_{i2}	a_{i3}	a_{i4}	a_{i5}	a_{i6}	a_{i7}	a_{i8}
a_{1j}	1.00	1.55	2.23	2.65	2.65	2.23	1.55	1.00
a_{2j}	1.55	2.40	3.46	4.11	4.11	3.46	2.40	1.55
a_{3j}	2.23	3.46	4.97	5.91	5.91	4.97	3.46	2.23
a_{4j}	2.65	4.11	5.91	7.02	7.02	5.91	4.11	2.65
a_{5j}	2.65	4.11	5.91	7.02	7.02	5.91	4.11	2.65
a_{6j}	2.23	3.46	4.97	5.91	5.91	4.97	3.46	2.23
a_{7j}	1.55	2.40	3.46	4.11	4.11	3.46	2.40	1.55
a_{8j}	1.00	1.55	2.23	2.65	2.65	2.23	1.55	1.00

Table 4.3: Dolph-Chebyshev coefficients for a squared array with 8x8 elements and $R_a = 25$ dB

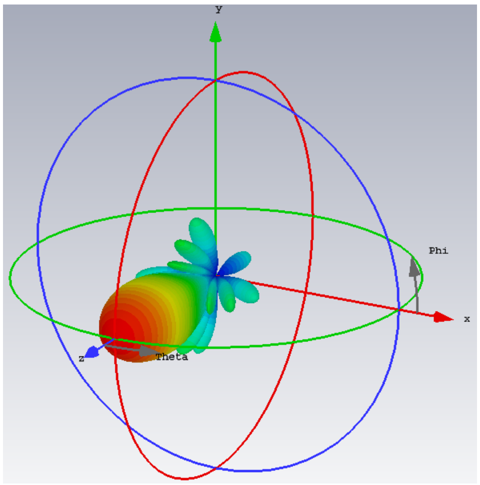

Figure 4.13: Orthogonal view of the 3D radiation pattern simulated for the 8x8 squared array

pattern for the horizontal polarization. The radiation pattern for vertical polarization and for the horizontal polarization of the squared array are nearly identical, as expected from the results obtained in section 3.3. The desired minimum side lobe levels are achieved for both polarizations. For the vertical polarization, the side lobe levels are -25.9 dB for the E-plane and -25.7 dB for the H-plane, along with a main lobe magnitude of 22.9 dBi for both planes and a Half-power Beam-width of $15.1°$ for the E-plane and $15.0°$ for the H-plane, being very close to the Half-power Beam-width shown in table 4.1. Regarding horizontal polarization, the side lobes level are -25.5 dB for the E-plane and -25.8 dB for the H-plane, with a main lobe magnitude of 22.2 dB for both planes and a Half-power Beam-width of $15.0°$ for the E-plane and $15.1°$ for the H-plane. Note how the radiation patterns and characteristics of the E-plane of the vertical polarization are similar to the characteristics of the H-plane of the horizontal polarization, and the other way around. The array was successfully stimulated with two different independent polarizations.

4.3 Steering the Dolph-Chebyshev Squared Array Model

Once the planar array is designed and simulated with the main lobe orthogonal to the array plane, it's time to analyse its steering capabilities. Since the vertical and horizontal polarization are proved to be very similar (figures 4.14, 4.15, 4.16 and 4.17), the results shown in this section are only regarding vertical polarization.

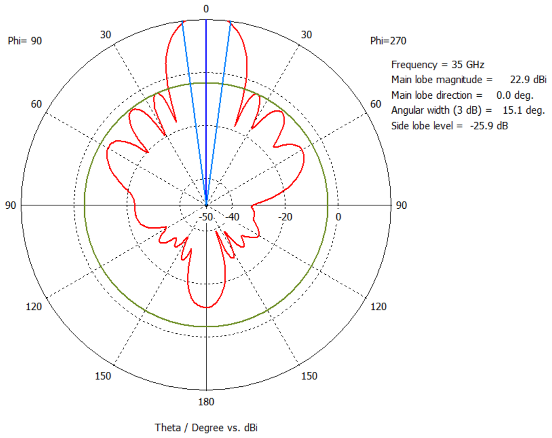

Figure 4.14: Squared 8x8 array radiation pattern E-Plane - vertical polarization

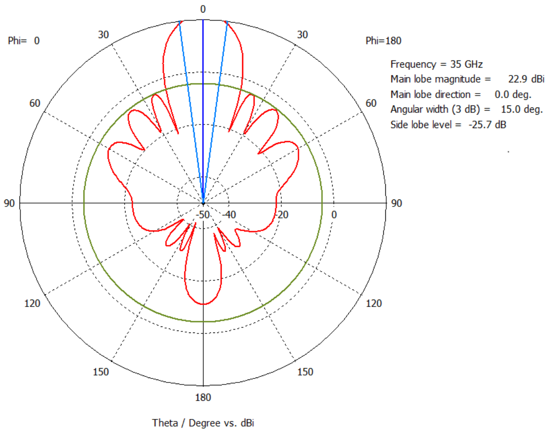

Figure 4.15: Squared 8x8 array radiation pattern H-Plane - vertical polarization

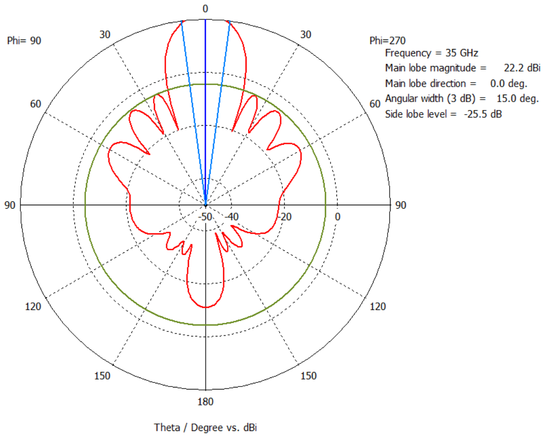

Figure 4.16: Squared 8x8 array radiation pattern E-Plane - horizontal polarization

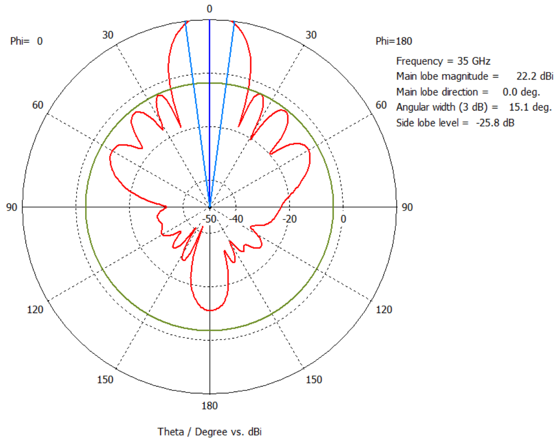

Figure 4.17: Squared 8x8 array radiation pattern H-Plane - horizontal polarization

Along this section, the phase shift for each desired scanning angle are calculated, an analysis of the array maximum steering angle without significantly deforming the main lobe is done, and the simulation results of some steered radiation patterns are shown.

The desired steering angle step is $15°$, corresponding to the Half-power Beam-width angle obtained in section 4.2. Since the distance between array elements was set to $d = 0.5\lambda$, from condition 4.16, to avoid grating lobes the steering angles must be defined in the region $\phi_0 \in [0°, 180°]$. However, as the results of the simulations show, patch arrays have scan angle limitations due to the phenomena described in [37].

Once established a desired steering angle, the phase shift needed to apply to each element is calculated using equation 4.11. The phase shifts for each steering angle are represented in table 4.4, in which $\phi_0 = 90°$ is considered the direction orthogonal to the array plane. The axis considered throughout the design is presented in figures 4.10 and 4.13, where the direction orthogonal to the array plane is defined as the z-axis, and the result figures show cuts in the zx-plane. Considering the array steered angle θ relative to the positive x-axis rotated by $\phi = 180°$, the relation between θ from figure 4.13 and ϕ_0 from figure 4.2 is also represented in table 4.4.

ϕ_0 [°]	90	75	60	45	30
θ [°]	0	15	30	45	60
ψ_0 [rad]	0	0.8131	1.5708	2.2214	2.7207
ψ_0 [°]	0	46.59	90	127.28	155.88

Table 4.4: Consecutive antenna phase shifts for each steering angle

To steer a planar array $N°$ towards a direction in the x-axis, the same phase must be applied to every antenna in each row (y-axis direction), being the phase shift applied to consecutive antennas in each line (x-axis direction). The principal plane of the radiation pattern from the simulation results of this method using the phase shifts for θ from table 4.4 are presented in figures 4.18, 4.19, 4.20 and 4.21.

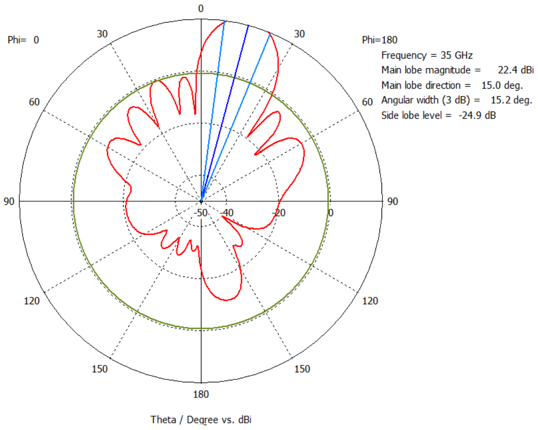

Figure 4.18: Steered radiation pattern principal plane ($\theta = 15°$)

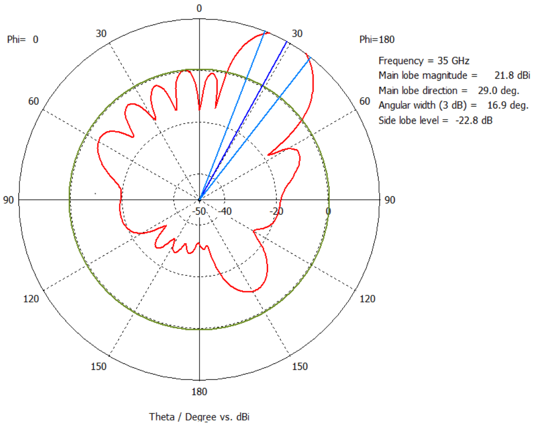

Figure 4.19: Steered radiation pattern principal plane ($\theta = 30°$)

It is possible to verify that the steering was accomplished, however, the Half-power Beam-width, side lobe levels and main lobe magnitude values were more affected as the steering angle increases. These values for the non steered pattern and for the steered patterns are represented in table 4.5

As the steering angle increases it is possible to verify a decrease in the main lobe magnitude and an increse in the half-power beam-width and in the side lobe levels. For $\theta = 45°$, a main lobe deformation is starting

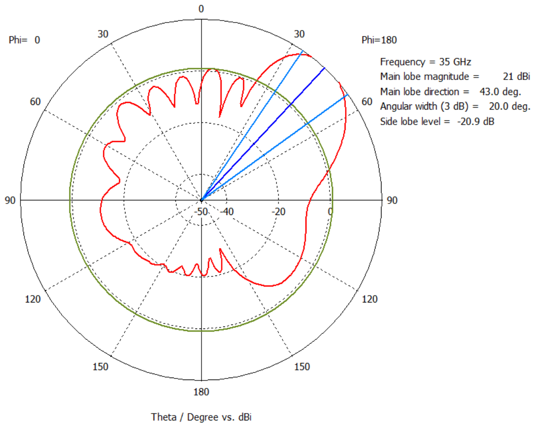

Figure 4.20: Steered radiation pattern principal plane ($\theta = 45°$)

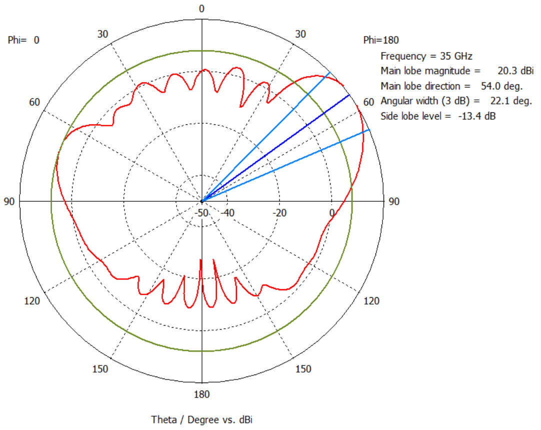

Figure 4.21: Steered radiation pattern principal plane ($\theta = 60°$)

Desired main lobe direction [°]	0	15	30	45	60
Obtained main lobe direction [°]	0	15	29	43	54
Main lobe magnitude [dBi]	22.9	22.4	21.8	21	20.3
Half-power Beam-width [°]	15	15.2	16.9	20	22.1
Side lobe level [dB]	-25.7	-24.9	-22.8	-20.9	-13.4

Table 4.5: Comparison between different steered radiation pattern characteristics

to become noticeable in figure 4.20, and no side lobes exists to the right of the main lobe, which indicates that grating lobes might start to appear for steering angles closer to the array plane. However, the half-power beam-width and side lobe levels for $\theta = 45°$ are still suitable for the purpose of this work. When analysing the results for $\theta = 60°$ in figure 4.21, it is clear that a grating lobe is starting to appear, confirmed by the rise in the side lobe levels to -13.4 dB. This behaviour is not desired, since is conductive to wrong target identifications when using the antenna as a Radar. The limit of the scanning angle for θ is then set to $45°$.

The purpose of this design is to steer the main lobe throughout the space where $z > 0$, (figure 4.13). To do so, a phase shift must also be applied between consecutive antennas in each row, making the phase of each element ψ_{ij} a function of its position within the array (figure 4.10), of the phase shift between elements in each line ψ_{0x} and in each row ψ_{0y}, defined by equation 4.30.

$$\psi_{ij} = i \times \psi_{0x} + j \times \psi_{0y}, \quad i, j = 1, ..., N \tag{4.30}$$

The simulations will only be done for steering angles in the quadrant with $\phi \in [90°, 180°]$ (figure 4.13). For each combination of the phase shifts ψ_{0x} and ψ_{0y} extracted from table 4.4, the principal plane of the radiation pattern is dictated by the orientation in ϕ of the maximum of the main lobe. For each combination of phase shifts, the orientation of the main lobe in ϕ can be predicted according to figure 4.22, using equation 4.31.

$$\phi_{predicted} = \arctan(\frac{\psi_{0y}}{\psi_{0x}}) \tag{4.31}$$

Thus, since the desired steering angles are in the interval $\phi \in [90°, 180°]$, the principal plane orientation of the simulated radiation patterns will be $\phi[°] = 180 - \phi_{predicted}[°]$. The orientation $\phi[°]$ of the principal plane for each combination of phase shifts in table 4.4 (except for $\theta = 60°$) are represented in table 4.6.

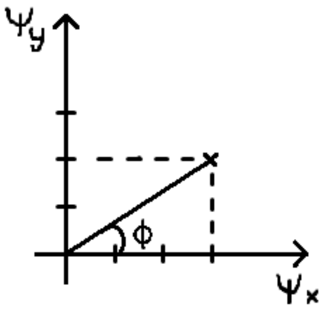

Figure 4.22: Conceptual relation between phase shifts and orientation of the main lobe in ϕ

	$\psi_{0x}[^\circ]$	0.00	46.59	90.00	127.28
$\psi_{0y}[^\circ]$	-	-	-	-	-
0.00	-	180	180	180	180
46.59	-	90	135	153	160
90.00	-	90	117	135	145
127.28	-	90	110	125	135

Table 4.6: Orientation of the principal plane of the radiation pattern for each combination of phase shifts

The results of all simulated radiation patterns are presented in Appendix A. The phase shift for each element in the squared array is calculated using equation 4.30, for all the combinations presented in table 4.6. The simulations were done using the weights from table 4.3. It is possible to verify that the steering throughout the desired quadrant is accomplished, maintaining a minimum side lobe level of -20 dB for every steered radiation pattern. The main lobe HPBW increases as the steering angle in θ increase, which is a known limitation of phased arrays [68]. The phase shift combination $\psi_{0x} = 127^\circ$ and $\psi_{0y} = 127^\circ$ outputs the radiation pattern with characteristics that are affected by steering the most (figure A.15). The obtained HPBW is 27.2°, the main lobe magnitude 19.4 dB and a side lobe level of -20.6 dB.

4.4 Discussion and Future Work

In this chapter, the design of a generic antenna array with steering capabilities was made, and the elements in the array were fed with a Dolph-Chebyshev non-uniform excitation, to achieve a narrow beam with low side lobe level. The Dolph-Chebyshev weights were calculated based on the desired inter-element spacing, side lobe level, and number of elements. The antenna obtained in section 3.3 was used as the single element of the array.

By fixing the inter-element spacing and side lobe level, the number of elements in the array become arbitrary. A theoretical model was used to estimate the radiation pattern half-power beam-width depending on the number of elements. A linear array with 8 elements was simulated in the electromagnetic field simulation software $\mathit{CST\ Studio\ Suite}$, and it was possible to verify a close relationship between the theoretical model and the simulation results.

A planar array with 8x8 elements was then modelled, being the feed coefficients of each element calculated as if the model was a linear array of linear arrays. The array had dual linear polarization (due to the single element having dual-linear polarization), and the results, for both polarizations, were satisfactory for the array to be used in a radar system. The desired side lobe level was maintained, but the half-power beam-width was slightly worse due to mutual coupling between elements. The reflection coefficient of each element were also affected by the mutual coupling, but acceptable magnitudes were still obtained.

Finally, the main lobe of the planar array was steered, being the maximum steering angle identified by a sharp increase on the side lobe level of the radiation pattern. It was concluded that the more the steering angle increases, the more effect on the radiation pattern main lobe magnitude, half-power beam-width and side lobe level is seen. The steering was successfully achieved on the planar array, obtained by using a feed phase shift for each element, computed by considering the model as a linear array of linear arrays.

The array designed is capable of scanning $\pm 45^\circ$ in azimuth, being lower than the necessary azimuth of $\pm 60^\circ$ to be covered, defined in the ELOS for see and avoid [17]. The maximum steering angle can be increased by increasing the number of elements in the array, resulting in an array with a narrower main beam, allowing for a wider scanning angle before the appearance of grating lobes.

As future work, an array with more elements shall be considered, to obtain a better angular resolution. This should be complemented by an increase of the resonant frequency of each single element, as suggested in section 3.4, since it would result in smaller elements, and thus, in a smaller final array physical dimensions. As the scan range in elevation is $(\pm 10^\circ)$ is much smaller than the azimuth range $(\pm 60^\circ)$, a cylindrical array could also be considered, to evaluate the steering angles achievable, and the effect on the width of the main beam. If a good balance were found between the steering angles, and the angular resolution, it would improve the area that the array could scan.

Fabrication and test of a prototype is also an important task to materialize in future work. By doing so, experimental validation of the proposed configurations could be accomplished.

Chapter 5

mm-Wave FMCW Radar Simulation

In this chapter, a mm-wave FMCW radar is studied, along with a radar simulation tool based on $Blender$.

5.1 Theoretical Background

The signal throughout the mm-wave radar block diagram is analysed, along with the study of power propagation in space, and of the digital processing techniques to perform a target detection analysis.

5.1.1 mm-Wave Radar Working Principle

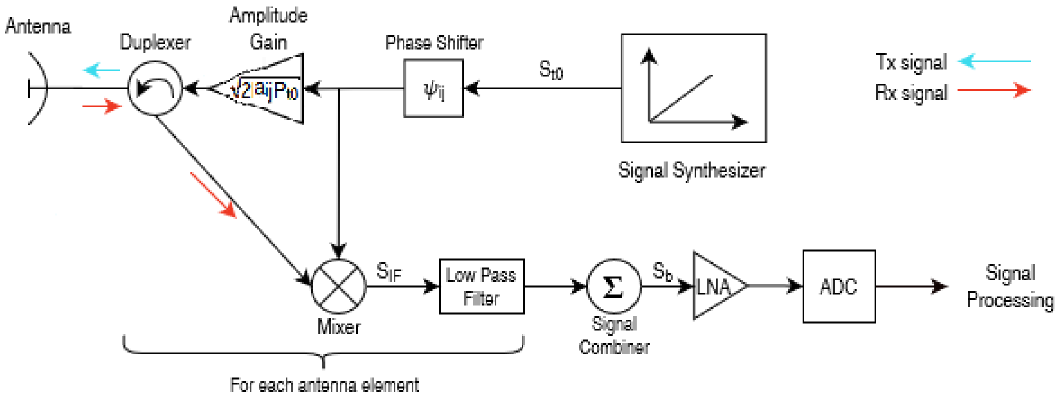

Figure 5.1: mm-Wave FMCW Radar Block Diagram

A complete mm-Wave Radar system includes many RF, analog and digital components, depending on the number of elements of the phased-array. A simplified mm-Wave FMCW Radar block diagram is depicted in figure 5.1. The transmitter part consists of a Signal Synthesizer, that outputs a frequency linear modulated signal, followed by a phase shifter and an amplitude gain amplifier, both specifics for each antenna element and adjusted according to the reasoning of chapter 4. This is followed by a duplexer that isolates and routes the transmitted signals to the antenna and then the antenna propagates the signal into free-space. The receiver part consists of the antenna that receives the reflected signal, that is routed by the duplexer to the mixer, to perform a frequency mixing of the transmitted and received signals, followed by a low pass filter to eliminate the high frequency comoponent of the signal. Note that one of each component is necessary per antenna in the array. Subsequently the following are used: a signal combiner to merge the signals from all the antenna elements; a Low Noise Amplifier (LNA) to adjust the sensitivity of the radar; and an ADC to sample the signal into a post-processing phase. To clarify each process, the remaining of this section expounds each step.

The implementation of signal synthesizers with accurate frequency for mm-Wave FMCW Radar, is a challenge that has recently been tackled by Silicon Germanium (SiGe) technologies. A programmable signal synthesizer based on this technology, with high frequency accuracy output is presented in [47]. The desired output signal from the signal synthesizer, the signal $S_{t0}(t)$, is a linear-frequency modulated chirp, with instantaneous frequency given by equation 5.1, being the signal represented in equation 5.2. In 5.1, f_{min} is the chirp minimum frequency, B_{ch} is the chirp Bandwidth and T_{ch} the chirp duration.

$$f(t) = f_{min} + \frac{B_{ch}}{T_{ch}}t, \qquad t \in [0, T_{ch}] \tag{5.1}$$

$$S_{t0}(t) = e^{j(2\pi \cdot f(t))}, \qquad t \in [0, T_{ch}] \tag{5.2}$$

The signal $S_{t0}(t)$ undergoes a phase shift and an amplitude gain, according to which antenna element that is being fed, and as specified in sections 4.3 and 4.2. The signal $S_{Tij}(t)$ to transmit through each antenna in the array is given by equation 5.3. Note that the power of the signal transmitted by each antenna is $P_{Tij} = a_{ij}P_{t0}$, being the total power transmitted by the array P_t, given by equation 5.4.

$$\begin{aligned} S_{Tij}(t) &= (\sqrt{2a_{ij}P_{t0}})e^{j(2\pi \cdot f(t) - \psi_{ij})} \\ &= (\sqrt{2P_{Tij}})e^{j(2\pi \cdot f(t) - \psi_{ij})} \end{aligned}, \qquad t \in [0, T_{ch}] \tag{5.3}$$

$$P_t = \sum_{i,j} P_{Tij} \tag{5.4}$$

The duplexer routes the signal to the antenna, that transmits it into free space where it propagates. If the transmitted signal hits an obstacle, a part of it is reflected back towards the antenna. The received signal $S_{Rij}(t)$ is a version of the transmitted signal that suffered an attenuation $A_{tt_{ij}}$ in power (related to the quantity of power reflected on the target and to path losses), and a time delay $\phi(R) = \frac{2R}{c}$, that is directly proportional to the target distance R, as depicted in figure 5.2 [39]. The power received by each antenna is $P_{Rij} = P_{Tij}A_{tt_{ij}}$, being the received signal represented by each antenna in equation 5.5, in conjunction with white Gaussian wideband noise $w(t)$ [69].

$$S_{Rij}(t) = \sqrt{2P_{Rij}}e^{j(2\pi f(t) - \psi_{ij} - \phi(R))} + w(t) \tag{5.5}$$

The received signal is routed by the duplexer to the frequency Mixer, and both the transmitted and received signals are mixed. A frequency mixer device receives as input two signals and outputs a new one. The output signal frequency components correspond to the instantaneous sum and difference of the frequency components of the two input signals. The instantaneous difference in frequency of the two signals, for the antenna element with index ij, is called a beat frequency f_{Bij} which is graphically represented in figure 5.2 [70], and is given by

$$f_{Bij} = \frac{2R_{ij}}{c} \cdot \tan(\alpha) = \frac{2R_{ij}B_{ch}}{cT_{ch}} \tag{5.6}$$

Despite being very close, each antenna element is spaced from one another, and thus, the reflected signal arrives at each antenna element at different time instances, as depicted in figure 5.3. To combine the received signals, the mm-Wave radar receiver should compensate this delay for each antenna element individually, and

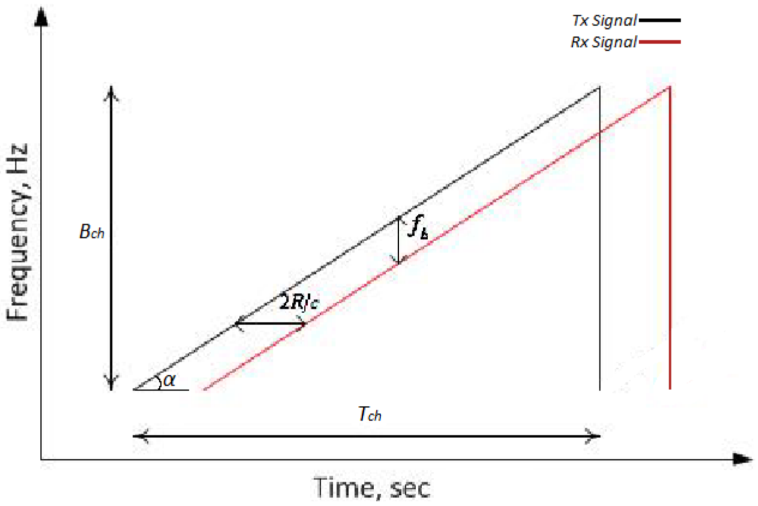

Figure 5.2: Frequency vs time - Transmitted vs Received Signals (extracted from [70])

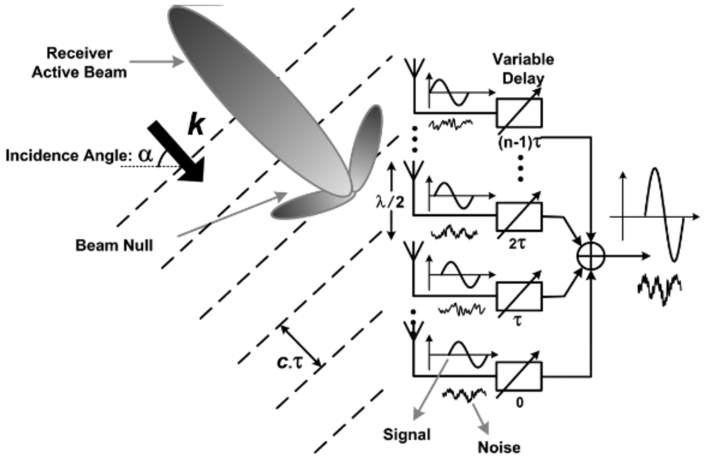

Figure 5.3: Delay of receiving signals in multiple antenna elements (extracted from [71])

according to the incidence angle of the receiver [71] [39]. The compensation is done accordingly to the position of each element in the array.

Considering that the mentioned delay is compensated, the beat frequency can be considered the same for each antenna element, i.e,

$$f_{Bij} = f_b = \frac{2RB_{ch}}{cT_{ch}} \tag{5.7}$$

A frequency mixer that receives as inputs the signals from equations 5.3 and 5.5, outputs a signal $S_{IFij}(t)$ given by equation 5.8. Note that e^{-jf_bt} is the low frequency component that contains relevant information, and $e^{j(4\pi \cdot f(t)-f_bt)}$ is the irrelevant high frequency component of S_{IF}.

$$S_{IFij}(t) = \sqrt{2P_{Rij}}e^{-j2\pi f_bt}e^{j(2\pi(2\pi f(t)-f_bt)} + w(t) \tag{5.8}$$

The high frequency component is then eliminated by the low pass filter. The signals from each antenna are combined, as depicted in figure 5.3, to create the Beat signal. This signal carries information about target detection and distance. The beat signal is represented in equation 5.9, being the sum of the received signal for all antennas. Note that the sum of the power received by each antenna is the total power received by the whole array, i.e, $\sum_{i,j} P_{Rij} = P_r$.

$$S_b(t) = \sqrt{2\sum_{i,j} P_{Rij}} e^{-j2\pi f_b t} + w(t) = \sqrt{2P_r} e^{-j2\pi f_b t} + w(t) \tag{5.9}$$

The LNA is usually tuned to adjust the desired sensitivity of the Radar, since the detection of target in the post-processing phase is decided based on the amplitude of the sampled signal. The signal to be sampled by the ADC is given by equation 5.10.

$$S_{ADC}(t) = \sqrt{2P_r} G_{LNA} e^{-j2\pi f_b t} + w(t) \tag{5.10}$$

The signal is sampled at N points acquired with a sampling interval T_s, being the digital data given by

$$S(n) = S_{ADC}(t)\delta(t - nT_s), \quad n = 0, 1, ..., N-1 \tag{5.11}$$

The delta function $\delta(t)$ is defined by

$$\delta(t - t_0) = \begin{cases} 1, & t = t_0 \\ 0, & t \neq t_0 \end{cases} \tag{5.12}$$

Due to the high rate of signal acquisition, the post-processing in phased arrays mm-Wave Radars is usually done by sampling the signals onto an FPGA, and subsequently sending them through a network to a processing device (such as a computer), to avoid having a lack of processing power in the FPGA [50]. Note that power signals are considered throughout this chapter.

5.1.2 Power propagation in space

The received power P_r, in equation 5.9, can be calculated by analysing the power propagation in space. The power density P_D of an antenna, radiating P_{t0} power , to a point located at distance R and angular direction (θ, ϕ), is defined as the amount of power transferred per unit of area to the surface area of a sphere at that distance [72]. For an antenna with gain G the power density is given by:

$$P_D(\theta, \phi, R) = \frac{P_t G(\theta, \phi)}{4\pi R^2} \tag{5.13}$$

If a target is found at that location, the reflected power P_{rt}, given by equation 5.14, is the density of the power received, affected by the radar cross section of the target in the considered direction σ, and also affected the reflection coefficient of the object Γ.

$$P_{rt}(\sigma, \Gamma) = P_D(\theta, \phi, R) \cdot \sigma \cdot \Gamma \tag{5.14}$$

The reflected signal is not affected by any gain, thus, the power density of the signal reflected by the target P_{Dt}, received back at the antenna, is given by:

$$P_{Dt}(R) = \frac{P_{rt}(\sigma, \Gamma)}{4\pi R^2} = \frac{P_t G(\theta, \phi)\sigma\Gamma}{(4\pi)^2 R^4} \tag{5.15}$$

The power captured by the receiving array is given by equation 5.16, being proportional to the effective area of the antenna $A_e = \frac{\lambda^2 G(\theta,\phi)}{4\pi}$ [72]. Note that the final equation is similar to the Radar equation [73], also considering losses due to the reflection coefficient of the target. Note that perfect polarization matching has been assumed to calculate the received power.

$$P_r = P_{Dt} \cdot A_e = \frac{P_t G(\theta, \phi)^2 \lambda^2 \sigma\Gamma}{(4\pi)^3 R^4} \tag{5.16}$$

5.1.3 Radar Detection and Distance Measurement

The post processing phase starts with the sampling of the signal in equation 5.10, as represented in equation 5.11. According to the Nyquist Theorem, the maximum frequency that can be accurately represented by a sampled signal is half of the sampling frequency f_s. Thus, the sampling frequency f_s of the ADC must be set, taking into consideration the maximum frequency that would be detected, according to the reasoning of section 5.1.1. The Nyquist frequency is then given by equation 5.17.

$$f_N = \frac{f_s}{2} \tag{5.17}$$

Note that, the sampling frequency is related to the sampling interval T_s of each sample, as given by

$$T_s = \frac{1}{f_s} \tag{5.18}$$

The digital signal must then be analysed to determine its amplitude and frequency. To do so, a spectral analysis technique is used in order to determine the frequencies that are present in a signal, as well as the energy carried at the different frequencies found. The Discrete Fourier Transform (DFT) is a common spectral analysis technique used in many different fields, such as modern Radar applications [74]. It transforms a signal sampled at N points in the time domain, resulting in a new N point signal in the frequency domain, containing the amplitudes of the sine and cossine components that the original signal can be decomposed into [75]. The most used algorithm to efficiently compute the DFT is the Fast Fourier Transform (FFT), that reduces computational complexity from $O(N^2)$ to $O(NlogN)$ [76].

The N point FFT $X(k)$ of a discrete time sequence $S(n)$ with length N, is given by

$$\begin{aligned} X(k) &= \sum_{n=0}^{N-1} S(n) e^{-j\frac{2\pi kn}{N}} \\ &= \sum_{n=0}^{N-1} S(n)\cos(\frac{2\pi kn}{N}) - j\sum_{n=0}^{N-1} S(n)\sin(\frac{2\pi kn}{N}) \end{aligned} \quad , \quad k = 0, 1, ..., N-1 \tag{5.19}$$

with k being the frequency domain independent variable. To relate each value of $X(k)$ to a frequency f, equation 5.20 is used. The FFT transformation of an N point time domain signal to an N point frequency domain signal, is depicted in figure 5.4. Note that the amplitude of the cossine waves are stored in the real part of the FFT $Re\{X(k)\}$, and the amplitude of the sine waves in the imaginary part $Im\{X(k)\}$.

$$f = k\frac{f_s}{N} \tag{5.20}$$

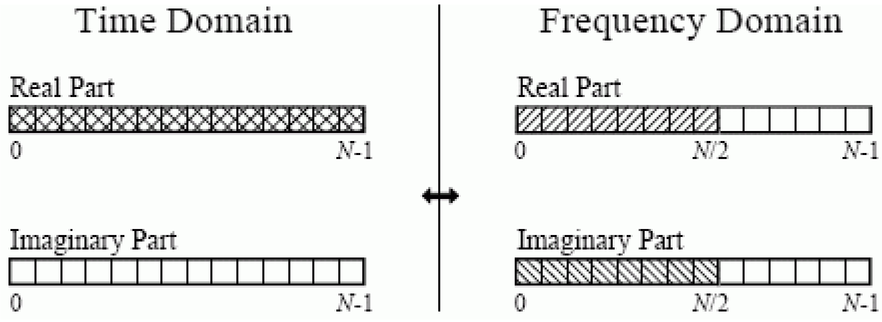

Figure 5.4: Complex DFT signal transformation (extracted from [76])

The results of $X(k)$, $k \in [0, ..., N/2]$ contain the positive frequency values, and the results of $X(k)$, $k \in [N/2+1, ..., N-1]$ contain the negative frequency values. The DFT algorithms have a periodic frequency spectrum, and by that, a phenomena happens, in which the positive frequency spectrum is mirrored to the negative frequency spectrum. This phenomena is explained in detail in [77]. One easy way to deal with this effect is to only consider the positive frequency values of the FFT, and perform the analysis only on the positive frequency spectrum, i.e, with $n \in [0, N/2]$ [78] [76].

The amplitude of the sampled signal can be retrieved using the absolute value of the FFT at its maximum, according to equation 5.21, being $\max(|X(k)|) = \max\left(\sqrt{Re\{X(k)\}^2 + Im\{X(k)\}^2}\right)$.

$$A_{fft} = \frac{2 \cdot \max(|X(k)|)}{N} \tag{5.21}$$

In case of presence of a target, the signal to sample (equation 5.10) is affected by white gaussian noise with power spectral density N_0, that is a random variable with normal distribution, with zero mean and variance given by equation 5.22. The power spectral density is given by equation 5.23, being k_{boltz} the Boltzmann constant and T_{noise} the noise temperature of the receiver.

$$\sigma_N^2 = \frac{N_0}{T_{ch}} \tag{5.22}$$

$$N_0 = k_{boltz} T_{noise} B_{ch} \tag{5.23}$$

The amplitude A_{fft} is then a random variable with Rice distribution, which is a distribution model usually used to model transmissions between two points in view of each other [79] [80]. The probability density function of a Rice distribution is given by equation 5.24, with $S^2 = A_{fft}^2$ being the non-centrality parameter of the distribution, and $I_0(\cdot)$ the zero-order modified Bessel function of the first kind.

$$p_{Z_{A_{fft}}}(z|S > 0) = \frac{z}{\sigma_N^2}\exp(-\frac{z^2 - S^2}{2\sigma_N^2}) I_0(\frac{zS}{\sigma_N^2}), \quad z \geq 0 \tag{5.24}$$

In case of absence of target, $S^2 = S = 0$, and the amplitude A_{fft} becomes a random variable with Rayleigh distribution, with a probability density function given by: [80]

$$p_{Z_{A_{fft}}}(z|S = 0) = \frac{z}{\sigma_N^2}\exp(-\frac{z^2}{2\sigma_N^2}), \quad z \geq 0 \tag{5.25}$$

The target detection operation asserts if the amplitude of the sampled signal is under a threshold level V_{th}, being the following criteria is used:

$$\begin{cases} A_{fft} < V_{th}, & \text{target absent} \\ A_{fft} > V_{th}, & \text{target present} \end{cases} \tag{5.26}$$

The probability of correct target detection P_d, is the probability of detecting a target in case it is actually present, given by equation 5.27. Note that $Q(\cdot, \cdot)$ is the Marcum's Q-function. [80]

$$\begin{aligned} P_d &= \text{prob}\{P_{fft} > V_{th} | S > 0\}, \\ &= \int_{V_{th}}^{\infty} p_z(z|S > 0) dz \\ &= Q\left(\frac{P_{fft}}{\sigma_N}, \frac{V_{th}}{\sigma_N}\right) = Q\left(P_{fft}\sqrt{\frac{T_{ch}}{N_0}}, V_{th}\sqrt{\frac{T_{ch}}{N_0}}\right) \end{aligned} \tag{5.27}$$

The probability of false alarm P_{fa}, is the probability of detecting a target when no target is present, given by

$$\begin{aligned} P_{fa} &= \text{prob}\{P_{fft} > V_{th} | S = 0\}, \\ &= \int_{V_{th}}^{\infty} p_z(z|S = 0) dz \\ &= \exp(-\frac{V_{th}}{2\sigma_N^2}) \end{aligned} \tag{5.28}$$

Since P_d and P_{fa} are affected by V_{th}, usually the value of V_{th} is chosen using the Neyman-Pearson criteria, given by equation 5.29 [80].

$$V_{th} = \sqrt{-2\sigma_N^2 \ln(P_{fa})} \tag{5.29}$$

The target distance is calculated by determining the frequency that corresponds to index k of the maximum of $|X(k)|$, using equation 5.20, that combined with equation 5.7, allow to compute the target distance.

5.2 Simulation Concepts

The Radar simulation is performed based on rendered images obtained from a 3D environment created in *Blender*, and on the radiation patterns obtained in the results of chapter 4 (mostly depicted in annex A). The processing of these files was made in a $Python$ environment.

The 3D environment was setup in *Blender* by inserting objects into a scene. A camera is a special object that specifies to the ray tracer the part of the scene to be rendered into an image, having several properties that can be tweaked to achieve the desired characteristics for the output image. In *Blender*, the camera lens defines how the 3D environment is mapped to the 2D image, being a key property to control the image output projection. A detailed explaination of 3D to 2D projections can be found in [59] and [81].

To output the rendered image directly to a file, compositing was used in *Blender* to export the "Render Layer", selecting the Z-pass and Normal-pass data to be output along with the image, into a $.exr$ format, which allows to have different data layers for every pixel in an image [56]. The Z-pass data contains the absolute distance in meters from the camera position to any visible surface within its field of view, and the Normal-pass contains the surface normal vector weights, relative to the main referential of the scene, both information being obtained for each pixel during the rendering done by the ray tracer. For each render, the *Blender* camera position and orientation were also exported.

The radiation patterns data were also exported from $CST\ Studio\ Suite$, with an angle step of $1°$, covering the angles $\theta \in [0°, 90°]$ and $\phi \in [0°, 360°[$. The output files were organized in the form of (θ, ϕ, $Gain$), which is a equirectangular projection representation of the radiation pattern gain data. An equirectangular projection is a type of stereographic projection in which the longitude of each point is mapped directly to the horizontal coordinate, and the latitude to the vertical coordinate.

The rendered images were output with panoramic fisheye equidistant, also known as tiny planet, projection. This is a type of stereographic projection, that maps the spherical view of the environment seen by the camera to a flat image, having a linear relation between its variables (r_{fep},θ_{fep}) and the latitude and longitude, respectively, of each point seen by the camera, when analysed with a polar coordinate system at its center [82]. Points at equal distance r_{fep} to the centre of the referencial all have the same latitude, and points at the same θ_{fep} all have the same longitude. The projection field of view was set to $180°$, covering half of the whole spherical image seen by the camera, and the image pixel resolution was set to $N_{pix} \times N_{pix}$ pixels. Assuming that the antenna array is located at the camera position facing towards the environment seen in the image, it is possible, by using equations 5.30 and 5.31, to convert each pixel position (n_{px}, n_{py}) of the image with fisheye equidistant projection, to an angular direction (θ_{pos}, ϕ_{pos}) with $\theta \in [0°, 90°]$ and $\phi \in [0°, 360°[$, corresponding to the direction of that point in space relative to the antenna referential (refer to image 4.13).

$$\begin{aligned} r_{fep} &= \sqrt{((\frac{N_{pix}}{2} - n_{px})^2 + (\frac{N_{pix}}{2} - n_{py})^2)} \\ \theta_{fep} &= \arctan\left(\frac{\frac{N_{pix}}{2} - n_{py}}{\frac{N_{pix}}{2} - n_{px}}\right) \end{aligned} \quad , \quad n_{px}, n_{py} \in [0, N_{pix}] \tag{5.30}$$

$$\begin{aligned}\theta_{pos} &= r_{fep} * \frac{90}{N_{pix}/2}, \quad n_{px}, n_{py} \in [0, N_{pix}] \\ \phi_{pos} &= \theta_{fep}\end{aligned} \tag{5.31}$$

An easy way to correlate the rendered images to the radiation patterns, is to map the exported data from each radiation pattern to an image with fisheye equidistant projection, and process the rendered image pixel by pixel, using each radiation pattern to simulate the scan of the antenna to each desired direction. Thus, an image with the same pixel resolution $N_{pix} \times N_{pix}$ shall be created for each radiation pattern. The images are filled by calculating the orientation (θ_{pos}, ϕ_{pos}) of each pixel using equations 5.30 and 5.31, and assigning the value of the gain in that direction of each radiation pattern untill all pixels are filled. Note that only pixels with $r_{fep} < N_{pix}/2$ shall be mapped, since the remaining pixels do not contain valuable data in a fisheye equidistant projection. The obtained radiation patterns equirectangular projections and the fisheye equidistant projections are depicted in annex A. Note that the radiation patterns obtained in chapter 4 only cover the 1st quadrant of the fisheye equidistant projection referential, and thus, to perform the simulation, the radiation patterns were mirrored to the remaining quadrants, using symmetry relative to the referential at the centre of the images.

The calculated pixel point latitude and longitude $(\theta_{pos}, \phi_{pos})$, allow to calculate the unitary vector $\overrightarrow{r_{pos}^{ant}}$ in the pixel direction, relative to the antenna referential, using equation 5.32.

$$\overrightarrow{r_{pos}^{ant}} = \begin{bmatrix} \cos(\theta_{pos}) \cdot \cos(\phi_{pos}) \\ \cos(\theta_{pos}) \cdot \sin(\phi_{pos}) \\ \sin(\theta_{pos}) \end{bmatrix} \tag{5.32}$$

The camera axis in *Blender* is oriented such that every pixel in the image correspond to a point with a negative z-coordinate. Thus, to convert the unitary vector from the antenna array referential to the camera referential, a $180°$ Euler rotation in the Y-axis is done, being the unitary vector in the camera referential $\overrightarrow{r_{pos}^{cam}}$ given by equation 5.34. Throughout this work, the Euler rotations are performed in the XYZ order, and thus, the used rotation matrix, R_{XYZ}, is represented in equation 5.33, with R_X, R_Y and R_Z being the Euler rotation matrices over each axis.

$$R_{XYZ}(\alpha_x, \alpha_y, \alpha_z) = R_Z(\alpha_z) \cdot R_Y(\alpha_y) \cdot R_X(\alpha_x) \tag{5.33}$$

$$R_X(\alpha_x) = \begin{bmatrix} 1 & 0 & 0 \\ 0 & \cos(\alpha_x) & -\sin(\alpha_x) \\ 0 & \sin(\alpha_x) & \cos(\alpha_x) \end{bmatrix} \quad R_Y(\alpha_y) = \begin{bmatrix} \cos(\alpha_y) & 0 & \sin(\alpha_y) \\ 0 & 1 & 0 \\ -\sin(\alpha_y) & 0 & \cos(\alpha_y) \end{bmatrix}$$

$$R_Z(\alpha_z) = \begin{bmatrix} \cos(\alpha_z) & -\sin(\alpha_z) & 0 \\ \sin(\alpha_z) & \cos(\alpha_z) & 0 \\ 0 & 0 & 1 \end{bmatrix}$$

$$\overrightarrow{r_{pos}^{cam}} = R_{XYZ}(0, 180°, 0) \cdot \overrightarrow{r_{pos}^{ant}} \tag{5.34}$$

The vector $\overrightarrow{r_{pos}^{cam}}$ can then be represented relative to the *Blender* scene referential, by considering the orientation of the camera exported along with the render. The unitary vector in the scene referential, $\overrightarrow{r_{pos}^{scene}}$, is then given by equation 5.35, being α_{camX}, α_{camY} and α_{camZ} the Euler angle rotations of the camera according to the scene referential.

$$\overrightarrow{r_{pos}^{scene}} = R_{XYZ}(\alpha_{camX}, \alpha_{camY}, \alpha_{camZ}) \cdot \overrightarrow{r_{pos}^{cam}} \tag{5.35}$$

The Z-pass data can be used along with each unitary vector to obtain the point position relative to each referential. Note that, to calculate the point position in the scene referential, the camera location $P_{cam} = (P_{camX}, P_{camY}, P_{camZ})$, exported along with the render, must also be taken into consideration. The surface point represented in the pixel (n_{px}, n_{py}) can be positioned in the coordinates of each referential, being the P_{pos}^{ant}, P_{pos}^{cam} and P_{pos}^{scene}, the coordinates of the location of that point in the antenna referential, in the camera referential and in the scene referential, respectively. This is easily computed using equations 5.36.

$$\begin{aligned} P_{pos}^{ant} &= Z_{pass}(n_{px}, n_{py}) \cdot \overrightarrow{r_{pos}^{ant}} \\ P_{pos}^{cam} &= Z_{pass}(n_{px}, n_{py}) \cdot \overrightarrow{r_{pos}^{cam}} \\ P_{pos}^{scene} &= \begin{bmatrix} P_{camX} \\ P_{camY} \\ P_{camZ} \end{bmatrix} + Z_{pass}(n_{px}, n_{py}) \cdot \overrightarrow{r_{pos}^{scene}} \end{aligned} \tag{5.36}$$

5.3 Simulation Method

The goal of the correlation between the rendered image and the radiation patterns, is to obtain the digital signal that would be sampled by the ADC of the radar system, defined in equation 5.11, to perform the processing described in section 5.1.3. The simulated signal, $S_{sim}(n)$ with N samples, was computed, for each radiation pattern, using equation 5.37, with $P_{r;px,py}$ and $f_{b;px,py}$ being the contribution of each pixel to the received power and to the beat frequency, respectively.

$$S_{sim}(n) = G_{LNA}\sqrt{2\sum_{px,py} P_{r;px,py}} e^{-j2\pi f_{b;px,py} \cdot nT_s}, \qquad n = 0, 1, ..., N-1 \tag{5.37}$$

The number of samples to compute, N, in order to cover the whole signal, shall be related to the chirp signal duration and to the sampling frequency, as represented in equation 5.38. The chirp duration shall be set taking into consideration the maximum distance willing to identify, being calculated using equation 5.39 (based on figure 5.2). The sampling frequency should be set, according to the Nyquist theorem (equation 5.17), being twice as much the maximum frequency desired to identify in the signal (equation 5.7). Since the chirp duration is set according to the maximum distance to identify, the maximum frequency to identify is the bandwidth of the original signal (figure 5.2). By using the chirp duration defined in equation 5.39, the sampling frequency obtained using equation 5.40 is precisely the double of the bandwidth of the original signal. The sampling interval T_s is given by equation 5.18.

$$N = T_{ch} \cdot f_s \tag{5.38}$$

$$T_{ch} = \frac{2R_{max}}{c} \tag{5.39}$$

$$f_s = 2 \times \frac{2R_{max}B_{ch}}{cT_{ch}} = 2B_{ch} \tag{5.40}$$

The reflected power per pixel is computed using equation 5.41 (based on equation 5.16). For simplicity, the reflection coefficient Γ is considered as unity. Note that the gain of the array in each direction, $G(\theta, \phi)$, is converted to the gain of the array for each pixel $G_{px,py}$, using equations 5.30 and 5.31.

$$P_{r;px,py} = \frac{P_t \lambda^2 G^2_{px,py} \sigma_{px,py}}{(4\pi)^3 R^4_{px,py}} \tag{5.41}$$

The radar cross section $\sigma_{px,py}$ is calculated by assuming that the surface area covered by each pixel is a flat squared plate with sidelength $l_{px,py}$, that is at a distance $R_{px,py}$, and orientated according to its normal $\overrightarrow{r_{px,py}}$. The radar cross section of a squared plate is also highly influenced by the angle of incidence θ_{inc} of the propagated wave relative to the surface normal, being given by equation 5.42. [83]

$$\sigma_{px,py} = \frac{4\pi l^4_{px,py}}{\lambda^2} \left(\frac{\sin[k_0 l_{px,py} \cdot \sin(\theta_{inc})]}{k_0 l_{px,py} \cdot \sin(\theta_{inc})} \right)^2 \tag{5.42}$$

Since stereographic projections were used, with a field of view of $180°$ and a pixel size of $N_{pix} \times N_{pix}$, the angle/pixel resolution is the same for the latitude and longitude, $\theta_{res} = \frac{180°}{N_{pix}}$. Thus, the sidelength $l_{px,py}$ relative to each pixel can be calculated according to figure 5.5, using equation 5.43.

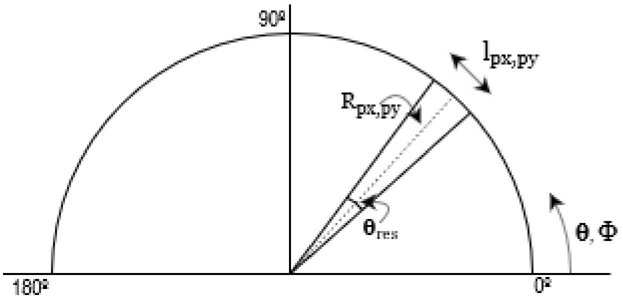

Figure 5.5: Surface sidelength $l_{px,py}$ of each pixel on a circle with radius $R_{px,py}$

$$l_{px,py} = 2R_{px,py} \sin\left(\frac{\theta_{res}}{2}\right) \tag{5.43}$$

The angle of incidence θ_{inc} is calculated from the internal product between the unitary vector in the pixel direction, calculated using equation 5.35, and the surface normal obtained from the Normal-pass exported from *Blender*. The surface normal, $\overrightarrow{r^{scene}_{surf}}$, is a unitary vector relative to the scene referential. The angle of incidence between the two vectors can then be calculated with equation 5.44, obtained as depicted in figure 5.6. Note that $|\overrightarrow{a} \cdot \overrightarrow{b}| = a_x b_x + a_y b_y + a_z b_z$.

$$\theta_{inc} = 180 - \arccos\left(\left| \overrightarrow{r^{scene}_{pos}} \cdot \overrightarrow{r^{scene}_{surf}} \right| \right) \tag{5.44}$$

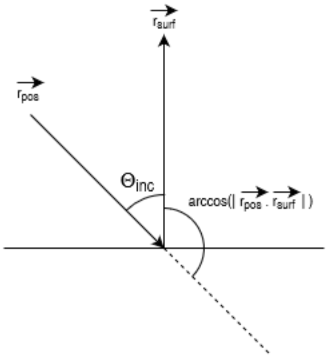

Figure 5.6: Angle of incidence on a surface

The contribution of each pixel to the beat frequency is calculated using equation 5.45 (based on equation 5.7).

$$f_{b;px,py} = \frac{2R_{px,py}B_{ch}}{cT_{ch}} \tag{5.45}$$

Furthermore, the threshold voltage level V_{th}, related to the sensibility of the radar, is calculated using equation 5.29. The minimum power of the received signal, in order to detect a target, is then given by equation 5.46. The transmitted power, P_t, shall be set according to the maximum target distance to identify, to the target minimum radar cross section, to the threshold level to claim a detection, and to the antenna characteristics, using equation 5.47 that was obtained from equation 5.16.

$$P_{r,min} = \frac{1}{2}V_{th}^2 \tag{5.46}$$

$$P_t = \frac{P_{r,min}(4\pi)^3 R_{max}^4}{max(G_{px,py})^2 \lambda^2 \sigma} \tag{5.47}$$

Note that the chirp minimum frequency and bandwidth were set according to the results obtained in section 4.2. According to the reflection coefficients presented in figures 4.11 and 4.12, the bandwidth of the chirp could be set up to 1.5GHz, with a minimum frequency of 34.2GHz.

Once the simulated radar signals are computed, the FFT is applied to each signal, and the amplitude of the sampled signals are computed according to equation 5.21. To assert if a target is detected, the criteria in equation 5.26 is used, and if a target is detected, equation 5.48 is used to calculate its distance. Note that $f_{max(|X(k)|}$ is the frequency corresponding to the index k of the maximum of the FFT, computed with equation 5.20.

$$R_{sim} = \frac{f_{max(|X(k)|}cT_{ch}}{2B_{ch}} \tag{5.48}$$

To perform the radar simulation, the simulation environment was created in $Python$ as outlined in algorithm 1, followed by the computation of the simulated radar signals, as outlined in algorithm 2, and by a target detection analysis, as outlined in algorithm 3. Note that the algorithms are written in pseudo-code.

Algorithm 1 Import the image and radiation patterns to create the simulation environment

```
Require: A .exr image file with distance and surface normal data per pixel, the camera position at
    render time, and a .txt radiation pattern data for each radiation pattern to import.
Import the .exr file and separate each layer of data.
Import the camera position.
Calculate the pixel resolution of the image.
Import each radiation pattern.
for Each imported radiation pattern do
    Map the radiation pattern data to the used image projection.
end for
Using symmetry, create the radiation patterns for the non-simulated quadrants.
```

Algorithm 2 Compute the radar signals obtained by scanning an image with a set of radiation patterns

```
Require: The distance and surface normal of each pixel in the image, and the radiation patterns mapped according to the image mapping.
Compute the chirp duration $T_{ch}$, sampling frequency $f_s$ and number of samples $N$.
Compute the radar minimum power to detect a target $P_{r,min}$, and the transmitted power $P_t$.
for Each pixel in the image do
    Compute the pixel radar cross section.
    Compute the pixel contribution to the beat frequency.
end for
for Each radiation pattern to be used do
    for Each sample of the chirp do
        Compute the received power per pixel.
        Compute the radar signal at sample $n \in [0, N-1]$.
    end for
end for
```

Algorithm 3 Perform a target detection analysis for a set of radar signals

```
Require: A set of radar signals with $N$ samples each.
for Each radar signal do
    Compute the FFT.
    Compute the amplitude of the sampled signal at the maximum of the FFT.
    if The computed amplitude is higher than the threshold level to detect a target then
        Assert target detected.
        Compute the target distance, from the frequency corresponding to the maximum of the FFT.
    else
        Assert target undetected.
    end if
end for
```

5.4 Simulation Results

For the results that follow, a chirp with minimum frequency of 34.5 GHz, and 1 GHz of bandwidth was considered. The maximum distance to detect, R_{max}, was set to 200 m, to be considered in a rendered image with 500×500 pixel resolution. The false alarm probability was set to $P_{fa} = 10^{-2}$, the noise temperature T_{noise} to 290 K and the gain of the low noise amplifier was set to unity, considering the worst case scenario. With this assumptions, the values in table 5.1 were computed. Note that to compute the transmitted power, the maximum of the array gain in the orthogonal direction to the array plane is used.

Two environments were made in $Blender$, being the environment A depicted in figure 5.7 and the environment B in figure 5.8. Environment A consists of 3 cubes, placed at approximately the defined distance

N_0 [W]	4.002×10^{-12}
T_{ch} [s]	1.333×10^{-6}
f_s [Hz]	2×10^{9}
T_s [s]	5×10^{-10}
N	2668
λ [m]	$8.696\ \times10^{-3}$
k_0 [rad/m]	722.566
V_{th} [V]	$5.257\ \times10^{-3}$
$P_{r,min}$ [W]	$1.382\ \times10^{-5}$
P_t [W]	7.261

Table 5.1: Radar simulation specifications

R_{max} from the camera position, and environment B consists on a mesh of objects, placed close to each other and close to the camera position. Note that the cubes all have the same size. The images obtained from each environment are depicted in figures 5.9 and 5.10. Note that figure 5.9 was shown without referential, and with a different background, to allow the visualization of the targets. Both images are taken with the camera at the same position and with the same orientation, being $(P_{camX}, P_{camY}, P_{camZ}) = (2, 0, 0)$m and $(\alpha_{camX}, \alpha_{camY}, \alpha_{camZ}) = (90, 0, 90)°$.

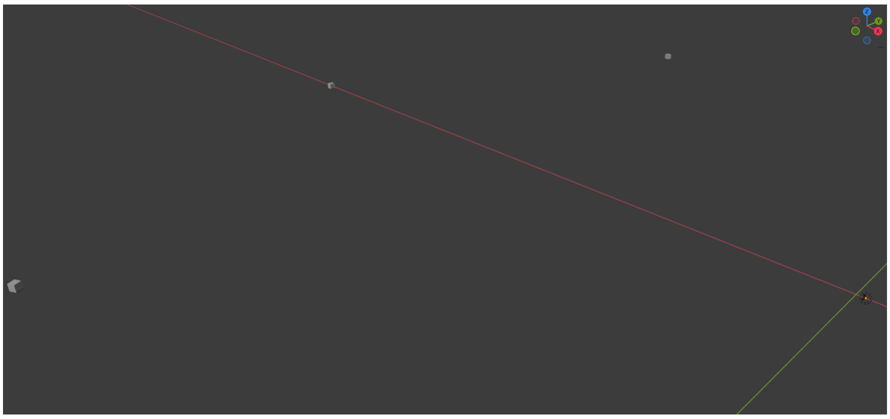

Figure 5.7: Radar Simulation Scene for Environment A

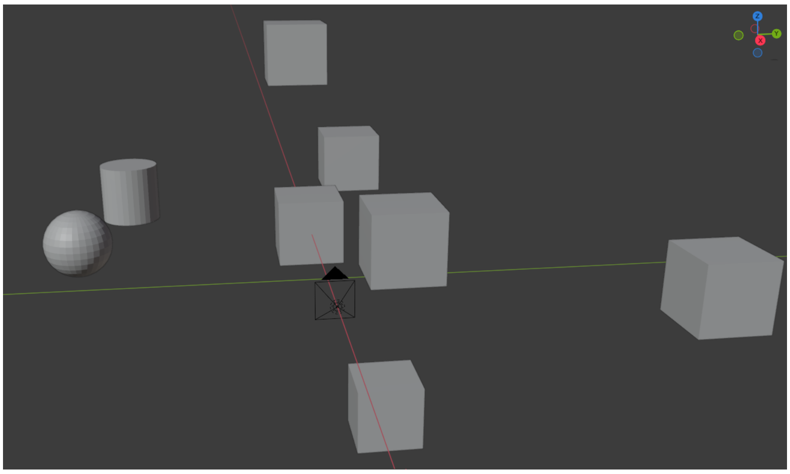

Figure 5.8: Radar Simulation Scene for Environment B

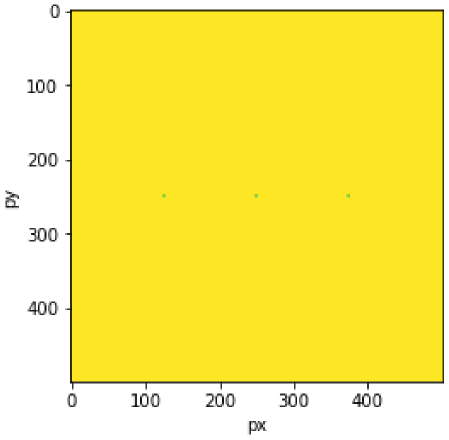

Figure 5.9: Image obtained from environment A

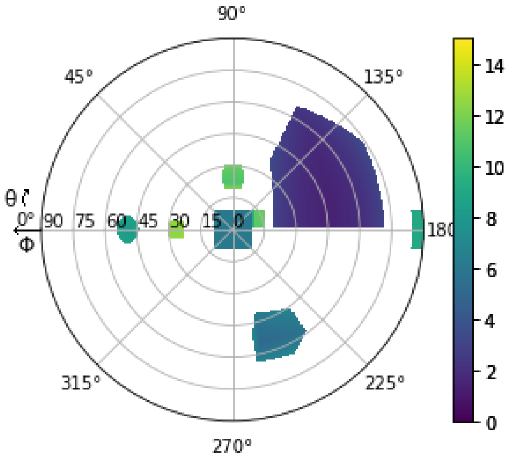

Figure 5.10: Image obtained from environment B

As already stated, the radiation patterns depicted in annex A were mirrored to the remaining quadrants. The radiation patterns were overlapped into an image, depicted in figure 5.11. Note that the simulation is done considering each radiation pattern individually, the purpose of figure 5.11 is just to visualise the whole area of the image scanned by the antenna.

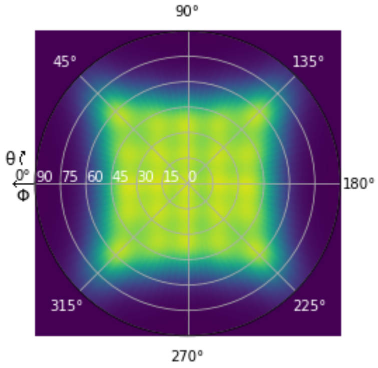

Figure 5.11: Area covered by the antenna array

The simulation results from all radiation patterns were mapped into a single image, covering the same field of view as in figures 5.9 and 5.10, but with a smaller pixel density. The angle step between each radiation pattern was set to 15° in section 4.3, being the image result of the simulation constructed with a pixel density of $N_{pix,sim} \times N_{pix,sim}$, with $N_{pix,sim} = \frac{180}{15} + 1 = 13$, being the number of possible scanned angular directions. Since not every possible direction is scanned by the antenna, only the central 7×7 pixels are filled with data, analogue to the covered area conceptually depicted in figure 5.11. Each pixel stores the result of the distance in case of detection, according to the reasoning detailed in section 5.3.

5.4.1 Results for Environment A

The purpose of environment A was to verify that a target at approximately the maximum distance was detected, by obtaining a signal amplitude close to the detection voltage threshold. The image corresponding to the result of the simulation is depicted in figure 5.12. Only the cube positioned orthogonally to the camera was detected, obtained as result of the scan using the radiation pattern with mainbeam oriented orthogonally to the camera plane. The results of the positive frequency spectrum, representing the absolute value of the FFT *versus* frequency, for the scan that detected a target, are plotted in figure 5.13, for the scans using the radiation patterns that could detect the left and right cubes in figures 5.14 and 5.15, respectively, and for one of the scans without any target found in figure 5.16.

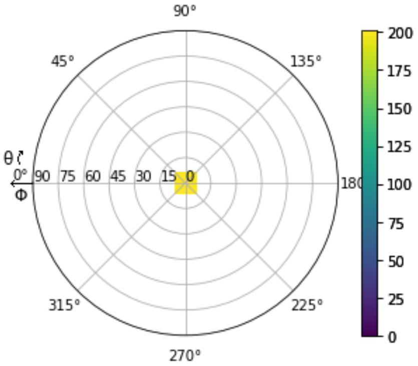

Figure 5.12: Simulation result image for Environment A

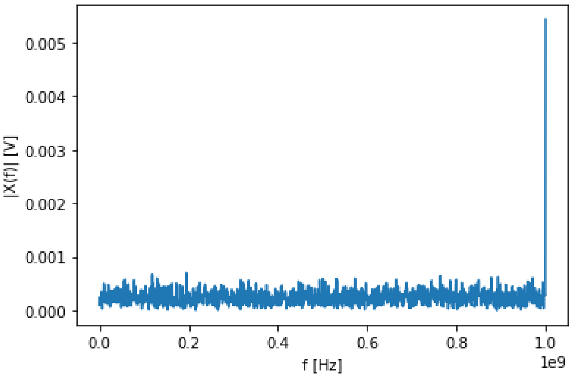

Figure 5.13: Frequency spectrum of the scan with radiation pattern pointing to the central cube

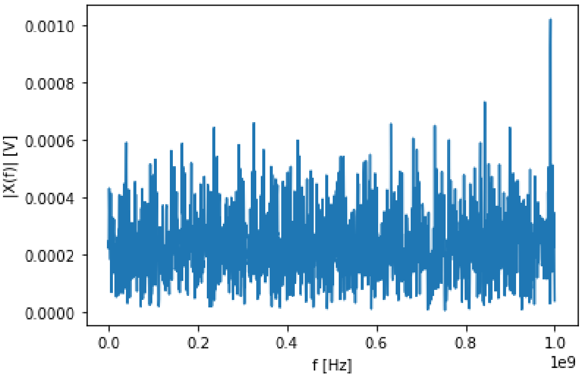

Figure 5.14: Frequency spectrum of the scan with radiation pattern pointing to the left cube

As for the central cube, from figure 5.13 it is possible to conclude that a target was detected, obtaining an amplitude of the sampled signal $A_{fft} = 5.433 \times 10^{-3}$ V, higher than the threshold voltage V_{th} represented in table 5.1. The surface of the central cube, in the $Blender$ scene, is at a distance of 200 m from the

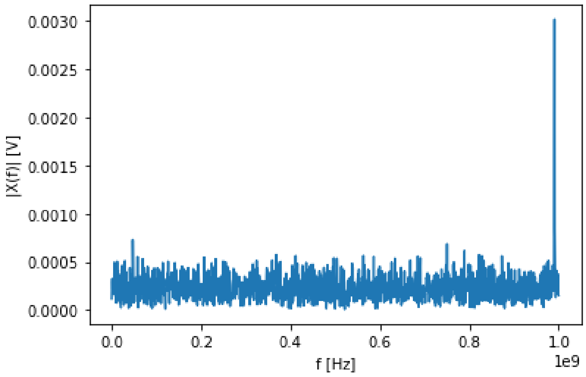

Figure 5.15: Frequency spectrum of the scan with radiation pattern pointing to the right cube

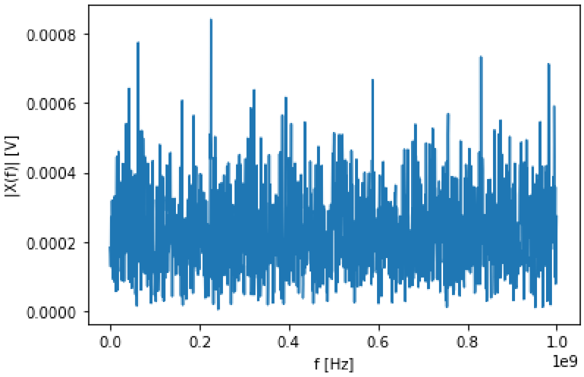

Figure 5.16: Frequency spectrum of the scan of one direction without target

camera. Thus, it was expected that the computed amplitude of the signal was very close to the threshold level. From the frequency corresponding to the maximum on the frequency spectrum, the computed distance was $R_{sim} = 199.4$ m.

The cubes on the left and on the right in figure 5.9 were not detected, as is verified by analysing figures 5.14 and 5.15. The amplitude obtained, from the maximum of the FFT, for the cube on the left was $A_{fft} = 1.021 \times 10^{-3}$ V, and for the cube on the right $A_{fft} = 3.015 \times 10^{-3}$ V, both being below the threshold voltage level V_{th}. However, it is possible to verify that, at a frequency corresponding to a distance of $R_{sim} = 198.05$ m, for both scans, the maximum of the FFT occurs, being noticeable among the noise. Note that in the $Blender$ scene, the center of the cubes were located at x=-170 m, y= ± 100 m and z = 0 m, being 198.95 m away from the camera. This leads to the conclusion that if more power were transmitted, the targets would probably be detected. Furthermore, the cubes are not positioned directly according to the maximum of the considered radiation patterns, and the transmitted power was calculated using the maximum gain of the central radiation pattern, that has a higher gain compared to the ones in the remaining directions (verify in annex A). Thus, there was a possibility that targets at directions in which the maximum gain of the antenna was lower than the one considered, would have a maximum detectable distance lower than the one defined.

For the directions that had no target, by analysing the frequency spectrum in figure 5.16, only noise was identified, without any peak that would stand out. This was the behaviour seen in every direction without any target.

5.4.2 Results for Environment B

The purpose of environment B was to verify that the radar system could identify a number of objects in its close vicinity, being the targets expected to be easily identifiable, with computed signal amplitudes much higher than the threshold level, since the targets are close to the camera. The image result of the simulation is depicted in figure 5.17. Targets were found in many directions, being represented with different colours in the figure, analogous to figure 5.8. The distance results obtained for each radiation pattern are represented in table 5.2, being a 7×7 sized table, corresponding to the data of the central 7×7 pixels of image 5.17. Note that, if the value of a cell in table 5.2 is NT (no target), it means that that no target was detected in that direction.

The sphere located at the left of figure 5.8 is identified by one of the radiation patterns. The frequency spectrum obtained from the simulated signal in this direction is represented in figure 5.18. The obtained

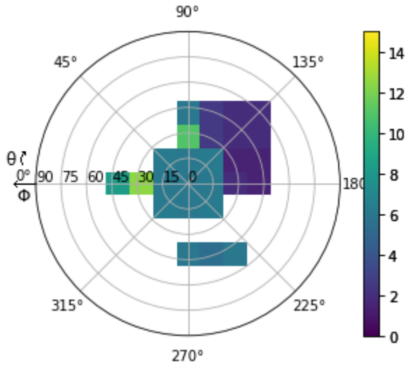

Figure 5.17: Simulation result image for Environment B

NT	NT	NT	5.997	2.549	1.949	1.949
NT	NT	NT	10.945	2.549	1.949	1.949
NT	NT	6.147	5.997	6.147	1.495	1.499
8.246	12.440	5.997	5.997	5.997	1.949	1.499
NT	NT	6.147	5.997	6.147	NT	NT
NT	NT	NT	NT	NT	NT	NT
NT	NT	NT	5.997	5.397	5.997	NT

Table 5.2: Obtained distances R_{sim} [m] for targets detected by each radiation pattern

amplitude of the maximum of the FFT exceeded the voltage threshold level V_{th}, being $A_{fft} = 2.7 \times 10^{-2}$ V, at a frequency that corresponds to a distance of 8.246 m, as represented in the position (column, row) = (1,4) of table 5.2. In the $Blender$ scene, the sphere is at a distance of 8.062 m of the camera.

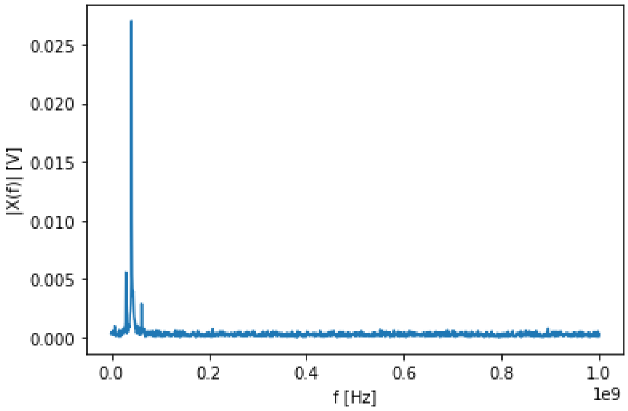

Figure 5.18: Frequency spectrum of the scan that identified the sphere in environment B

The object on the right of the sphere in figure 5.8 is a cylinder, and is also correctly identified by another radiation pattern. The frequency spectrum obtained from the simulated signal in this direction is represented in figure 5.19. The obtained amplitude from the maximum of the FFT is $A_{fft} = 6.934 \times 10^{-2}$ V, being higher than V_{th}, at a frequency that corresponds to the distance represented in position (2,4) of table 5.2. The distance of the cylinder to the camera in the $Blender$ scene is 11.66 m.

The cube in the center of figure 5.8 is identified by many radiation patterns, specifically the 3×3 central ones, as identified in positions (3,3), (4,3), (5,3), (3,4), (4,4), (5,4), (3,5), (4,5) and (5,5) of table 5.2. The amplitude of the signal computed from the FFT is higher on the radiation pattern that outputs result in index (4,4) of the referred table, since it covers a higher portion of the cube, while the radiation patterns that output the results in the rest of the mentioned indexes have similar computed amplitude, higher than the threshold level V_{th}. In figures 5.20, 5.21 and 5.22 are depicted the frequency spectrums of the results corresponding to indexes (4,4), (5,4), and (5,3) in table 5.2. The computed amplitude from the FFT was $A_{fft} = 1.53$ V, $A_{fft} = 0.14$ V and $A_{fft} = 2.72 \times 10^{-2}$ V for figures 5.20, 5.21 and 5.22, respectively, resulting in targets clearly identified. Note that the computed distances differ, since different portions of the cube are identified.

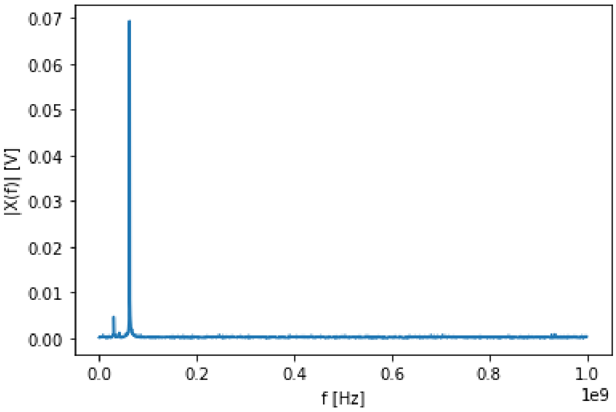

Figure 5.19: Frequency spectrum of the scan that identified the cylinder in environment B

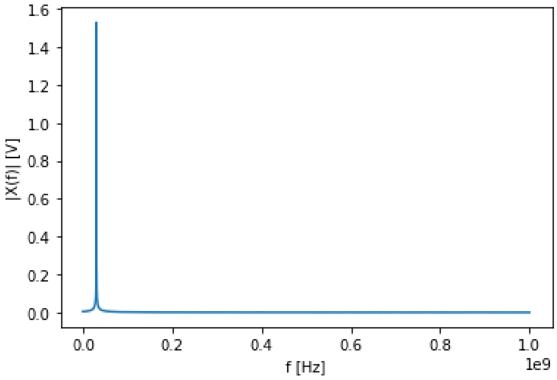

Figure 5.20: Frequency spectrum of index (4,4) that identified the central cube in environment B

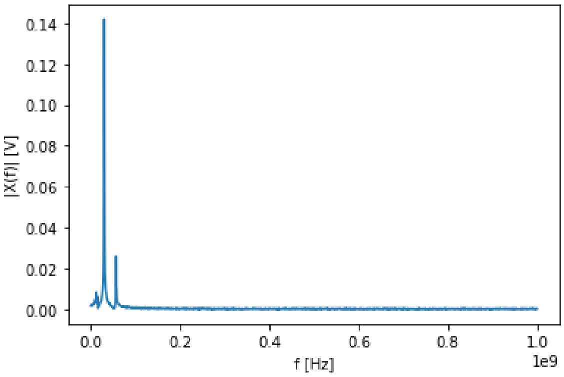

Figure 5.21: Frequency spectrum of index (5,4) that identified the central cube in environment B

The closest cube to the camera, located at the right of the central cube in figure 5.8, was also detected by many radiation patterns, being the results represented in indexes (1,5), (1,6), (1,7), (2,5), (2,6), (2,7), (3,6), (3,7), (4,6) and (4,7) of table 5.2. For this cube, the frequency spectrums obtained from the sampled signals were similar, showing a single peak corresponding to the maximum, with different computed amplitudes. The maximum of the amplitude obtained for these scans was $A_{fft} = 0.3$ V and the lower was $A_{fft} = 1.63 \times 10^{-2}$ V. The distance of the center of the cube to the camera in the *Blender* scene was 2 m.

The cube on top of the center cube was identified in scan with index (4,2) in table 5.2, being the computed amplitude of the signal $A_{fft} = 1.07 \times 10^{-2}$ V. The distance of this cube to the camera in *Blender* was 11 m.

The cube on bottom of the image was also identified by 3 different scans, represented in indexes (4,7), (5,7) and (6,7) of table 5.2. The amplitude computed from the FFTs of each signal was approximately

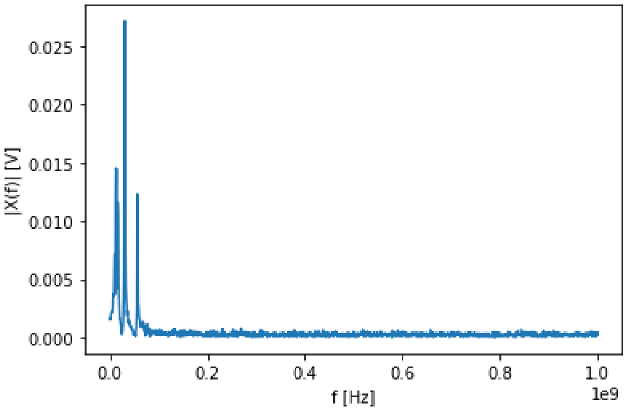

Figure 5.22: Frequency spectrum of index (5,3) that identified the central cube in environment B

$A_{fft} = 8 \times 10^{-3}$ V for indexes (4,7) and (6,7), being close to the threshold level, and $A_{fft} = 1.75 \times 10^{-2}$ V for the index (5,7), meaning that more area of the cube was hit with the mainbeam of the radiation pattern.

Furthermore, the results from the simulation in this environment detected a false positive, represented in index (4,1) of table 5.2. It is seen in figure 5.10 that no target is located at the considered direction, being the detection caused by the influence of the side lobes of the radiation pattern, that transmitted enough power to detect the central cube. The frequency spectrum relative to the result in index (4,1) of the referred table is depicted in figure 5.23, being noticeable that the detection was based on an amplitude that is very close to the threshold level. If the environment was truly unknown, the system could assume that a small target was found at the considered direction, since the computed distance is relatively small when compared to the maximum detectable distance R_{max}. However, since the environment is known, it is possible to affirm that is a false positive.

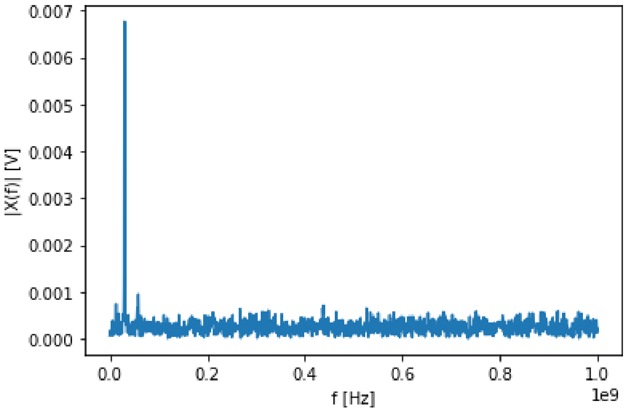

Figure 5.23: Frequency Spectrum of the signal that detected a false positive in environment B

The cube most on the right in figure 5.8 was not detected, since the array was not able to scan that direction. Also note that the cube behind the central cube was not identified. However, it is noticeable in the frequency spectrums, that there are peaks lower than the maximum, but higher than the threshold level, as seen in figures 5.18, 5.21 and 5.22. These peaks correspond to a component on the sampled signal at different frequencies, being related to objects located at different distances that also reflected the transmitted signal. The peaks at the left and at the right of the maximum in figure 5.22 were analysed, and the distances obtained were $R_{sim} = 2.6$ m and $R_{sim} = 11.3$ m, respectively. It is noticeable that these peaks were the result of the reflection of the signal in the cube that is closest to the camera, and in the cube behind the central cube, which is located at a distance of 11.5 m from the camera. If these peaks were considered in the target detection phase, the radar could detect 3 objects in this direction, each positioned at the corresponding computed distance.

For a safety system, it is of utmost importance that the system identifies the objects that are the nearest, in each direction. Thus, another simulation was done on environment B, considering that the detection was based on the first peak higher than the threshold level. This way, if many targets were detected by a scan, the closest one would be the one identified. The image result of the simulation is depicted in figure 5.24. It is noticeable, when comparing with figure 5.17, that some radiation patterns that identified the central cube, now identify the cube on the right, that is closest to the camera. Note that even on the central radiation pattern this cube was identified, instead of the central cube.

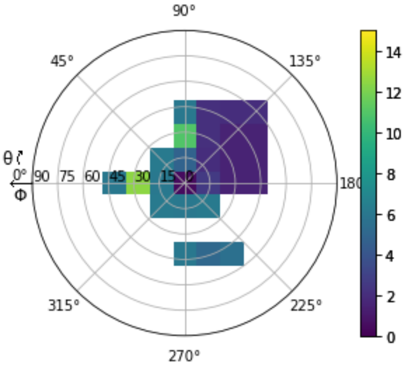

Figure 5.24: Simulation 2 result image - Environment B

5.5 Discussion and Future Work

In this chapter, a radar simulation algorithm was designed and validated, using an image of an environment developed in $Blender$ to be scanned with different radiation patterns, and perform a target detection analysis for each. Two environments were chosen, one to identify targets located at the defined maximum detectable distance, and another with a mesh of objects close to the camera position. In both environments, the radar was able to identify the objects.

The radar model described in section 5.1.1 was used to simulate the signals that would be received by the radar system, if it was located in the considered environment. A complete analysis was done, since the synthesis of a generic signal that would need to be adapted to be sent to each antenna element present in the array, to the signal that would be digitally processed to perform the detection techniques, along with an analysis of the power propagation in space according to the image characteristics, and to each radiation pattern considered.

The target detection technique used to perform target detection is described in section 5.1.3, consisting on an analysis of the frequency spectrum obtained from the simulated signal, with the purpose of identifying its strength, to claim or not the detection of a target. The detection threshold level was based on the false alarm probability of the radar, which is a parameter often considered to determine the reliability of a radar system. Furthermore, if a target was detected, its distance was correctly identified, being computed based on the frequency corresponding to the maximum of the frequency spectrum. However, it was found that in some directions, there were other peaks, lower than the maximum, but higher than the threshold level. Since the objective of this work is to focus on a safety system, a target identification technique was used, in which the distance to the target was computed based on the frequency of the first peak higher than the threshold level.

In some directions, the difference in the obtained targets distance is visible, providing the data regarding the objects closer to the camera.

Since the environment is known, it was possible to conclude that in the simulation the targets were identified correctly as expected. However, it was also noticeable that if an antenna array with higher angular resolution was used, it was possible to achieve a more precise target detection, since there would be a higher number of directions scanned in the same covered area, resulting in a more detailed final result. There is also another reason to increase the angular resolution of the array. Since more antenna elements would be present, the gain of the array would be higher, that would have a direct attenuation on the necessary transmitted power by the radar system. Note that, the maximum detectable distance considered in the simulation was $R_{max} = 200$ m, and the necessary transmitted power was 7.26 W, however, by considering the same characteristics, but with a maximum detectable distance of $R_{max} = 2000$ m, the necessary transmitted power would be 72.6 kW. This is a huge increase, due to the relation between transmitted power and detectable distance, but also emphasising the effect of the higher attenuation of signals when using mm-wave frequencies.

According to the ELOS for see and avoid, a minimum time to colision of 21 s is required for the sensing systems [17]. The velocity of the state of the art low flying altitude air vehicles can reach up to 100 km/h, [84], corresponding to a necessary distance of detection of 583 m. For the distance of 200 m considered in the simulations, the vehicle velocity should not exceed 34.29 km/h. A simulation was done, considering the state of the art vehicles requirements, to detect objects at 583 m. The results are depicted in annex B.

As future work, this simulation could be enhanced by interconnecting more $Blender$ capabilities with the script. One suggestion is to import an environment from $Google\ Maps$ using the addon $Blender\ GIS$ [85], and create a path for the camera to dynamically acquire the image renders, while performing the simulation at each position. This could be complemented by considering that the simulated radar system, instead of transmitting a single chirp, was transmitting a train of chirps, allowing to also compute the relative velocity between the system and each detected object [39]. Furthermore, the target detection technique can also be enhanced, by considering the peaks of the FFT with lower magnitude than the maximum, but higher than the threshold level, allowing to detect more than one target at each direction. Note that this has to be carefully analysed, since it could lead to the increase of false detections.

Chapter 6

Conclusion

This thesis intends to contribute to the study and possible development of a safety system for low flying vehicles, with special attention given to Radar systems due to its reliability in different environment conditions. The theme was developed aiming to allow the definition of a complete configuration of the system according to the needs of the design, starting with the single antenna element, followed by the specification of the array and ending with the specification of the complete radar system.

The design of the patch antenna single element was made using two well known models, the transmission line and cavity models. This models have previously output accurate results [28] [24], and in this work, the results were optimised using a eletromagnetic field simulation software tool. The result was a patch antenna that resonates at the desired frequency. The antenna should identify targets as reliably as possible, and since losing targets due to a polarization mismatch is a known phenomena [26], the antenna was designed with dual linear polarization, intended to output similar radiation patterns for both vertical and horizontal polarizations. By achieving this, the probability of missing a target detection due to polarization mismatch is decreased.

The antenna array used in a radar system is directly related to the detail of the objects identified, since its characteristics control the width of the mainbeam and the gain of the radiation pattern. The higher the angular resolution, the more angular directions can be scanned, the higher the gain, and the larger the distance of detectable targets. However, in order to avoid false detections, the sidelobe level of the array must be controlled. This was achieved using the well-known narrow-beam low side lobe level Dolph-Chebyshev design, obtaining an array with the maximum possible gain for the desired side lobe level. Furthermore, the array mainbeam direction was controlled, providing steering capabilities, allowing to scan multiple directions with a fixed antenna. By achieving this, more angular directions can be accurately scanned.

The characteristics of the radar system are highly dependent on the working frequency of the used antenna. In this work, mm-Wave frequencies were considered, and a radar system suitable to be used with antennas optimised for this frequency band was studied. Since the production of such a radar is expensive, the validation of the system was done by simulating an environment with objects to be identified. By achieving this, it was proven the concept of using a highly directive radar to identify detected objects relative to its own position, data that could be used to prevent colisions of air flying vehicles.

6.1 Achievements

In this work a radar system was modelled, and by controlling the characteristics of the sensing antenna, a system capable of identifying and positioning targets in its surroundings was created.

A design model for a squared patch antenna with dual linear polarization was achieved, being versatile in terms of resonant frequency. The model was tested to design a patch resonating at 35 GHz, obtaining accurate results.

An antenna array with a narrow mainbeam and low side lobe level was modelled, with the capability of being steered according to its half-power beam-width. By increasing the number of elements, it is possible to achieve a narrower mainbeam, and thus the number of possible scanned angular directions. The radiation patterns were analysed for both polarizations of the used antenna, being a similar behaviour verified for both. The array was designed with 8x8 elements, leading to a 22.9 dBi gain, a 1° half-power beamwidth and a -25.7 dB side lobe level, for the broadside direction pointing situation.

A radar simulation technique using the open source software $Blender$ was developed, with the intention of allowing to optimise a radar system. In this simulation tool, a preview of the behaviour of the radar system in a defined environment is obtained, allowing to identify possible improvements that could enhance the system performance for the desired purpose. A conceptual validation was done, by creating simple environments and correctly identifying the objects within them.

The simulations were done, by defining the transmitted power and the sensitivity of the radar according to the maximum distance desired to detect a target. One environment with a single object at approximately the defined distance away from the camera was made, being the object detected in the simulation, with an amplitude of the simulated signal nearly the threshold level. Another environment was studied, with many objects located close to the camera, being the system able to identify the targets correctly. However, in certain directions, the computed distance was not in respect to the object closest to the camera, being a detection algorithm implemented, in which the distance of the detected target was computed according to the frequency of the first peak in the frequency spectrum, higher than the threshold level. Furthermore, a validation of the designed system according to the ELOS for see and avoid was also analysed (annex B).

6.2 Future Work

The future work is vast, as stated at the end of chapters 3, 4 and 5. For the single patch antenna, an element that operates at a frequency of the state of the art long range automotive radars (77 GHz) could be done, along with an implementation of either proximity or aperture coupled feed. The antenna array could be designed with a higher number of elements, along with a study of the implementation of cylindrical arrays. The radar simulation could be enhanced by interconnecting more $Blender$ capabilities with the script, and creating a real scaled environment using data from $Google\ Maps$ street view, with the purpose of obtaining a video of the system navigating through it, along with the results of the simulations. The radar detection can also be enhanced, by considering a pulse of chirps, being also able to compute the relative velocity of the detected targets, and by implementing a detection algorithm that considers many peaks from the frequency spectrum of each radar signal, to identify targets at different distances in the same direction.

As for the overall theme, the data regarding the objects identified in many simulations could be processed by a SLAM algorithm, with the objective of creating a map of the sensed environment. This development is fundamental to the objective of creating a safety system, since it would allow to limit the movement of a flying vehicle according to the objects presented in its surroundings.

Beyond optimising the created system and the correlation of the simulated data using SLAM, an experimental validation should be done. Although very demanding and expensive, the fabrication and test of the complete system should be a goal.

References

[1] Merrill I. Skolnik. “The Nature of Radar”. In: *Introduction to Radar Systems, 2nd Edition*. McGraw-Hill Book Company, 1981. ISBN: 0-07-057909-1.

[2] Johan Alexandersson och Olle Nordin. “Implementation of SLAM algorithms in a small-scale vehicle using model-based development”. MA thesis. Department of Electrical Engineering, Linköping University, Linköping, Sweden, 2017.

[3] Oscar A. Martinez and Manuel Cardona. “State of the Art and Future Trends on Unmanned Aerial Vehicle”. In: *International Conference on Research in Intelligent and Computing in Engineering (RICE)* (2018). DOI: 10.1109/RICE.2018.8509091.

[4] I. Colomina and P. Molina. “Unmanned aerial systems for photogrammetry and remote sensing: A review”. In: *ISPRS Journal of Photogrammetry and Remote Sensing* 92 (2014), pp. 79–97. DOI: 10.1016/j.isprsjprs.2014.02.013.

[5] Jawad N. Yasin et al. “Unmanned Aerial Vehicles (UAVs): Collision Avoidance Systems and Approaches”. In: *IEEE Access (Volume: 8)* (2020), pp. 105139–105155. DOI: 10.1109/ACCESS.2020.3000064.

[6] Sanjiv Singh, Christopher Geyer, and Lyle Chamberlain. *Avoiding Collisions Between Aircraft: State of the Art and Requirements for UAVs operating in Civilian Airspace*. Manual CMU-RI-TR-08-03, Robotics Institute, Carnegie Mellon University, Pittsburgh. 2008.

[7] Malcolm Mielle, Martin Magnusson, and Achim J. Lilienthal. “A comparative analysis of radar and lidar sensing for localization and mapping”. In: *2019 European Conference on Mobile Robots (ECMR)* (2019). DOI: 10.1109/ECMR.2019.8870345.

[8] Constantine A. Balanis. “Microstrip Antennas”. In: *Antenna Theory Analysis and Design, 2nd Edition*. John Wiley & Sons Inc., 1938. ISBN: 0-471-59268-4.

[9] Jing Song, Xu Sun, and Shuang Wu. “Design of 77 GHz Narrow Beamwidth Antenna for UAVs Obstacle Avoidance Radar”. In: *International Conference on Microwave and Millimeter Wave Technology (ICMMT)* (2018). DOI: 10.1109/ICMMT.2018.8563313.

[10] Monika Ouza, Michael Ulrich, and Bin Yang. “A Simple Radar Simulation Tool for 3D Objects based on Blender”. In: *18th International Radar Symposium (IRS)* (2017). DOI: 10.23919/IRS.2017.8008254.

[11] Cesar Cadena et al. "Past, Present, and Future of Simultaneous Localization And Mapping: Towards the Robust-Perception Age". In: *IEEE Transactions on Robotics (Volume: 32, Issue: 6)* (2016), pp. 1309–1332. DOI: 10.1109/TRO.2016.2624754.

[12] Sophocles J. Orfanidis. "Reflection and Transmission". In: *Electromagnetic Waves and Antennas*. Rutgers University, 2016. URL: http://eceweb1.rutgers.edu/~orfanidi/ewa/ch15.pdf.

[13] Raphaël Rouveure, Patrice Faure, and Marie-Odile Monod. "Radar imager for perception and mapping in outdoor environnements". In: *Advanced Concepts for Intelligent Vision Systems, 11th International Conference, ACIVS 2009* (2009). DOI: 10.1007/978-3-642-04697-1_58.

[14] Justin Bode and Arslan Munir. "OTMS: A Novel Radar-Based Mapping System for Automotive Applications". In: *2020 IEEE 17th Annual Consumer* (2020). DOI: 10.1109/CCNC46108.2020.9045231.

[15] G. Ludeno et al. "A micro-UAV-borne system for radar imaging: A feasibility study". In: *2017 9th International Workshop on Advanced Ground Penetrating Radar (IWAGPR)* (2017). DOI: 10.1109/IWAGPR.2017.7996034.

[16] Allistair Moses et al. "UAV-borne X-band radar for collision avoidance". In: *Cambridge University Press 2013, Robotica volume 32* (2014), pp. 97–114. DOI: 10.1017/S0263574713000659.

[17] Young K Kwag et al. "Collision Avoidance Radar for UAV". In: *2006 CIE International Conference on Radar* (2006). DOI: 10.1109/ICR.2006.343231.

[18] Jorge Vargas et al. "An Overview of Autonomous Vehicles Sensors and Their Vulnerability to Weather Conditions". In: *Sensors* 21.16 (2021). ISSN: 1424-8220. DOI: 10.3390/s21165397. URL: https://www.mdpi.com/1424-8220/21/16/5397.

[19] Marc L. Schoen et al. "Real-Time Radar SLAM". In: 2017 Workshop Fahrerassistenzsysteme und automatisiertes Fahren. URL: https://www.uni-das.de/images/pdf/veroeffentlichungen/2017/01.pdf.

[20] Custódio Peixeiro. "Microstrip Antenna Papers in the IEEE Transactions on Antennas and Propagation [EurAAP Corner]". In: *IEEE Antennas and Propagation Magazine* 54.1 (2012), pp. 264–268. DOI: 10.1109/MAP.2012.6202561.

[21] Abdullahi SB. and Mohammed et al. "Microstrip Patch Antenna: A Review and the Current State of the Art". In: *Journal of Advanced Research in Dynamical and Control Systems* 11.07-Special Issue (2019), pp. 510–524. ISSN: 1943-023X.

[22] Stéphane Kemkemian et al. *Radar systems for "Sense and Avoid" on UAV*. International Radar Conference 'Surveillance for a Safer World', 2009, pp. 1–6. ISBN: 978-2-912328-55-7.

[23] K. Siakavara. "Methods to Design Microstrip Antennas for Modern Applications". In: *Microstrip Antennas*. IntechOpen, 2011. URL: https://www.researchgate.net/publication/221911599_Methods_to_Design_Microstrip_Antennas_for_Modern_Applications.

[24] Ahmed Fatthi Alsager. “Design and Analysis of Microstrip Patch Antenna Arrays”. MA thesis. University College of Borås, 2011.

[25] Sonia Sharma, C. C. Tripathi, and Rahul Rishi. “Impedance Matching Techniques for Microstrip Patch Antenna”. In: *Indian Journal of Science and Technology, Vol 10(28)* (2017), pp. 1–16. DOI: 10.17485/ijst/2017/v10i28/97642.

[26] Mark A. Govoni, Jeffrey Spak, and Lee R. Moyer. “Analysis of Polarization Mismatch Loss for Horizontal Linear Feature Detection”. In: Distribution A 2012. URL: https://apps.dtic.mil/sti/pdfs/ADA569945.pdf.

[27] M. S. R Mohd Shah et al. “Dual Linearly Polarized Microstrip Array Antenna”. In: *Trends in Telecommunications Technologies*. Ed. by Christos Bouras. Intech Open, 2010. DOI: 10.5772/8468.

[28] Christopher B. Smith. “Wideband Dual-Linear Polarized Microstrip Patch Antenna”. MA thesis. Texas AM University, 2008.

[29] Shuchismita Pani, Malay Tripathy, and Arun Kumar. “Analysis of beam steering quality of 2-dimensional microstrip patch antenna array”. In: *International Journal of System Assurance Engineering and Management* 12 (2021). DOI: 10.1007/s13198-021-01112-z.

[30] Sophocles J. Orfanidis. “Array Design Methods”. In: *Electromagnetic Waves and Antennas*. Rutgers University, 2016. URL: http://eceweb1.rutgers.edu/~orfanidi/ewa/ch23.pdf.

[31] Mst Hasneara Khatun, Reefat Inum, and Nazia Tasnim. “Design of Rectangular Patch Antenna Array Using Different Feeding Technique”. In: *2017 2nd International Conference on Electrical Electronic Engineering (ICEEE)* (2017), pp. 1–4. DOI: 10.1109/CEEE.2017.8412882.

[32] Vasujadevi Midasala and P. Siddaiah. “Microstrip Patch Antenna Array Design to Improve Better Gains”. In: *Procedia Computer Science* 85 (2016). International Conference on Computational Modelling and Security (CMS 2016), pp. 401–409. ISSN: 1877-0509. DOI: https://doi.org/10.1016/j.procs.2016.05.181.

[33] Sophocles J. Orfanidis. “Antenna Arrays”. In: *Electromagnetic Waves and Antennas*. Rutgers University, 2016. URL: http://eceweb1.rutgers.edu/~orfanidi/ewa/ch22.pdf.

[34] Murad Ridwan, Mohammed Abdo, and Eduard Jorswieck. “Design of non-uniform antenna arrays using genetic algorithm”. In: *13th International Conference on Advanced Communication Technology (ICACT2011)* (2011), pp. 422–427.

[35] C.A. Olen and R.T. Compton. “A numerical pattern synthesis algorithm for arrays”. In: *International Symposium on Antennas and Propagation Society, Merging Technologies for the 90’s*. 1990, 828–831 vol.2. DOI: 10.1109/APS.1990.115236.

[36] N. Fadlallah et al. “Antenna Array Synthesis with Dolph-Chebyshev Method”. In: *11TH Mediterranean Microwave Symposium* (2011).

[37] Henry H. Vo and Chi-Chih Chen. “Frequency and scan angle limitations in UWB phased array”. In: *The 8th European Conference on Antennas and Propagation (EuCAP 2014)*. 2014, pp. 3627–3629. DOI: 10.1109/EuCAP.2014.6902615.

[38] Shahid Mumtaz, Jonathan Rodriguez, and Linglong Dai. “Chapter 9 - mmWave communication enabling techniques for 5G wireless systems: A link level perspective”. In: *mmWave Massive MIMO*. Academic Press, 2017, pp. 195–225. ISBN: 978-0-12-804418-6. DOI: https://doi.org/10.1016/B978-0-12-804418-6.00009-1.

[39] Cesar Iovescu and Sandeep Rao. *The fundamentals of millimeter wave radar sensors (Online)*. Texas Instruments. 2020. URL: https://www.ti.com/lit/wp/spyy005a/spyy005a.pdf?ts=1657996907338.

[40] Yosef Golovachev et al. “Millimeter Wave High Resolution Radar Accuracy in Fog Conditions-Theory and Experimental Verification”. In: *Sensors* 18 (2018). DOI: 10.3390/s18072148.

[41] H.D. Griffiths. “New ideas in FM radar”. In: *Electronics Communication Engineering Journal* 2 (5 1990), 185–194(9). ISSN: 0954-0695. URL: https://digital-library.theiet.org/content/journals/10.1049/ecej_19900043.

[42] A.G. Stove. “Modern FMCW radar - techniques and applications”. In: *First European Radar Conference EURAD*. 2004, pp. 149–152.

[43] Prajakta Desai, Keegan Garcia, and Osamah Ahmad. *How antenna-on-package design simplifies mmWave sensing in buildings and factories (Online)*. Texas Instruments. 2020. URL: https://www.ti.com/lit/wp/spry334a/spry334a.pdf?ts=1620999405802.

[44] David Marsh. “Radar reflects safer highways”. In: *EDN* 48.9 (2003), pp. 51–51.

[45] Wentao Zhu et al. “Design of Millimeter-wave Transmitter Based on FPGA”. In: *2019 IEEE 6th International Symposium on Electromagnetic Compatibility (ISEMC)*. 2019, pp. 1–4. DOI: 10.1109/ISEMC48616.2019.8986092.

[46] Tolga Dinc and Harish Krishnaswamy. “Millimeter-wave full-duplex wireless: Applications, antenna interfaces and systems”. In: *2017 IEEE Custom Integrated Circuits Conference (CICC)*. 2017, pp. 1–8. DOI: 10.1109/CICC.2017.7993663.

[47] Gregor Hasenäcker et al. “A SiGe Fractional-N Frequency Synthesizer for mm-Wave Wideband FMCW Radar Transceivers”. In: *IEEE Transactions on Microwave Theory and Techniques* 64 (2016), pp. 847–858. DOI: 10.1109/TMTT.2016.2520469.

[48] Martin L. Smith et al. “A simple Eletronically-Phased Acoustic Array”. In: *Acoustics Today* (2013), pp. 22–29. URL: https://acousticstoday.org/a-simple-electronically-phased-acoustic-array-martin-l-smith-martin-l-smith-michael-r-roddewig-kurt-m-strovink-john-a-scales/.

[49] D. Govind Rao et al. “Digital beam former architecture for sixteen elements planar phased array radar”. In: *2013 The International Conference on Technological Advances in Electrical, Electronics and Computer Engineering (TAEECE)*. 2013, pp. 532–537. DOI: 10.1109/TAEECE.2013.6557331.

[50] Wenjing Shang et al. “Digital beamforming based on FPGA for phased array radar”. In: *2017 Progress In Electromagnetics Research Symposium - Spring (PIERS)*. 2017, pp. 437–440. DOI: 10.1109/PIERS.2017.8261779.

[51] Monika Ouza, Michael Ulrich, and Bin Yang. “A simple radar simulation tool for 3D objects based on blender”. In: *2017 18th International Radar Symposium (IRS)*. 2017, pp. 1–10. DOI: 10.23919/IRS.2017.8008254.

[52] Rômulo Fernandes da Costa, Raíssa Andrade, and Renato Machado. “Simulador Radar baseado no software Blender”. In: *XXXVIII Simpósio Brasileiro de Telecomunicações e Processamento de Sinais* (2020). DOI: 10.14209/SBRT.2020.1570656801.

[53] Rômulo Fernandes da Costa et al. “General Purpose Radar Simulator based on Blender Cycles Path Tracer”. In: *XXXVIII Simpósio Brasileiro de Telecomunicações e Processamento de Sinais* (2020). DOI: 10.14209/SBRT.2020.1570649487.

[54] Hyun Eugin and Jonghun Lee. “Hardware architecture design and implementation for FMCW radar signal processing algorithm”. In: *Proceedings of the 2014 Conference on Design and Architectures for Signal and Image Processing*. 2014, pp. 1–6. DOI: 10.1109/DASIP.2014.7115643.

[55] Matthias Kronauge and Hermann Rohling. “New chirp sequence radar waveform”. In: *IEEE Transactions on Aerospace and Electronic Systems* 50.4 (2014), pp. 2870–2877. DOI: 10.1109/TAES.2014.120813.

[56] *OpenEXR*. URL: https://www.openexr.com/.

[57] Michel Thoby. *Models for the various classical lens projections (Online)*. Michel Thoby Free. 2012. URL: http://michel.thoby.free.fr/Fisheye_history_short/Projections/Models_of_classical_projections.html.

[58] Ji Zhang and Sanjiv Singh. “LOAM: Lidar Odometry and Mapping in Real-time”. In: 2014. DOI: 10.15607/RSS.2014.X.007.

[59] Richard Szeliski. “Image formation”. In: *Computer Vision: Algorithms and Applications, 2nd Edition*. Springer, 2021. ISBN: 978-3030343712.

[60] Sophocles J. Orfanidis. “Impedance Matching”. In: *Electromagnetic Waves and Antennas*. Rutgers University, 2016. URL: http://eceweb1.rutgers.edu/~orfanidi/ewa/ch13.pdf.

[61] Sophocles J. Orfanidis. “S-Parameters”. In: *Electromagnetic Waves and Antennas*. Rutgers University, 2016. URL: http://eceweb1.rutgers.edu/~orfanidi/ewa/ch14.pdf.

[62] Tawfik Ismail, Erich Leitgeb, and Thomas Plank. "Free Space Optic and mmWave Communications: Technologies, Challenges and Applications". In: *IEICE Transactions on Communications* E99.B (2016). DOI: 10.1587/transcom.2015EUI0002.

[63] *AWR Tx-Line 2003*. URL: https://www.cadence.com/ko_KR/home/tools/system-analysis/rf-microwave-design/awr-tx-line.html.

[64] *Automotive Radar Frequency Bands*. https://www.everythingrf.com/community/automotive-radar-frequency-bands. Accessed: 2022-09-22.

[65] Sophocles J. Orfanidis. "Radiation Fields". In: *Electromagnetic Waves and Antennas*. Rutgers University, 2016. URL: http://eceweb1.rutgers.edu/~orfanidi/ewa/ch15.pdf.

[66] Natanael Karjanto. "Properties of Chebyshev Polinomials". In: *Scientifique de l'AEIF 2* 2 (2002), pp. 127–132. DOI: arXiv:2002.01342v1.

[67] Sophocles J. Orfanidis. *Electromagnetic Waves and Antennas*. 2016. URL: http://eceweb1.rutgers.edu/~orfanidi/ewa/.

[68] Mattia Rebato et al. "Study of Realistic Antenna Patterns in 5G mmWave Cellular Scenarios". In: *2018 IEEE International Conference on Communications (ICC)*. 2018, pp. 1–6. DOI: 10.1109/ICC.2018.8422746.

[69] J. Proakis. "Microstrip Antennas". In: *Digital Communications, 4th ed.* McGraw-Hill, 2001. URL: https://arnabiitk.files.wordpress.com/2013/02/proakis-digital-communications-4th-ed.pdf.

[70] Muhammad Z. Ikram, Adeel Ahmad, and Dan Wang. "High-accuracy distance measurement using millimeter-wave radar". In: *2018 IEEE Radar Conference (RadarConf18)*. 2018, pp. 1296–1300. DOI: 10.1109/RADAR.2018.8378750.

[71] A. Hajimiri et al. "Integrated Phased Array Systems in Silicon". In: *Proceedings of the IEEE* 93.9 (2005), pp. 1637–1655. DOI: 10.1109/JPROC.2005.852231.

[72] Sophocles J. Orfanidis. "Transmitting and Receiving Antennas". In: *Electromagnetic Waves and Antennas*. Rutgers University, 2016. URL: http://eceweb1.rutgers.edu/~orfanidi/ewa/ch16.pdf.

[73] Merrill I. Skolnik. "The Radar Equation". In: *Introduction to Radar Systems, 2nd Edition*. McGraw-Hill Book Company, 1981, pp. 1–13. ISBN: 0-07-057909-1.

[74] Steven W. Smith. "8: The Discrete Fourier Transform". In: *The Scientist and Engineer's Guide to Digital Signal Processing*. Newnes, 2002. ISBN: 0-7506-7444-X. URL: http://www.dspguide.com/CH8.PDF.

[75] Steven W. Smith. "5: Linear Systems". In: *The Scientist and Engineer's Guide to Digital Signal Processing*. Newnes, 2002. ISBN: 0-7506-7444-X. URL: http://www.dspguide.com/CH5.PDF.

[76] Steven W. Smith. “12: The Fast Fourier Transform”. In: *The Scientist and Engineer’s Guide to Digital Signal Processing*. Newnes, 2002. ISBN: 0-7506-7444-X. URL: http://www.dspguide.com/CH12.PDF.

[77] Steven W. Smith. “10: Fourier Transform Properties”. In: *The Scientist and Engineer’s Guide to Digital Signal Processing*. Newnes, 2002. ISBN: 0-7506-7444-X. URL: http://www.dspguide.com/CH10.PDF.

[78] Michael Cerna and Audrey F. Harvey. *The Fundamentals of FFT-Based Signal Analysis and Measurement*. Manual 340555B-01. National Instruments. 2020. URL: https://www.sjsu.edu/people/burford.furman/docs/me120/FFT_tutorial_NI.pdf.

[79] *Rician Distribution (Rice Distribution): Definition Examples*. https://www.statisticshowto.com/rician-distribution-rice/. Accessed: 2022-08-20.

[80] Fernando D. Nunes. “Notes on Air Traffic Control Systems”. In: DEEC, Instituto Superior Técnico, Lisbon, Portugal, 2018.

[81] Richard Hartley and Andrew Zisserman. “Camera Models”. In: *Multiple View Geometry in Computer Vision, Second edition*. Cambridge University Press, 2003, pp. 153–176.

[82] *Tiny Planet Algorithm?* https://math.stackexchange.com/questions/607353/tiny-planet-algorithm. Accessed: 2022-08-20.

[83] Merrill I. Skolnik. “Radar Cross Section”. In: *Radar Handbook, Third Edition*. McGraw-Hill, 1990. ISBN: 0-07-057913-X.

[84] *Ehang 184 Autonomous Aerial Vehicle (AAV)*. https://www.aerospace-technology.com/projects/ehang-184-autonomous-aerial-vehicle-aav/. Accessed: 2022-10-25.

[85] *Blender GIS*. URL: https://github.com/domlysz/BlenderGIS.

Appendix A

Steered Radiation Patterns

This appendix presents the results of the several simulations done in $CSTStudioSuite$ with the antenna array model, shown in figure 4.10, using the feed weights presented in table 4.3, and phase shift between elements presented in table 4.6. Figures A.1, A.2, A.3, A.4, A.5, A.6,A.7, A.8, A.9, A.10, A.11, A.12, A.13, A.14 and A.15 show the 3d view of all the radiation patterns simulated, which are linked to the corresponding result section that contains the principal planes of the steered radiation pattern and the corresponding Equirectangular and Fisheye Equidistant Projection. Note that the presented radiation patterns are at a frequency of 35 GHz.

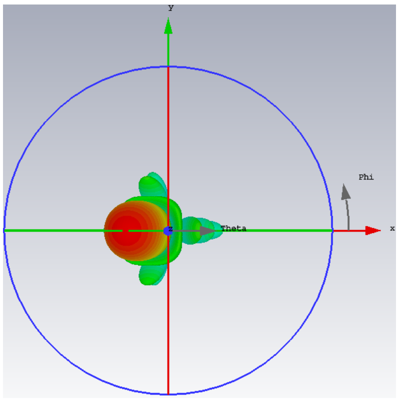

Figure A.1: Steered radiation pattern with $\psi_{0y} = 0°$ and $\psi_{0x} = 46°$

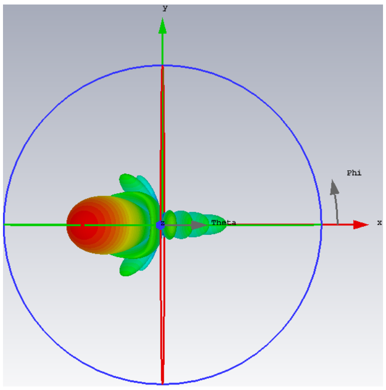

Figure A.2: Steered radiation pattern with $\psi_{0y} = 0°$ and $\psi_{0x} = 90°$

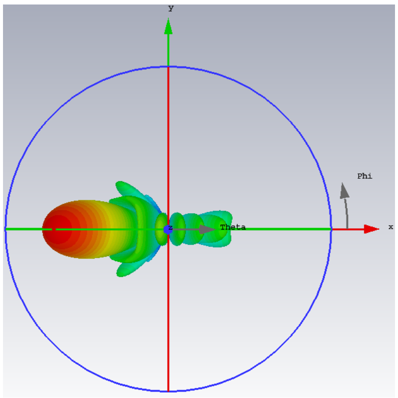

Figure A.3: Steered radiation pattern with $\psi_{0y} = 0^\circ$ and $\psi_{0x} = 127^\circ$

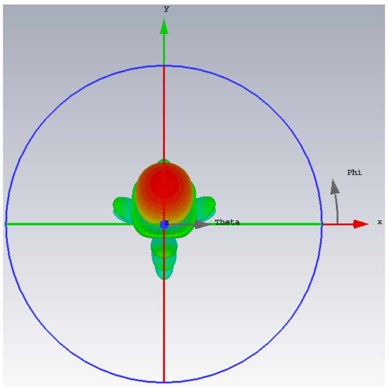

Figure A.4: Steered radiation pattern with $\psi_{0y} = 46^\circ$ and $\psi_{0x} = 0^\circ$

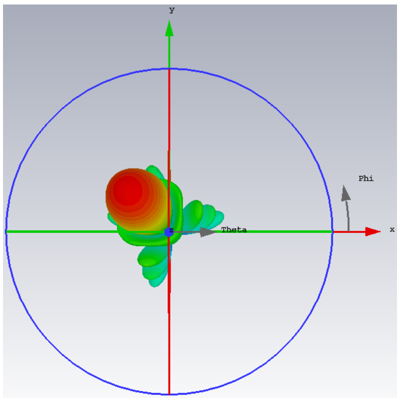

Figure A.5: Steered radiation pattern with $\psi_{0y} = 46^\circ$ and $\psi_{0x} = 46^\circ$

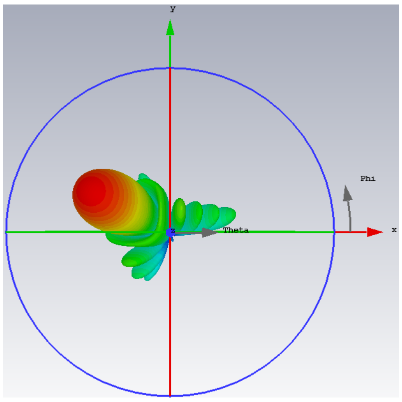

Figure A.6: Steered radiation pattern with $\psi_{0y} = 46^\circ$ and $\psi_{0x} = 90^\circ$

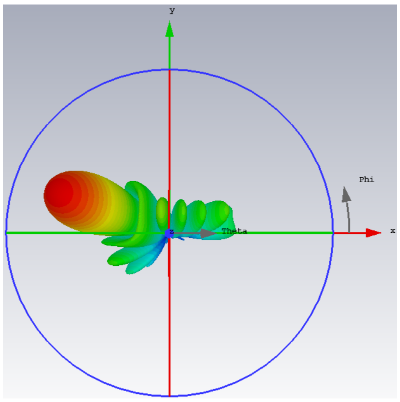

Figure A.7: Steered radiation pattern with $\psi_{0y} = 46^\circ$ and $\psi_{0x} = 127^\circ$

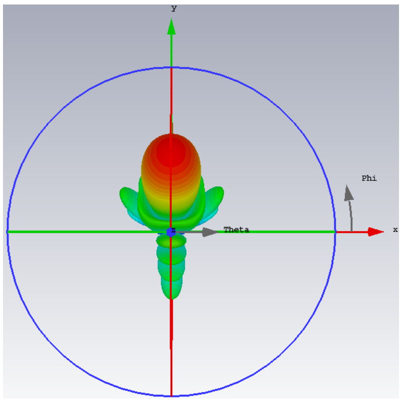

Figure A.8: Steered radiation pattern with $\psi_{0y} = 90^\circ$ and $\psi_{0x} = 0^\circ$

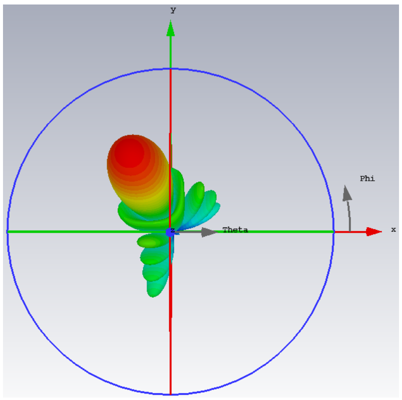

Figure A.9: Steered radiation pattern with $\psi_{0y} = 90^\circ$ and $\psi_{0x} = 46^\circ$

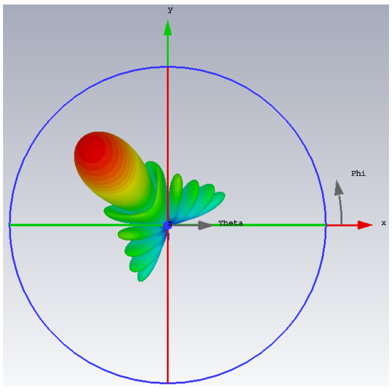

Figure A.10: Steered radiation pattern with $\psi_{0y} = 90^\circ$ and $\psi_{0x} = 90^\circ$

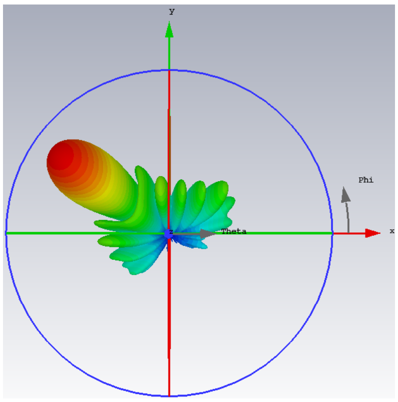

Figure A.11: Steered radiation pattern with $\psi_{0y} = 90^\circ$ and $\psi_{0x} = 127^\circ$

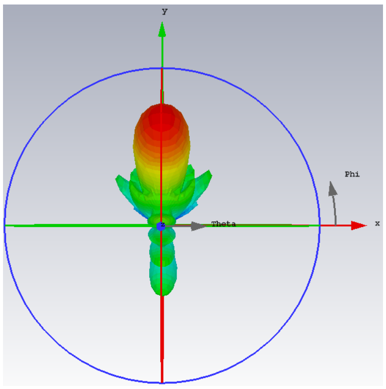

Figure A.12: Steered radiation pattern with $\psi_{0y} = 127^\circ$ and $\psi_{0x} = 0^\circ$

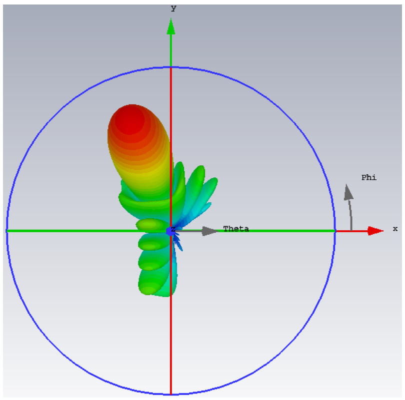

Figure A.13: Steered radiation pattern with $\psi_{0y} = 127^\circ$ and $\psi_{0x} = 46^\circ$

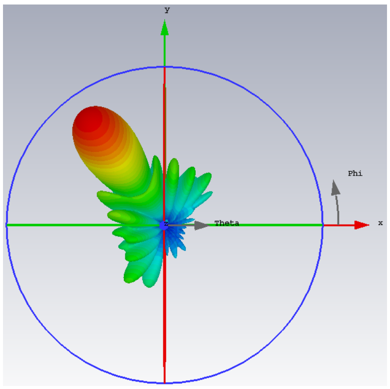

Figure A.14: Steered radiation pattern with $\psi_{0y} = 127^\circ$ and $\psi_{0x} = 90^\circ$

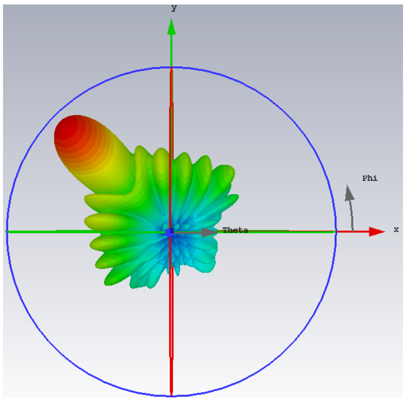

Figure A.15: Steered radiation pattern with $\psi_{0y} = 127°$ and $\psi_{0x} = 127°$

Steered radiation pattern with $\psi_{0y} = 0°$ and $\psi_{0x} = 46°$

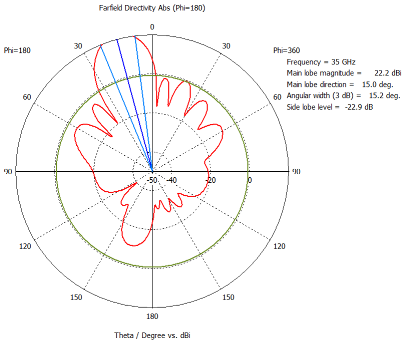

Figure A.16: Steered Radiation Pattern cut $\phi = 180°$

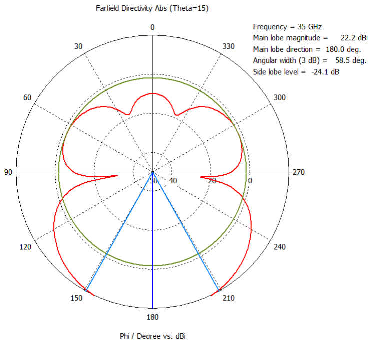

Figure A.17: Steered Radiation Pattern cut $\theta = 15°$

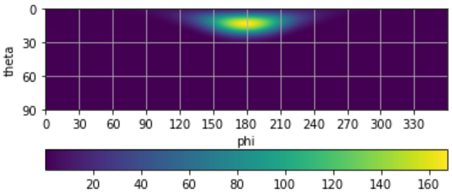

Figure A.18: Steered Radiation Pattern $(\theta, \phi) = (15°, 180°)$ equirectangular projection

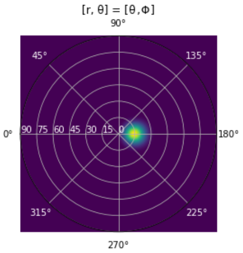

Figure A.19: Steered Radiation Pattern $(\theta, \phi) = (15°, 180°)$ fisheye equidistant projection

Steered radiation pattern with $\psi_{0y} = 0°$ and $\psi_{0x} = 90°$

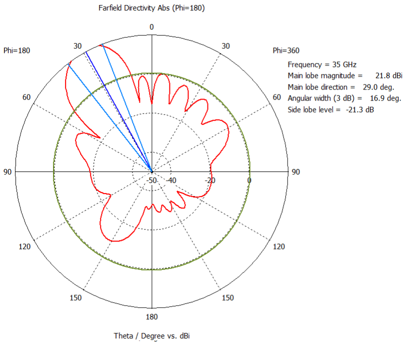

Figure A.20: Steered Radiation Pattern cut $\phi = 180°$

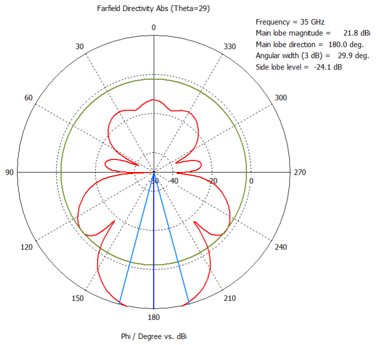

Figure A.21: Steered Radiation Pattern cut $\theta = 29°$

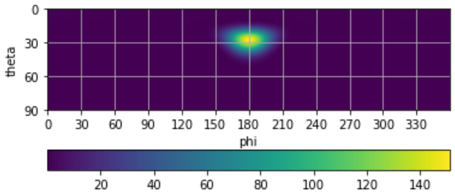

Figure A.22: Steered Radiation Pattern $(\theta, \phi) = (29°, 180°)$ equirectangular projection

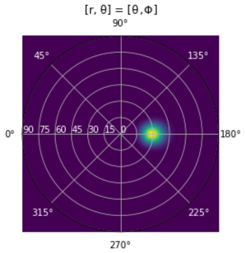

Figure A.23: Steered Radiation Pattern $(\theta, \phi) = (29°, 180°)$ fisheye equidistant projection

Steered radiation pattern with $\psi_{0y} = 0°$ and $\psi_{0x} = 127°$

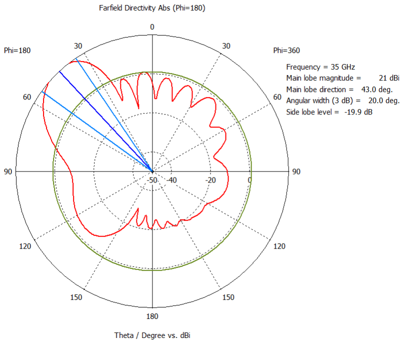

Figure A.24: Steered Radiation Pattern cut $\phi = 180°$

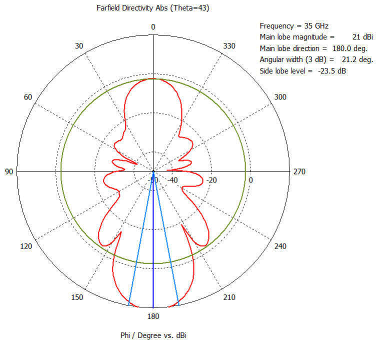

Figure A.25: Steered Radiation Pattern cut $\theta = 43°$

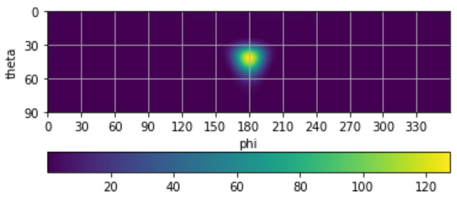

Figure A.26: Steered Radiation Pattern $(\theta, \phi) = (43^\circ, 180^\circ)$ equirectangular projection

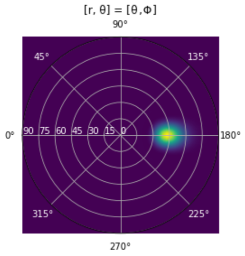

Figure A.27: Steered Radiation Pattern $(\theta, \phi) = (43^\circ, 180^\circ)$ fisheye equidistant projection

Steered radiation pattern with $\psi_{0y} = 46^\circ$ and $\psi_{0x} = 0^\circ$

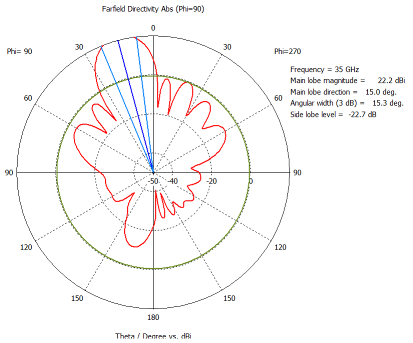

Figure A.28: Steered Radiation Pattern cut $\phi = 90^\circ$

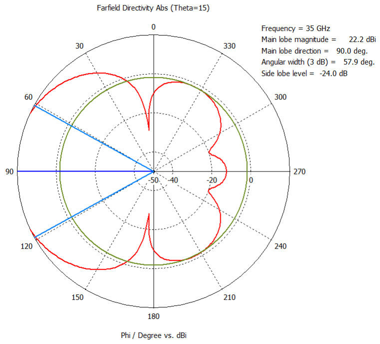

Figure A.29: Steered Radiation Pattern cut $\theta = 15^\circ$

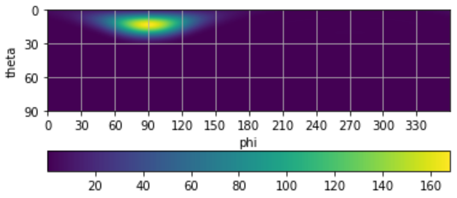

Figure A.30: Steered Radiation Pattern $(\theta, \phi) = (15^\circ, 90^\circ)$ equirectangular projection

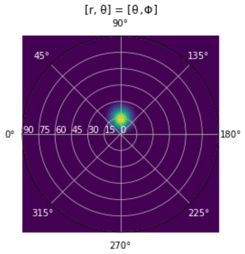

Figure A.31: Steered Radiation Pattern $(\theta, \phi) = (15^\circ, 90^\circ)$ fisheye equidistant projection

Steered radiation pattern with $\psi_{0y} = 46^\circ$ and $\psi_{0x} = 46^\circ$

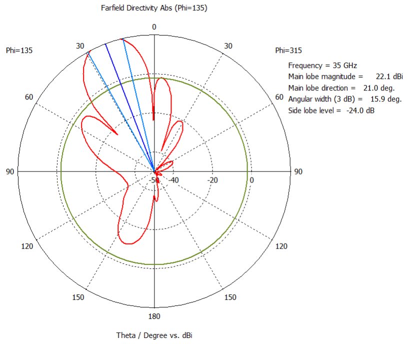

Figure A.32: Steered Radiation Pattern cut $\phi = 135^\circ$

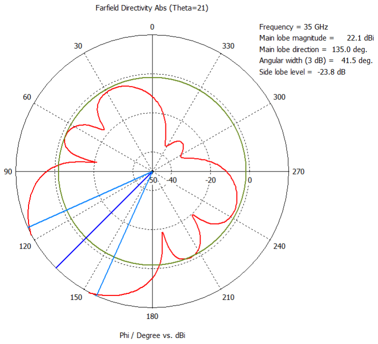

Figure A.33: Steered Radiation Pattern cut $\theta = 21^\circ$

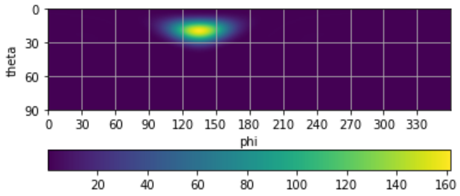

Figure A.34: Steered Radiation Pattern $(\theta, \phi) = (21°, 135°)$ equirectangular projection

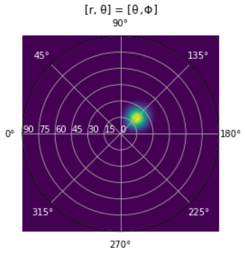

Figure A.35: Steered Radiation Pattern $(\theta, \phi) = (21°, 135°)$ fisheye equidistant projection

Steered radiation pattern with $\psi_{0y} = 46°$ and $\psi_{0x} = 90°$

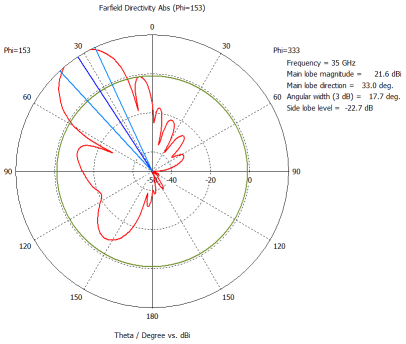

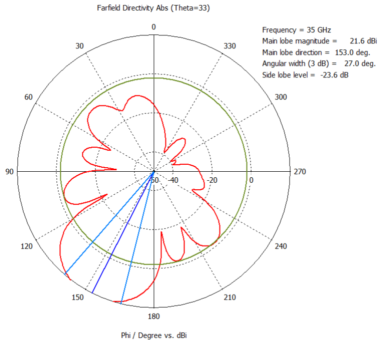

Figure A.36: Steered Radiation Pattern cut $\phi = 153°$ Figure A.37: Steered Radiation Pattern cut $\theta = 33°$

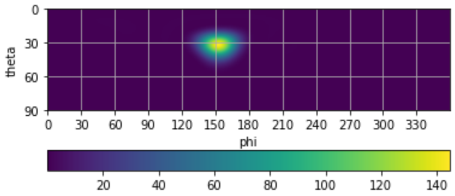

Figure A.38: Steered Radiation Pattern $(\theta, \phi) = (33°, 153°)$ equirectangular projection

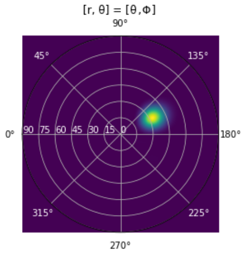

Figure A.39: Steered Radiation Pattern $(\theta, \phi) = (33°, 153°)$ fisheye equidistant projection

Steered radiation pattern with $\psi_{0y} = 46°$ and $\psi_{0x} = 127°$

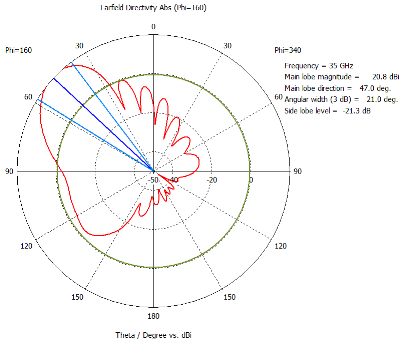

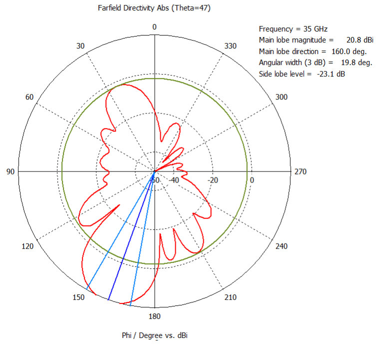

Figure A.40: Steered Radiation Pattern cut $\phi = 160°$ Figure A.41: Steered Radiation Pattern cut $\theta = 47°$

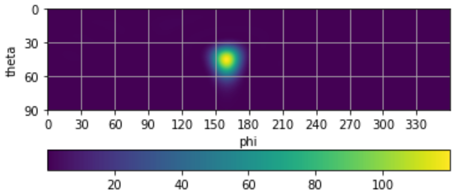

Figure A.42: Steered Radiation Pattern $(\theta, \phi) = (47^\circ, 160^\circ)$ equirectangular projection

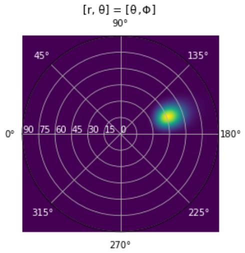

Figure A.43: Steered Radiation Pattern $(\theta, \phi) = (47^\circ, 160^\circ)$ fisheye equidistant projection

Steered radiation pattern with $\psi_{0y} = 90^\circ$ and $\psi_{0x} = 0^\circ$

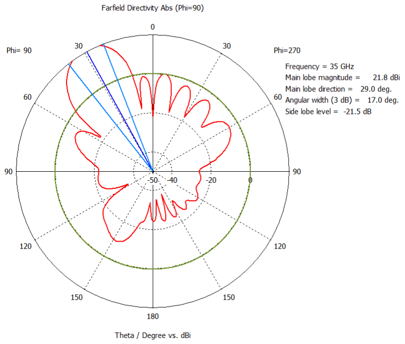

Figure A.44: Steered Radiation Pattern cut $\phi = 90^\circ$

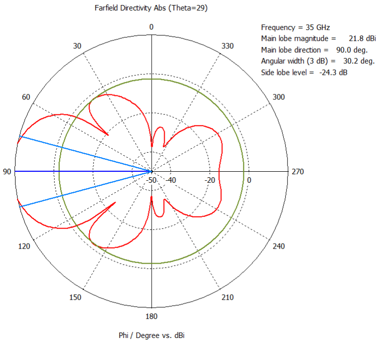

Figure A.45: Steered Radiation Pattern cut $\theta = 29^\circ$

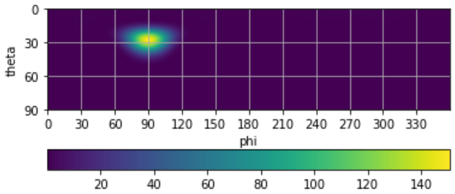

Figure A.46: Steered Radiation Pattern $(\theta, \phi) = (29^\circ, 90^\circ)$ equirectangular projection

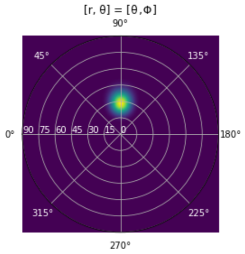

Figure A.47: Steered Radiation Pattern $(\theta, \phi) = (29^\circ, 90^\circ)$ fisheye equidistant projection

Steered radiation pattern with $\psi_{0y} = 90^\circ$ and $\psi_{0x} = 46^\circ$

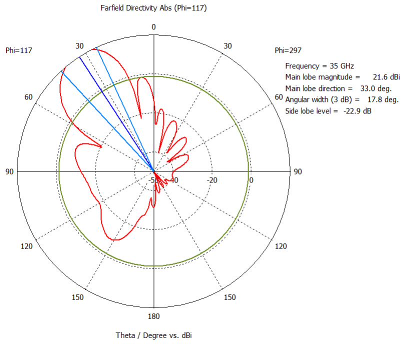

Figure A.48: Steered Radiation Pattern cut $\phi = 117^\circ$

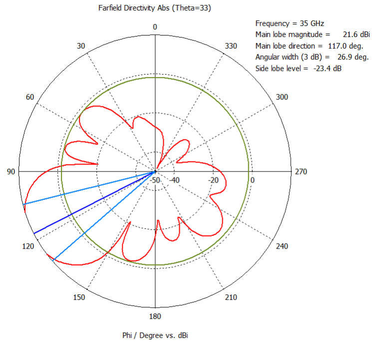

Figure A.49: Steered Radiation Pattern cut $\theta = 33^\circ$

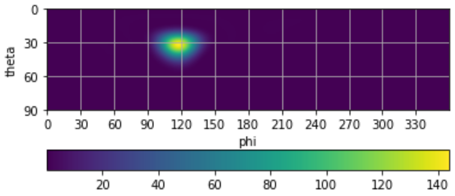

Figure A.50: Steered Radiation Pattern $(\theta, \phi) = (33^\circ, 117^\circ)$ equirectangular projection

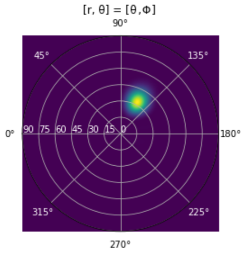

Figure A.51: Steered Radiation Pattern $(\theta, \phi) = (33^\circ, 117^\circ)$ fisheye equidistant projection

Steered radiation pattern with $\psi_{0y} = 90^\circ$ and $\psi_{0x} = 90^\circ$

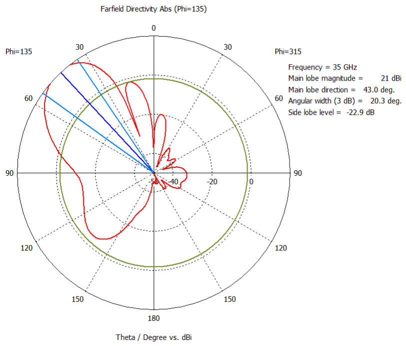

Figure A.52: Steered Radiation Pattern cut $\phi = 135^\circ$

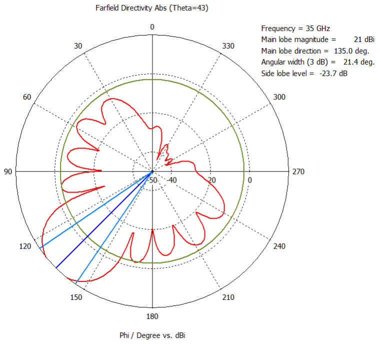

Figure A.53: Steered Radiation Pattern cut $\theta = 43^\circ$

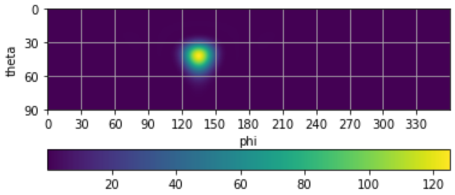

Figure A.54: Steered Radiation Pattern $(\theta, \phi) = (43^\circ, 135^\circ)$ equirectangular projection

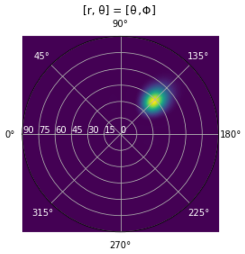

Figure A.55: Steered Radiation Pattern $(\theta, \phi) = (43^\circ, 135^\circ)$ fisheye equidistant projection

Steered radiation pattern with $\psi_{0y} = 90^\circ$ and $\psi_{0x} = 127^\circ$

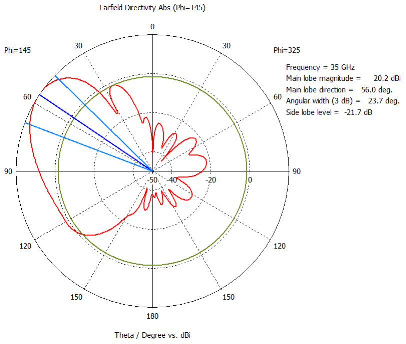

Figure A.56: Steered Radiation Pattern cut $\phi = 145^\circ$

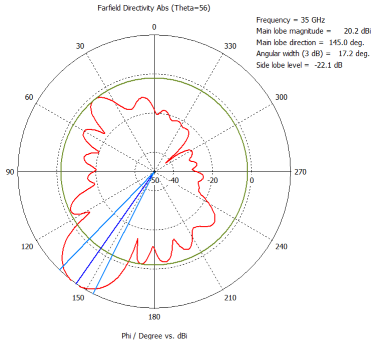

Figure A.57: Steered Radiation Pattern cut $\theta = 56^\circ$

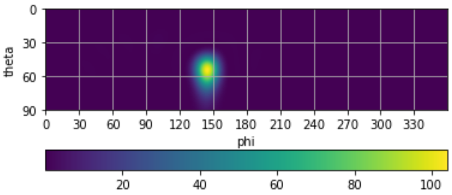

Figure A.58: Steered Radiation Pattern $(\theta, \phi) = (56°, 145°)$ equirectangular projection

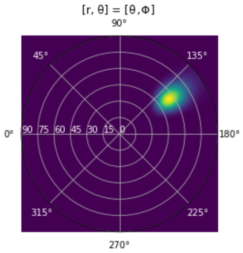

Figure A.59: Steered Radiation Pattern $(\theta, \phi) = (56°, 145°)$ fisheye equidistant projection

Steered radiation pattern with $\psi_{0y} = 127°$ and $\psi_{0x} = 0°$

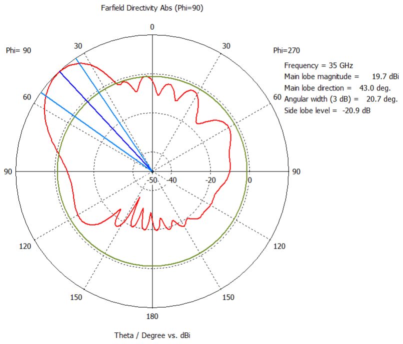

Figure A.60: Steered Radiation Pattern cut $\phi = 90°$

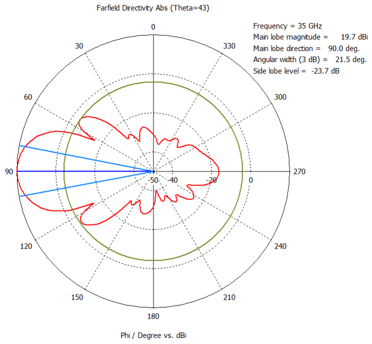

Figure A.61: Steered Radiation Pattern cut $\theta = 43°$

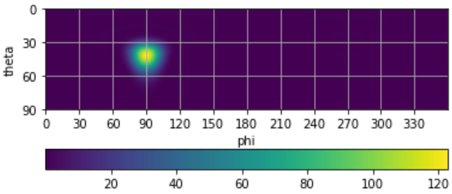

Figure A.62: Steered Radiation Pattern $(\theta, \phi) = (43°, 90°)$ equirectangular projection

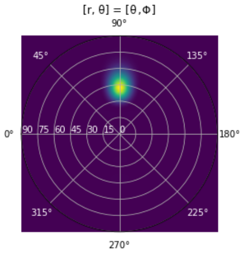

Figure A.63: Steered Radiation Pattern $(\theta, \phi) = (43°, 90°)$ fisheye equidistant projection

Steered radiation pattern with $\psi_{0y} = 127°$ and $\psi_{0x} = 46°$

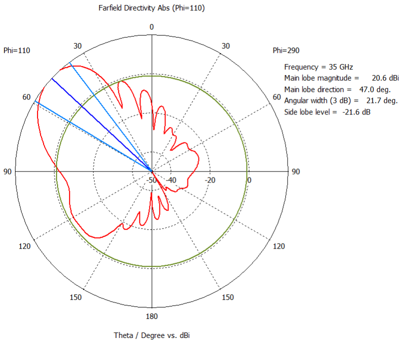

Figure A.64: Steered Radiation Pattern cut $\phi = 110°$

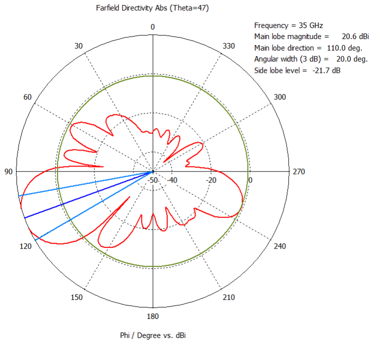

Figure A.65: Steered Radiation Pattern cut $\theta = 47°$

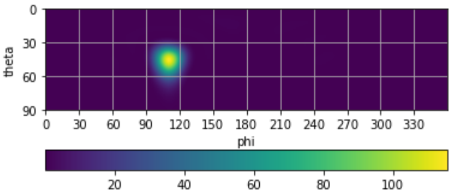

Figure A.66: Steered Radiation Pattern $(\theta, \phi) = (47^\circ, 110^\circ)$ equirectangular projection

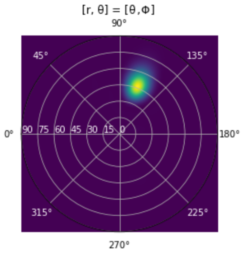

Figure A.67: Steered Radiation Pattern $(\theta, \phi) = (47^\circ, 110^\circ)$ fisheye equidistant projection

Steered radiation pattern with $\psi_{0y} = 127^\circ$ and $\psi_{0x} = 90^\circ$

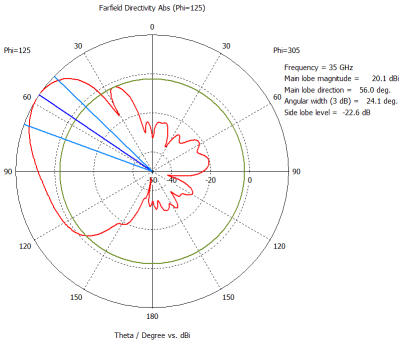

Frequency = 35 GHz
Main lobe magnitude = 20.1 dBi
Main lobe direction = 56.0 deg.
Angular width (3 dB) = 24.1 deg.
Side lobe level = -22.6 dB

Figure A.68: Steered Radiation Pattern cut $\phi = 125^\circ$

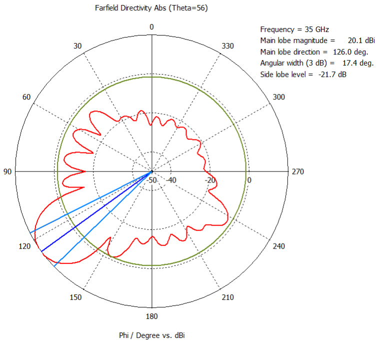

Frequency = 35 GHz
Main lobe magnitude = 20.1 dBi
Main lobe direction = 126.0 deg.
Angular width (3 dB) = 17.4 deg.
Side lobe level = -21.7 dB

Figure A.69: Steered Radiation Pattern cut $\theta = 56^\circ$

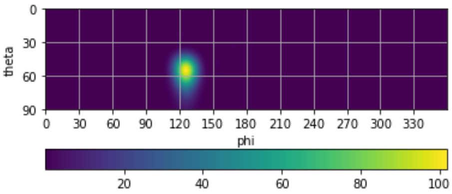

Figure A.70: Steered Radiation Pattern $(\theta, \phi) = (56^\circ, 125^\circ)$ equirectangular projection

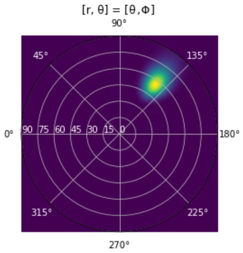

Figure A.71: Steered Radiation Pattern $(\theta, \phi) = (56^\circ, 125^\circ)$ fisheye equidistant projection

Steered radiation pattern with $\psi_{0y} = 127^\circ$ and $\psi_{0x} = 127^\circ$

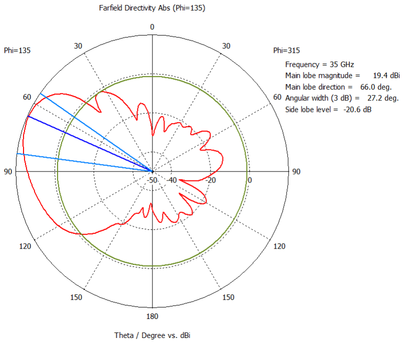

Frequency = 35 GHz
Main lobe magnitude = 19.4 dBi
Main lobe direction = 66.0 deg.
Angular width (3 dB) = 27.2 deg.
Side lobe level = -20.6 dB

Figure A.72: Steered Radiation Pattern cut $\phi = 135^\circ$

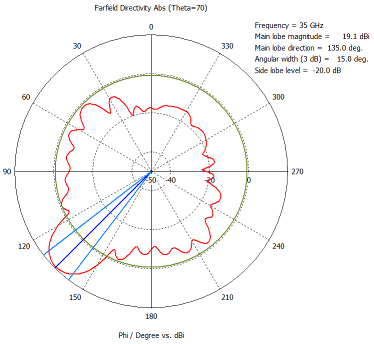

Frequency = 35 GHz
Main lobe magnitude = 19.1 dBi
Main lobe direction = 135.0 deg.
Angular width (3 dB) = 15.0 deg.
Side lobe level = -20.0 dB

Figure A.73: Steered Radiation Pattern cut $\theta = 66^\circ$

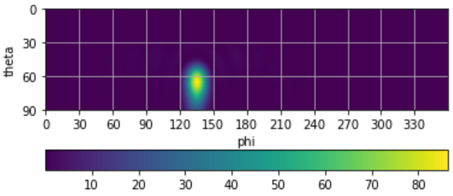

Figure A.74: Steered Radiation Pattern $(\theta, \phi) = (66°, 135°)$ equirectangular projection

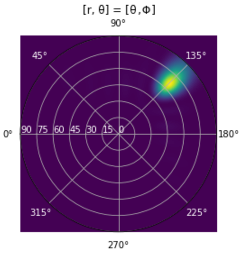

Figure A.75: Steered Radiation Pattern $(\theta, \phi) = (66°, 135°)$ fisheye equidistant projection

Appendix B

Simulation results according to the ELOS for see and avoid requirements

The radar simulation was done to verify the ELOS for see and avoid minimum requirements specified in section 5.5. An environment was set in $Blender$, with a single cube 583 m away from the camera, similar to environment A. Due to the larger distance, an image with more pixel resolution was necessary to identify the cube in the image. The rendered image was output with 1550×1500 pixels, and the maximum distance to detect, R_{max}, was set to 583 m, along with a false alarm probability of $P_{fa} = 10^{-2}$ and a noise temperature of $T_{noise} = 290$ K. According to the reasoning of section 5.3, the results represented in table B.1 were obtained.

N_0 [W]	4.002$\times 10^{-12}$
T_{ch} [s]	3.887$\times 10^{-6}$
f_s [Hz]	2$\times 10^{9}$
T_s [s]	5$\times 10^{-10}$
N	7774
λ [m]	8.696 $\times 10^{-3}$
k_0 [rad/m]	722.566
V_{th} [V]	3.079 $\times 10^{-3}$
$P_{r,min}$ [W]	4.742 $\times 10^{-6}$
P_t [W]	179.854

Table B.1: Radar simulation specifications

The image corresponding to the simulation result is depicted in figure B.1. The target was correctly identified. The frequency spectrum of the sampled signal is depicted in figure B.2, being $A_{fft} = 4.03 \times 10^{-3}$ V, with a maximum at a frequency corresponding to $R_{sim} = 582.05$ m. Note that the 1 m difference is due to the surface of the cube being 1 m closer than the center, since the cube as a side length of 2 m. In figure B.3, the frequency spectrum corresponding to one of the directions without detection is shown. It is clear, that the threshold level is correctly set.

Note that, to detect targets at a larger distance, it is possible to conclude, by comparing tables B.1 and 5.1, that besides an increase of the transmitted power, there is also an increase of the necessary number of samples. The detection of targets at larger distances, besides requiring an array with a larger number of

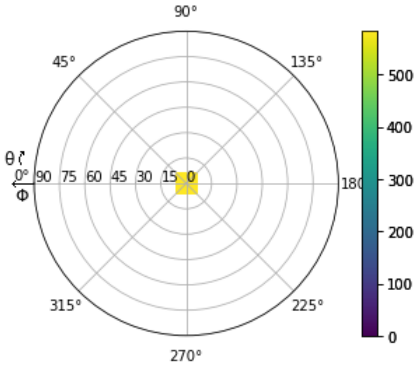

Figure B.1: Simulation result image for environment according to ELOS for see and avoid

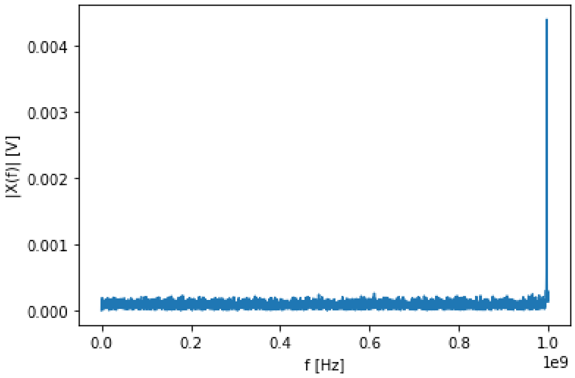

Figure B.2: Frequency spectrum of the scan with radiation pattern pointing to the cube

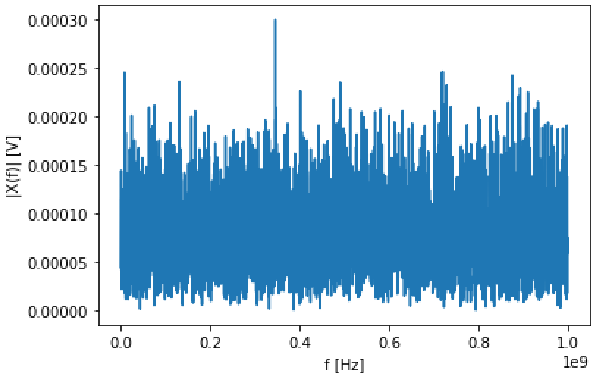

Figure B.3: Frequency spectrum of the scan with radiation pattern pointing to another direction

elements, to obtain higher gains, would also require a higher processing power of the system.